AD_____

GRANT NUMBER DAMD17-98-1-8141

TITLE: Quantitative Three-dimensional Ultrasonic Mammography

PRINCIPAL INVESTIGATOR: T. Douglas Mast, Ph.D.

CONTRACTING ORGANIZATION: The Pennsylvania State University
State College, Pennsylvania 16804-0030

REPORT DATE: July 1999

TYPE OF REPORT: Annual

PREPARED FOR: Commanding General
U.S. Army Medical Research and Materiel Command
Fort Detrick, Maryland 21702-5012

DISTRIBUTION STATEMENT: Approved for Public Release;
Distribution Unlimited

The views, opinions and/or findings contained in this report are
those of the author(s) and should not be construed as an official
Department of the Army position, policy or decision unless so
designated by other documentation.

20001121 068

REPORT DOCUMENTATION PAGE

Form Approved
OMB No. 0704-0188

1. AGENCY USE ONLY *(Leave blank)*	2. REPORT DATE July 1999	3. REPORT TYPE AND DATES COVERED Annual (1 Jul 98 - 30 Jun 99)

4. TITLE AND SUBTITLE
Quantitative Three-dimensional Ultrasonic Mammography

5. FUNDING NUMBERS
DAMD17-98-1-8141

6. AUTHOR(S)
T. Douglas Mast, Ph.D.

7. PERFORMING ORGANIZATION NAME(S) AND ADDRESS(ES)
The Pennsylvania State University
State College, Pennsylvania 16804-0030

8. PERFORMING ORGANIZATION REPORT NUMBER

9. SPONSORING / MONITORING AGENCY NAME(S) AND ADDRESS(ES)
U.S. Army Medical Research and Materiel Command
Fort Detrick, Maryland 21702-5012

10. SPONSORING / MONITORING AGENCY REPORT NUMBER

11. SUPPLEMENTARY NOTES

12a. DISTRIBUTION / AVAILABILITY STATEMENT
Approved for Public Release; Distribution Unlimited

12b. DISTRIBUTION CODE

13. ABSTRACT *(Maximum 200 words)*

The goal of this research, improved diagnosis of breast cancer by quantitative, high-resolution three-dimensional ultrasonic imaging, is being reached by a thorough program that synthesizes recent advances in tissue modeling, adaptive imaging, instrumentation, and signal processing. The goal of three-dimensional quantitative imaging is currently being achieved using novel time-domain inverse scattering methods invented by the Principal Investigator and coworkers. Nonlinear forms of these methods provide a robust approach to adaptive imaging that is based on compensation for three-dimensional scattering from actual breast tissue structure. A crucial aspect of the research is the use of realistic tissue models for ultrasonic propagation through breast tissue. Tissue modeling techniques employ tissue maps obtained from specimen cross sections as well as from newly available high-resolution volume photographic data. Calculated scattering from these tissue models will provide accurate characterization of ultrasonic propagation within breast tissue and will also provide realistic data for quantitative imaging algorithms. Synthesis of these breakthroughs will make possible new mammographic applications of ultrasound that will provide clinicians with previously unavailable quantitative information and image detail. The end result will be a lower-cost, more effective, and safer modality for diagnosis, detection, and monitoring of breast cancer.

14. SUBJECT TERMS
Breast Cancer

Ultrasound, Three-Dimensional, Imaging, Scattering, Diagnosis

15. NUMBER OF PAGES
117

16. PRICE CODE

17. SECURITY CLASSIFICATION OF REPORT Unclassified	18. SECURITY CLASSIFICATION OF THIS PAGE Unclassified	19. SECURITY CLASSIFICATION OF ABSTRACT Unclassified	20. LIMITATION OF ABSTRACT Unlimited

FOREWORD

Opinions, interpretations, conclusions and recommendations are those of the author and are not necessarily endorsed by the U.S. Army.

_____ Where copyrighted material is quoted, permission has been obtained to use such material.

_____ Where material from documents designated for limited distribution is quoted, permission has been obtained to use the material.

_____ Citations of commercial organizations and trade names in this report do not constitute an official Department of Army endorsement or approval of the products or services of these organizations.

_____ In conducting research using animals, the investigator(s) adhered to the "Guide for the Care and Use of Laboratory Animals," prepared by the Committee on Care and use of Laboratory Animals of the Institute of Laboratory Resources, national Research Council (NIH Publication No. 86-23, Revised 1985).

TDM ✓ For the protection of human subjects, the investigator(s) adhered to policies of applicable Federal Law 45 CFR 46.

_____ In conducting research utilizing recombinant DNA technology, the investigator(s) adhered to current guidelines promulgated by the National Institutes of Health.

_____ In the conduct of research utilizing recombinant DNA, the investigator(s) adhered to the NIH Guidelines for Research Involving Recombinant DNA Molecules.

_____ In the conduct of research involving hazardous organisms, the investigator(s) adhered to the CDC-NIH Guide for Biosafety in Microbiological and Biomedical Laboratories.

27 July 1999

_____   _____
PI - Signature   Date

IV. Table of Contents

V. Introduction

An investigation of three-dimensional ultrasonic mammography is underway. The goal of the research is improved diagnosis of breast cancer by quantitative, high-resolution three-dimensional ultrasonic imaging. This goal is being reached by a thorough program that synthesizes recent advances in tissue modeling, adaptive imaging, instrumentation, and signal processing. The final result of the research will be a major advance in quantitative three-dimensional ultrasonic mammography. Improved resolution, accurate quantitative information on tissue properties, and precise determination of three-dimensional breast structure will provide crucial new information for detection, diagnosis, and monitoring of breast cancer. The goal of three-dimensional quantitative imaging is currently being achieved using novel inverse scattering methods invented by the Principal Investigator and coworkers. Use of full time-domain scattering information provides images with high point resolution, contrast resolution, and quantitative accuracy without significant artifacts. Nonlinear forms of these methods provide a robust approach to adaptive imaging that is based on compensation for three-dimensional scattering from actual tissue structure. Unlike previous adaptive imaging methods based on assumptions of phase-screen aberrators and point scatterers, these methods provide aberration correction ideally suited to distributed inhomogeneous tissue like the breast. A unique and innovative aspect of the research is the use of realistic tissue models for ultrasonic propagation through breast tissue. Such models have been shown to realistically model wavefront distortion in the human abdominal wall, but have not to date been applied to the human breast. Tissue modeling techniques employ tissue maps obtained from specimen cross sections as well as from newly available high-resolution volume photographic data. Calculated scattering from these tissue models will provide accurate characterization of ultrasonic propagation within breast tissue and will also provide realistic data for quantitative imaging algorithms. The above studies will facilitate the application of breakthroughs from tissue modeling, inverse scattering, and signal processing to the critical application of ultrasonic mammography. Completion of the proposed research will make possible new mammographic applications of ultrasound that will provide clinicians with previously unavailable information and detail. The end result will be a lower-cost, more effective, and safer modality for diagnosis, detection, and monitoring of breast cancer.

VI. Body of Report

Below, the accomplishments of the first year for this project are summarized under the four categories of the approved Statement of Work. Details are given for how accomplishments to date fit into the overall research plan. Where applicable, brief descriptions of planned research indicate how the remainder of the Statement of Work will be fulfilled.

A. Quantitative Imaging Algorithm Development

In the first year of this USAMRMC-funded Breast Cancer Research Program project, great progress has been made on development of new quantitative imaging algorithms for three-dimensional ultrasonic mammography. Research on algorithm development has occurred in two areas: (1) a new time-domain diffraction tomography method for wideband quantitative imaging and (2) nonlinear extensions to a novel eigenfunction-based inverse scattering method.

The new time-domain diffraction tomography method [1, 2], which is specifically designed for ultrasonic mammography, allows quantitative, high-resolution images to be obtained using direct synthetic-aperture processing of time-domain scattered fields. This method provides tomographic images of inhomogeneous media using scattering measurements made on a surface surrounding the medium of interest, *e.g.*, on a circle for two-dimensional problems or on a sphere for three-dimensional problems. Images of compressibility variations are then reconstructed using coherent combination of the far-field scattered waveforms, delayed and summed in a manner that numerically focuses on the unknown medium. This approach is closely related to synthetic aperture imaging; however, unlike conventional synthetic-aperture methods, the present method provides quantitative reconstructions of compressibility variations, analogous to frequency-compounded filtered backpropagation images weighted by the spectrum of the incident wave. A complete description of the method, with example two-dimensional and three-dimensional reconstruction results, is given in Ref. [2], included as Appendix A of this report. A brief abstract describing the work, presented at Forum Acusticum 99, is included in Appendix D.

The results of the new time-domain imaging method are exciting for several reasons. First, the images are both higher in quality and more efficiently computed than conventional single-frequency quantitative images. The high point and contrast resolution, as well as absence of artifacts usually associated with diffraction tomography, suggests that this method will be very useful for detection and characterization of breast lesions. Second, because of the close analogy between the new method and delay-and-sum imaging, the new method could be implemented in hardware using beamforming technology already present on digital ultrasound scanners. Furthermore, the new time-domain method can easily incorporate other imaging techniques (*e.g.*, time-gain compensation, harmonic imaging, and aberration correction) currently used in clinical and experimental B-scan systems.

Work was also performed on nonlinear (aberration-corrected) implementation of a method for quantitative imaging using eigenfunctions of the scattering operator [3]–[4]. A 1998 presentation of this method at a meeting of the American Institute of Ultrasound in Medicine [5] was received with interest. Preliminary work on iterative nonlinear inverse

6

scattering, with application to quantitative imaging of strongly scattering media such as the human breast, shows promise for the potential of aberration correction to improve quantitative ultrasonic mammography.

Work on algorithm development will continue with synthesis of wideband time-domain inverse scattering together with aberration correction based on quantitative estimates of the unknown medium. Since these estimates are obtained directly from inverse scattering reconstructions, iterative reconstruction procedures will provide the highest quantitative accuracy available for the data. Since the nonlinear eigenfunction method provides a simple approach to aberration correction (improved reconstructions are obtained using numerical retransmission of eigenfunctions into the estimated medium), this procedure is much more efficient than other available nonlinear inverse scattering methods. This form of nonlinear aberration correction, in conjunction with the new time-domain imaging method described above, provide all the capabilities required for the proposed method of three-dimensional quantitative ultrasonic mammography.

B. Tissue Modeling

Progress toward improved scattering models for ultrasound-breast tissue interaction has been made in several related studies.

A finite-difference time-domain simulation of ultrasonic propagation through cross-sectional models of chest wall tissue [6, 7] has generated several important results that are directly relevant to the planned simulation of propagation through breast tissue. First, this work expands upon previous models [8, 9] by including tissue-dependent absorption effects. The absorption model developed will be an important part of the planned two-dimensional and three-dimensional simulations of ultrasonic scattering from breast tissue. Second, the chest study contained an analysis of the frequency dependence of ultrasonic wavefront distortion. A comparison of distortion effects for varying pulse center frequencies showed that, for soft tissue paths through the chest wall, energy level and waveform distortion increase markedly with rising ultrasonic frequency and that arrival-time fluctuations increase to a lesser degree. Since breast tissue has been observed to be more strongly scattering than other soft tissues [10], these results are of particular importance for ultrasonic mammography. A full description of this study, with numerical results including statistical summaries, is given in Ref. [7], included here as Appendix B. An abstract describing the work, presented at the 136th Meeting of the Acoustical Society of America, is included in Appendix D.

In accordance with the Statement of Work, scattering has been computed for canonically-shaped inhomogeneities including spheres, cylinders, and rectangular slabs. Time-domain scattered fields were computed using exact solutions [12] for spheres and cylinders with sound speed and density different from the surrounding medium. Time-domain scattered fields were also computed, using a weak scattering approximation, for rectangular slabs with a sound speed different from the surrounding medium. The purpose of these computations was to provide definitive test data for quantitative imaging algorithms. Example reconstructions based on these computations are provided in Ref. [2], provided as Appendix A.

A new k-space method was implemented for simulating wave propagation in soft tissue [11]. Numerical results, including quantitative comparisons of accuracy, showed that the k-

space method can achieve very accurate results for large-scale ultrasonic propagation through soft tissue. The computational efficiency obtained with the new k-space method is much greater than that of existing finite difference or pseudospectral methods. The method is described and quantitatively analyzed in Ref. [11], included here as Appendix C. Because of the remarkable accuracy and efficiency of the new k-space method, a three-dimensional version of this method will be employed for three-dimensional scattering computations in the remainder of this project. A three-dimensional version of the k-space code, incorporating the absorption model of Ref. [7] (Appendix B) as well as absorbing boundary conditions, has been implemented and is ready for use with breast tissue models. The existing code is also fully parallelizable, since most of the computational load is associated with execution of multithreaded fast Fourier transform computations.

Work is currently ongoing for optimization of speed and accuracy of the k-space method for scattering computations. Preliminary comparisons between the k-space code and a commercial pseudospectral code have shown that the k-space code allows accurate results to be obtained with much larger time steps and fewer independent variables, so that the k-space code is superior both in computational speed and in storage requirements. Both of these considerations are critical for the planned three-dimensional computations of scattering from breast tissue.

Now that a robust, efficient three-dimensional method for computation of ultrasonic propagation is available, work on mapping of breast tissue has begun in earnest. In collaboration with colleagues at the University of Rochester, cross-sectional breast tissue specimens have been sectioned and stained for high-resolution segmentation by tissue type. A license for use of the Visible Woman data set has been obtained; the second year of the project will include a substantial effort to construct three-dimensional tissue maps from the provided photographic, x-ray, and MRI data.

C. Quantitative Imaging Algorithm Implementation

Implementation of quantitative imaging algorithms, including the time-domain diffraction tomography method and the nonlinear eigenfunction method described above, has to date been primarily performed using simulated data. Quantitative reconstructions performed using the time-domain diffraction tomography method are shown in Ref. [2] (Appendix A) for simulated two-dimensional and three-dimensional scattering data. These results are promising for ultrasonic mammography. As discussed below in section D (Evaluation and Comparison of Results), time-domain quantitative images show parametric accuracy, high resolution, and few artifacts. Effects of limited scattering data, shown in Fig. 3 of Appendix A for the 2D case, indicate that accurate images can be obtained without the necessity of apertures that entirely enclose the breast.

Experimental testing of the new time-domain quantitative imaging method, in collaboration with colleagues at the University of Rochester, is now beginning. Tissue-mimicking phantoms composed of agar gel with glass spheres have been constructed. An anthropomorphic breast-mimicking phantom, developed in collaboration between General Electric, University of Wisconsin, and University of Rochester, is also available for testing. Time-domain scattering data, to be taken with the 2048-element University of Rochester ring transducer

[13] will be used as input for testing of the new time-domain quantitative imaging method. Both 2D and 3D reconstructions will be performed.

As proposed in the original Statement of Work, a nonlinear, aberration-corrected version of the new time-domain inverse scattering method will also be implemented and tested with simulated data (from the breast tissue models described above in section B, Tissue Modeling) as well as experimental data. The same data will be used as input for standard synthetic-aperture imaging, so that image quality and accuracy can be directly compared.

D. Evaluation and Comparison of Results

Analysis of the time-domain imaging results for simulated data is given in Ref. [2] (Appendix A). These results indicate that high quantitative accuracy can be achieved. Computations of point-spread functions (Fig. 2 in Appendix A) show that the time-domain method yields higher point and contrast resolution than single-frequency diffraction tomography. For the 3D case, the level of the first sidelobe is reduced by 13 dB, while the second sidelobe is reduced by 18 dB. Because of the broadband scattering information employed, the width of the main lobe indicates point resolution of features smaller than one-half wavelength at the center frequency. Evaluation of quantitative accuracy (Fig. 4) shows that the time-domain diffraction tomography method provides parametric accuracy similar to established single-frequency methods while showing much more immunity from artifacts. Similar quantitative analysis will be performed for images obtained using the nonlinear aberration-corrected inverse scattering method mentioned above.

Two-dimensional and three-dimensional reconstructions performed using the new time-domain quantitative imaging method will be directly compared to analogous images from other modalities such as x-ray computed tomography and conventional B-scan ultrasound. Consultants Dr. Jon Meilstrup, Dr. Claudia Kasales, and Dr. Carroll Osgood will help with this portion of evaluation and comparison of results. Although the original statement of work defers this image evaluation task until the third year of the project, this work may begin during the second year if no unanticipated experimental difficulties are encountered.

Regarding the task of publishing results in archival journals, the first year of the project has already resulted in three submitted manuscripts. Further publications planned to be prepared during the next year will be based on experimental testing of the new time-domain quantitative imaging method, optimization and benchmarking of the k-space algorithm, and scattering computations employing realistic breast tissue models.

VII. Key Research Accomplishments

The key research accomplishments to date in this project can be summarized as follows:

- Development of a new time-domain quantitative imaging method designed specifically for ultrasonic mammography.

- Numerical implementation and testing of the new time-domain imaging method, showing that this method provides high accuracy with greater efficiency than previous inverse scattering methods.

- Implementation of a nonlinear aberration-corrected eigenfunction inverse scattering method.

- Implementation of a tissue-dependent absorption model for simulations of scattering and propagation.

- Characterization of the frequency dependence of ultrasonic scattering from human soft tissues.

- Exact computation of time-domain scattering from simple objects for testing of quantitative imaging methods.

- Implementation and testing of a new k-space method for computation of scattering, indicating that the method is accurate and extremely efficient, and therefore ideal for the proposed 3D computations of scattering from breast tissue.

- Extension of the new k-space method to include tissue-dependent absorption, absorbing boundary layers, and three-dimensional scattering.

- Use of the k-space method to compute time-domain scattering data for testing of quantitative imaging algorithms.

- Quantitative analysis of inverse scattering results, indicating that time-domain reconstructions provide much higher point resolution, contrast resolution, and freedom from artifacts than single-frequency reconstructions.

VIII. Reportable Outcomes

Reportable outcomes for the research have, to date, included three papers submitted to archival journals (Refs. [2], [7], and [11]), as well as two published abstracts presented at scientific meetings (Refs. [1] and [6]). All of these publications, as well as a current Curriculum Vitae for the Principal Investigator, are included below in the Appendices.

IX. Conclusions

The first year of this USAMRMC-funded project has yielded considerable progress toward the goal of improved diagnosis of breast cancer by three-dimensional ultrasonic imaging. Several breakthroughs have been made which will provide a solid foundation for the continued tissue modeling and quantitative imaging research planned for the last two years of the project.

A major breakthrough has been the invention and implementation of a new time-domain diffraction tomography method designed for ultrasonic mammography. This method is potentially of very great importance for breast cancer diagnosis for several reasons: (1) images have higher quality than that achievable by conventional inverse scattering methods or by current ultrasound scanners, (2) tissue parameters are computed and quantitatively imaged with high accuracy, and (3) the close analogy between the new method and conventional synthetic-aperture imaging will allow rapid implementation of the new method on hardware similar to currently used beamformers. The additional improvement of aberration correction should increase the value of this method even more, because the strong scattering inherent to breast tissue is an important limiting factor to existing ultrasonic imaging methods.

In the area of breast tissue modeling, simulation methods have been developed that will allow efficient computation of scattering from fully three-dimensional models of breast tissue. A model for tissue absorption, important for realistic simulation of scattering in breast tissue, has been implemented. The frequency dependence of ultrasonic scattering from soft tissue has been shown to be a critical consideration for aberrating media such as the breast. A new k-space method has been implemented, shown to provide remarkable accuracy and efficiency, and extended to include absorbing boundary conditions as well as tissue-dependent ultrasonic absorption. A three-dimensional implementation of this method is already in place and is ready for computations based on realistic breast tissue models.

Future work based on these breakthroughs will follow the approved Statement of Work. Plans for the next year of research include extension of time-domain inverse scattering to include aberration correction, testing of the new quantitative imaging algorithm using measured scattering data, construction of realistic breast tissue models from cross-sectional and volume data, and computation of ultrasonic propagation through these tissue models. In the third year of the project, definitive aberration-corrected reconstructions will be computed both for measured scattering data from breast-mimicking phantoms and for simulated scattering data using detailed breast models. These results will be carefully evaluated for accuracy and clinical utility, in collaboration with the named clinical consultants.

The final outcome of the successfully completed project will be a novel method for early detection, characterization, and treatment monitoring of breast cancer lesions. Results to date indicate that the final method will provide image quality and diagnostic information greatly superior to current 2D and 3D ultrasonic mammography methods The finally resulting method is expected to be competitive with magnetic resonance imaging and x-ray computed tomography as a tool for breast cancer diagnosis, while maintaining inherent advantages of ultrasound such as lower cost, ability to characterize cystic and solid lesions, and safe nonionizing radiation.

X. References

[1] Mast, T. D., "Time-domain ultrasound diffraction tomography," J. Acoust. Soc. Am. **105**, 1014 (1999).

[2] Mast, T. D., "Wideband quantitative ultrasonic imaging by time-domain diffraction tomography," submitted to *J. Acoust. Soc. Am.* (1999).

[3] Mast, T. D., Nachman, A. I., and Waag, R. C., "Focusing and imaging using eigenfunctions of the scattering operator," *J. Acoust. Soc. Am.* **102**, 715–725 (1997).

[4] Mast, T. D., Nachman, A. I., Liu, D.-L., and Waag, R. C., "Quantitative imaging with eigenfunctions of the scattering operator," *1997 IEEE Ultrasonics Symposium Proceedings*, Vol. 2, pp. 1507–1510.

[5] Waag, R. C., Mast, T. D., Nachman, A. I., and Liu, D.-L., "Quantitative imaging with eigenfunctions of the scattering operator," J. Ultrasound Med. **17**, S104 (1998).

[6] Mast, T. D., Hinkelman, L. M., and Waag, R. C., "Simulation of ultrasonic propagation, scattering, and attenuation in the human chest wall," J. Acoust. Soc. Am. **104**, 1844 (1998).

[7] Mast, T. D., Hinkelman, L. M., Metlay, L. A., Orr, M. J., and Waag, R. C., "Simulation of ultrasonic pulse propagation, distortion, and attenuation in the human chest wall," submitted to *J. Acoust. Soc. Am.* (1999).

[8] Mast, T. D., Hinkelman, L. M., Orr, M. J., Sparrow, V. W., and Waag, R. C., "Simulation of ultrasonic pulse propagation through abdominal wall," *J. Acoust. Soc. Am.* **102**, 1177–1190 (1997).

[9] Mast, T. D., Hinkelman, L. M., Orr, M. J., and Waag, R. C., "The effect of abdominal wall morphology on ultrasonic pulse distortion. Part II: Simulations," *J. Acoust. Soc. Am.* **104**, 3650–3664 (1998).

[10] Hinkelman, L. M., Liu, D.-L., Waag, R. C., Zhu, Q., and Steinberg, B. D., "Measurement and correction of ultrasonic pulse distortion produced by the human breast," J. Acoust. Soc. Am. **97**, 1958–1969 (1995).

[11] Souriau, L. P., Mast, T. D., Liu, D.-L. D., Nachman, A. I., and Waag, R. C., "A new k-space method for large-scale models of wave propagation in tissue," submitted to *IEEE Trans. Ultrason. Ferroelect. Freq. Control* (1999).

[12] Morse, P. M. and Ingard, K. U., *Theoretical Acoustics* (McGraw-Hill, New York, 1968), ch. 8.

[13] Jansson, T. T., Mast T. D., and Waag, R. C., "Measurements of differential scattering cross-section using a ring transducer," *J. Acoust. Soc. Am.* **103**, 3169–3179 (1998).

XI. Appendices

Appendix A

Wideband Quantitative Ultrasonic Imaging by Time-Domain Diffraction Tomography

Submitted to *Journal of the Acoustical Society of America*

Wideband quantitative ultrasonic imaging

by time-domain diffraction tomography

T. Douglas Mast

Applied Research Laboratory

The Pennsylvania State University

University Park, Pennsylvania 16802

March 26, 1999

Abstract

A quantitative ultrasonic imaging method employing time-domain scattering data is presented. This method provides tomographic images of medium properties such as the sound speed contrast; these images are equivalent to multiple-frequency filtered-backpropagation reconstructions using all frequencies within the bandwidth of the incident pulse employed. However, image synthesis is performed directly in the time domain using coherent combination of farfield scattered pressure waveforms, delayed and summed to numerically focus on the unknown medium. The time-domain method is more efficient than multiple-frequency diffraction tomography methods, and can, in some cases, be more efficient than single-frequency diffraction tomography. Example reconstructions, obtained using synthetic data for two-dimensional and three-dimensional scattering of wideband pulses, show that the time-domain reconstruction method provides image quality superior to single-frequency reconstructions for objects of size and contrast relevant to medical imaging problems such as ultrasonic mammography. The present method is closely related to existing synthetic-aperture imaging methods such as those employed in clinical ultrasound scanners. Thus, the new method can be extended to incorporate available image-enhancement techniques such as time-gain compensation to correct for medium absorption and aberration correction methods to reduce error associated with weak scattering approximations.

43.20.Fn, 43.60.Rw, 43.80.Vj, 43.20.Px

INTRODUCTION

Quantitative imaging of tissue properties is a potentially useful technique for diagnosis of cancer and other pathological conditions. Inverse scattering methods such as diffraction tomography can provide quantitative reconstruction of tissue properties including sound speed, density, and absorption. However, although previous inverse scattering methods have achieved high resolution and quantitative accuracy, such methods have not yet been incorporated into commercially successful medical ultrasound imaging systems.

Current inverse scattering methods are lacking in several respects with respect to conventional B-scan and synthetic aperture imaging techniques. Previous methods of diffraction tomography, including methods based on the Born approximation, the Rytov approximation, and higher-order nonlinear approaches, have usually been based on single-frequency scattering (*e.g.*, Refs. 1–11) while current diagnostic ultrasound scanners employ wideband time-domain signals. The use of wideband information in image reconstruction is known to provide increased point and contrast resolution,[12,13] both of which are important for medical diagnosis.[12,14,15]

Several approaches have been used to incorporate wideband scattering information into quantitative ultrasonic imaging. One group of methods employs time-domain tomography based on Radon-transform relationships that hold (under the assumption of weak scattering) between scattered acoustic fields and the reflectivity or scattering strength of the medium. Pioneering studies in this area[16–18] employed measurements of reflectivity in pulse-echo mode, while later studies have incorporated aberration correction[19,20] and multiple-angle scattering measurements.[21–23] A limitation of these methods, however, is that the Radon transform relationship strictly holds only when the medium is insonified by an impulsive (infinite bandwidth) wave. When pulses of finite bandwidth are employed, image quality can degrade significantly.[24]

A number of linear and nonlinear diffraction tomography methods have been implemented using scattering data for a number of discrete frequencies (*e.g.*, Refs. 25–32). Although use of multiple-frequency data provides improvements in image quality, computational requirements for multiple-frequency imaging are typically large because the computational cost is proportional to the number of frequencies employed. To achieve image quality competitive with present diagnostic scanners, together with quantitative imaging of tissue properties, present frequency-domain methods may require solution of the inverse scatter-

ing problem for many frequencies within the bandwidth of the transducer employed. This approach thus demands a high computational cost, so that high-quality real-time imaging may not be presently feasible using current frequency-domain inverse scattering methods.

Very few previous workers have investigated direct use of time-domain waveform data for inverse scattering methods analogous to frequency-domain diffraction tomography. Several methods[33,34] have used frequency decomposition of scattered pulses to construct a wideband estimate of the spatial Fourier transform of an unknown medium; after appropriate averaging and interpolation, this transform can be inverted to obtain a wideband Born reconstruction of the medium. A study reported in Ref. 35 has showed that broadband synthetic aperture imaging using linear arrays is closely related to inverse scattering using filtered backpropagation. Another method, suggested in Ref. 36, provides a time-domain reconstruction algorithm that employs filtered backpropagation of scattered fields measured on a circular boundary. However, the time domain reconstruction formula of Ref. 36 yields reconstructions that are less general than multiple-frequency reconstructions obtained using the same signal bandwidth.

The present paper offers a new approach to wideband quantitative imaging: a time-domain inverse scattering method that overcomes some of the limitations of previous frequency-domain and time-domain quantitative imaging methods. The new method provides tomographic reconstructions of unknown scattering media using the entire available bandwidth of the signals employed. Reconstructions are performed using scattering data measured on a surface surrounding the region of interest, so that the method is well suited to ultrasonic mammography. The reconstruction algorithm is derived as a simple delay-and-sum formula similar to synthetic-aperture algorithms employed in conventional clinical scanners. However, unlike current clinical scanners, the present method can provide quantitative images of tissue properties such as the spatially-dependent sound speed. Reconstructions obtained in this manner are equivalent to reconstructions obtained by combining conventional frequency-domain diffraction tomography reconstructions for all frequencies within the signal bandwidth of interest. The current method, however, can be even more efficient than single-frequency diffraction tomography. The method is applicable both to two-dimensional and three-dimensional image reconstruction. The direct time-domain nature of the reconstruction algorithm allows straightforward incorporation of depth- and frequency- dependent amplitude correction to compensate for medium absorption as well as aberration correction methods to overcome limits set by the Born approximation.

I. THEORY

A. The time-domain reconstruction algorithm

An inverse scattering algorithm, applicable to quantitative imaging of tissue and other inhomogeneous media, is derived below. For simplicity of derivation, the medium is modeled as a fluid medium defined by the sound speed variation

$$\gamma(\mathbf{r}) = \frac{c_0^2}{c(\mathbf{r})^2} - 1, \tag{1}$$

where c_0 is a background sound speed and $c(\mathbf{r})$ is the spatially-dependent sound speed defined at all points $\mathbf{r}$. For the scope of the initial derivation, the medium is assumed to have constant density, no absorption, and weak scattering characteristics; extensions to the reconstruction algorithm that overcome these limiting assumptions are discussed in the following section.

For the model of the scattering medium represented by Eq. (1), the time-domain scattered acoustic pressure $p_s(\mathbf{r}, t)$ obeys the wave equation[37]

$$\nabla^2 p_s(\mathbf{r}, t) - \frac{1}{c_0^2} \frac{\partial^2 p_s(\mathbf{r}, t)}{\partial t^2} = \frac{\gamma(\mathbf{r})}{c_0^2} \frac{\partial^2 p(\mathbf{r}, t)}{\partial t^2}, \tag{2}$$

where $p(\mathbf{r}, t)$ is the total acoustic pressure in the medium.

The scattering configuration considered here is sketched in Fig. 1. The medium is subjected to a pulsatile plane wave propagating in the direction of the unit vector $\boldsymbol{\alpha}$,

$$p_{\text{inc}}(\mathbf{r}, \boldsymbol{\alpha}, t) = f(t - \mathbf{r} \cdot \boldsymbol{\alpha}/c_0), \tag{3}$$

where f is the time-domain waveform and c_0 is the background sound speed. The scattered wavefield $p_s(\boldsymbol{\theta}, \boldsymbol{\alpha}, t)$ is measured at a fixed radius R in the far field, where $\boldsymbol{\theta}$ corresponds to the direction vector of a receiving transducer element. (Alternatively, if scattering measurements are made in the near field, the farfield acoustic pressure can be computed using exact transforms that represent propagation through a homogeneous medium.[25])

A general time-domain solution for the wave equation (2), valid for two-dimensional (2D) or three-dimensional (3D) scattering, is then

$$p_s(\boldsymbol{\theta}, \boldsymbol{\alpha}, t) = \int_{-\infty}^{\infty} \hat{p}_s(\boldsymbol{\theta}, \boldsymbol{\alpha}, \omega) \, e^{-i\omega t} \, d\omega, \tag{4}$$

where $\hat{p}_s(\boldsymbol{\theta}, \boldsymbol{\alpha}, \omega)$ is a single frequency component of the scattered wavefield,

$$\hat{p}_s(\boldsymbol{\theta}, \boldsymbol{\alpha}, \omega) \equiv \frac{1}{2\pi} \int_{-\infty}^{\infty} p_s(\boldsymbol{\theta}, \boldsymbol{\alpha}, t) \, e^{i\omega t} \, dt, \tag{5}$$

given exactly by[37]

$$\hat{p}_s(\boldsymbol{\theta}, \boldsymbol{\alpha}, \omega) = k^2 \, \hat{f}(\omega) \int G_0(R\boldsymbol{\theta} - \mathbf{r}_0, \omega) \, \gamma(\mathbf{r}_0) \, \hat{p}(\mathbf{r}, \alpha, \omega) \, dV_0. \tag{6}$$

In Eq. (6), k is the wavenumber ω/c_0 and $\hat{p}(\mathbf{r}_0, \boldsymbol{\alpha}, \omega)$ is the total acoustic pressure associated with the unit-amplitude incident plane wave $e^{ik\boldsymbol{\alpha}\cdot\mathbf{r}_0}$. The integral in Eq. (6) is taken over the entire support of γ in $\Re^2$ for 2D scattering or in $\Re^3$ for 3D scattering. The free-space Green's function, represented by G_0 in Eq. (6), is[38]

$$G_0(\mathbf{r}, \omega) = \frac{i}{4} \, H_0^{(1)}(kr) \quad \text{for 2D scattering and}$$

$$G_0(\mathbf{r}, \omega) = \frac{e^{ikr}}{4\pi r} \quad \text{for 3D scattering,} \tag{7}$$

where $H_0^{(1)}$ is the zeroth-order Hankel function of the first kind and r is the magnitude of the vector $\mathbf{r}$.

The farfield scattered pressure, when specified for all incident-wave directions $\boldsymbol{\alpha}$, measurement directions $\boldsymbol{\theta}$, and times t, comprises the data set to be used for reconstruction of the unknown medium $\gamma(\mathbf{r})$. The inverse scattering problem is to reconstruct $\gamma(\mathbf{r})$ using this measured data. The starting point for the present time-domain inverse scattering method is conventional single-frequency diffraction tomography, which can be performed using any frequency component of the measured farfield scattering.

Under the assumption of weak scattering, one can make the Born approximation, in which the total pressure $\hat{p}(\boldsymbol{\alpha}, \omega)$ in Eq. (6) is replaced by the plane wave $e^{ik\mathbf{r}\cdot\boldsymbol{\alpha}}$. For scattering measurements made at a radius R in the far field, linearized inversion of Eq. (6) for any frequency component can then be performed using filtered backpropagation,[4,25,39,40] *i.e.*,

$$\gamma_B(\mathbf{r}, \omega) = \frac{\hat{\mu}(\omega) \, e^{-ikR}}{\hat{f}(\omega)} \iint \Phi(\boldsymbol{\theta}, \boldsymbol{\alpha}) \, \hat{p}_s(\boldsymbol{\theta}, \alpha, \omega) \, e^{ik(\boldsymbol{\theta}-\boldsymbol{\alpha})\cdot\mathbf{r}} \, dS_\alpha \, dS_\theta, \tag{8}$$

where

$$\hat{\mu}(\omega) = -\sqrt{\frac{ikR}{8\pi^3}}, \quad \Phi(\boldsymbol{\theta}, \boldsymbol{\alpha}) = |\sin(\theta - \alpha)| \quad \text{in 2D, and}$$

$$\hat{\mu}(\omega) = \frac{kR}{4\pi^3}, \quad \Phi(\boldsymbol{\theta}, \boldsymbol{\alpha}) = |\boldsymbol{\theta} - \boldsymbol{\alpha}| \quad \text{in 3D.} \tag{9}$$

Each surface integral in Eq. (8) is performed over the entire measurement circle for the 2D case and over the entire measurement sphere for the 3D case.

Equation (8) provides an exact solution to the linearized inverse scattering problem for a single frequency component of the scattered wavefield $p_s(\boldsymbol{\theta}, \boldsymbol{\alpha}, t)$. Instead of seeking a solution for $\gamma(\mathbf{r})$ that exactly satisfies the linearized time-domain inverse scattering problem, the method outlined here constructs a "compounded" $\gamma(\mathbf{r})$ by integrating single-frequency reconstructions $\gamma(\mathbf{r}, \omega)$ over a range of frequencies ω. A generalized formula for this approach can be written

$$\gamma_M(\mathbf{r}) = \frac{\int_0^\infty \hat{g}(\omega)\, \gamma_B(\mathbf{r}, \omega)\, d\omega}{\int_0^\infty \hat{g}(\omega)\, d\omega,} \tag{10}$$

where $\hat{g}(\omega)$ is an appropriate frequency-dependent weighting function.

Using Eq. (8), and making the definition

$$N \equiv 2 \int_0^\infty \hat{g}(\omega)\, d\omega, \tag{11}$$

Eq. (10) can be written in the form

$$\gamma_M(\mathbf{r}) = \frac{2}{N} \int_0^\infty \hat{g}(\omega)\, \frac{\hat{\mu}(\omega)\, e^{-ikR}}{\hat{f}(\omega)} \iint \Phi(\boldsymbol{\theta}, \boldsymbol{\alpha})\, \hat{p}_s(\boldsymbol{\theta}, \boldsymbol{\alpha}, \omega)\, e^{ik(\boldsymbol{\theta}-\boldsymbol{\alpha})\cdot\mathbf{r}}\, dS_\alpha\, dS_\theta\, d\omega. \tag{12}$$

If the frequency weight $\hat{g}(\omega)$ is now specified to incorporate the incident-pulse spectrum $\hat{f}(\omega)$ and to compensate for the frequency- and dimension-dependent coefficient $\hat{\mu}(\omega)$,

$$\hat{g}(\omega) = \hat{f}(\omega)/\hat{\mu}(\omega), \tag{13}$$

Eq. (12) reduces to the form

$$\gamma_M(\mathbf{r}) = \frac{2}{N} \iint \Phi(\boldsymbol{\theta}, \boldsymbol{\alpha}) \int_0^\infty \hat{p}_s(\boldsymbol{\theta}, \boldsymbol{\alpha}, \omega) e^{-ik[R+(\boldsymbol{\alpha}-\boldsymbol{\theta})\cdot\mathbf{r}]}\, d\omega\, dS_\alpha\, dS_\theta. \tag{14}$$

Equation (14) can be rewritten using the definition of $\hat{p}_s(\boldsymbol{\theta}, \boldsymbol{\alpha}, \omega)$ from Eq. 5 to yield the time-domain expression

$$\gamma_M(\mathbf{r}) = \frac{1}{N} \iint \Phi(\boldsymbol{\theta}, \boldsymbol{\alpha}) \, \mathbf{L}\left[p_s\left(\boldsymbol{\theta}, \alpha, R/c_0 + \frac{(\boldsymbol{\alpha}-\boldsymbol{\theta})\cdot\mathbf{r}}{c_0}\right) \right] dS_\alpha\, dS_\theta, \tag{15}$$

where $\mathbf{L}$ denotes the linear operator

$$\mathbf{L}\left[\psi(t)\right] = 2 \int_0^\infty \hat{\psi}(\omega) e^{-i\omega t}\, d\omega \tag{16}$$

and $\hat{\psi}(\omega)$ is the Fourier transform of $\psi(t)$ using the definition from Eq. (5).

Using the conjugate symmetry of $\hat{\psi}(\omega)$ [*i.e.*, $\hat{\psi}(\boldsymbol{\theta}, \boldsymbol{\alpha}, \omega) = \hat{\psi}^*(\boldsymbol{\theta}, \boldsymbol{\alpha}, -\omega)$ for any real $\psi(t)$], the real part of $\mathbf{L}[\psi(t)]$ is shown to be simply $\psi(t)$. Similarly, using the convolution theorem

as well as the conjugate symmetry of $\psi(t)$, the imaginary part of $\mathbf{L}[\psi(t)]$ is seen to be an inverse Hilbert transform[41] of $\psi(t)$,

$$\mathrm{Im}\left[\mathbf{L}\left[\psi(t)\right]\right] = -\frac{1}{\pi}\int_{-\infty}^{\infty}\frac{\psi(\tau)}{t-\tau}\,d\tau = \mathbf{H}^{-1}\left[\psi(t)\right]. \tag{17}$$

This transform, also known as a quadrature filter, applies a phase shift of $\pi/2$ to each frequency component of the input signal.

Thus, the time-domain reconstruction formula can finally be written

$$\gamma_M(\mathbf{r}) = \frac{1}{N}\iint \Phi(\boldsymbol{\theta},\boldsymbol{\alpha})\left(p_s(\boldsymbol{\theta},\alpha,\tau) + i\mathbf{H}^{-1}\left[p_s(\boldsymbol{\theta},\alpha,\tau)\right]\right)\,dS_\alpha\,dS_\theta, \tag{18}$$

where

$$\tau = R/c_0 + \frac{(\boldsymbol{\alpha}-\boldsymbol{\theta})\cdot\mathbf{r}}{c_0}. \tag{19}$$

The direction-dependent weight $\Phi(\boldsymbol{\theta},\boldsymbol{\alpha})$, which is the same as the "filter" employed in single-frequency filtered backpropagation, is given for the 2D and 3D cases by Eq. (9).

Equation 18 is notable in several respects. First, it provides a linearized reconstruction that employs scattering information from the entire signal bandwidth without any frequency decomposition of the scattered wavefield. Second, the delay term τ corresponds exactly to the delay required to construct a focus at the point $\mathbf{r}$ by delaying and summing the scattered wavefield $p_s(\boldsymbol{\theta},\boldsymbol{\alpha},t)$ for all measurement directions $\boldsymbol{\theta}$ and incident-wave directions $\boldsymbol{\alpha}$. Thus, the time-domain reconstruction formula given by Eq. (18) can be regarded as a quantitative generalization of confocal time-domain synthetic aperture imaging, in which signals are synthetically delayed and summed for each transmit/receive pair to focus at the image point of interest.[35,42–45]

A reconstruction formula similar to, although less general than, Eq. 18 was independently derived in Ref. 36 for the two-dimensional inverse scattering problem. In view of the present derivation, the method of "probing by plane pulses" in Ref. 36 can be regarded to yield a frequency-compounded reconstruction of $\mathrm{Re}\left[\gamma_M(\mathbf{r})\right]$, while the present method yields the complex function $\gamma_M(\mathbf{r})$. In Ref. 36, this method was proposed as a more convenient way to implement narrow-band diffraction tomography. However, the numerical results given below show that the reconstruction formula of Eq. 18, when directly implemented using wideband signals, provides considerable improvement in image quality over narrow-band reconstructions.

Reconstructions using Eq. (18) can be performed using any pulse waveform. However, the frequency compounding defined by Eq. (10) is most straightforwardly interpreted if the frequency weight $\hat{g}(\omega)$ has a phase that is independent of frequency. This criterion can be met, for instance, if the incident pulse waveform $f(t)$ is even in time,

$$f(t) = f(-t), \tag{20}$$

so that $\hat{f}(\omega)$ is purely real. (Similarly, if the incident pulse waveform is odd in time, $\hat{f}(\omega)$ is purely imaginary and Eq. (18) can still be employed.)

However, supposition of a frequency-independent phase for $\hat{f}(\omega)$ does not result in any loss of generality. For any linear-phase signal, such that the Fourier transform has the form

$$\hat{f}(\omega) = |\hat{f}(\omega)|\, e^{i\omega\zeta}, \quad \omega > 0, \tag{21}$$

an additional delay term of magnitude ζ can be applied to all scattered signals to obtain the signals associated with the purely-real spectrum $|\hat{f}(\omega)|$. In general, the scattered field associated with a desired waveform $f(t)$ can be determined for an arbitrary waveform $u(t)$ from the deconvolution operation

$$[p_s(\boldsymbol{\theta}, \boldsymbol{\alpha}, t)]_{f(t)} = \mathbf{F}^{-1}\left[\frac{\hat{f}(\omega)}{\hat{u}(\omega)}\, [p_s(\boldsymbol{\theta}, \boldsymbol{\alpha}, t)]_{u(t)} \cdot\right] \tag{22}$$

For stable deconvolution using Eq. (22), the desired $\hat{f}(\omega)$ should not have significant frequency components outside the bandwidth of $\hat{u}(\omega)$.

B. Extensions to the reconstruction algorithm

For large tissue structures at high ultrasonic frequencies, weak scattering approximations such as the Born approximation are of limited validity. Thus, for problems of interest to medical ultrasound imaging, reconstructed image quality can be improved by aberration correction methods that incorporate higher-order scattering and propagation effects. The present time-domain reconstruction formula (18) provides a natural framework for quantitative imaging with aberration correction. In general, if the background medium is known or can be estimated, the received scattered signals can be processed to provide an estimate of the scattered field that would be measured for the same scatterer within a homogeneous background medium. This approach essentially removes higher-order scattering effects from

the measured far field scattering, so that a Born inversion can be performed on the modified data; similar processes occur implicitly in many nonlinear inverse scattering methods.[46]

For example, a simple implementation of aberration correction can be derived if one makes the assumption that background inhomogeneities result only in cumulative delays (or advances) of the incident and scattered wavefronts. This crude model does not include many propagation and scattering effects important to ultrasonic aberration, but has been shown to provide a reasonable first approximation of local delays in wavefronts propagating through large-scale tissue models.[47,48] Given this approximation, the total delay for an angle ϕ and a point position $\mathbf{r}$ is given by

$$\delta\tau(\phi, \mathbf{r}) = \int_\xi c(\boldsymbol{\xi})^{-1} \, d\xi - \frac{R}{c_0} \tag{23}$$

where the integral is performed along the line that joins the spatial points $\mathbf{r}$ and $R\phi$, Aberration-corrected reconstructions can then be performed using Eq. (18) with τ replaced by the corrected delay term

$$\tau \rightarrow R/c_0 + \frac{(\boldsymbol{\alpha} - \boldsymbol{\theta}) \cdot \mathbf{r}}{c_0} + \delta\tau(\boldsymbol{\alpha}, \mathbf{r}) + \delta\tau(\boldsymbol{\theta}, \mathbf{r}). \tag{24}$$

Improved approximations could be obtained by application of the delay function $\delta\tau(\phi, \mathbf{r})$ after numerical backpropagation of the farfield scattered wavefronts through a homogeneous medium[49,50] or by compensation for both delay and amplitude variations.[51,52] More general, although much more computationally expensive, aberration correction could also be performed by synthetic focusing using full-wave numerical computation of acoustic fields within an estimated realization of the unknown medium. This method has been implemented, within the context of a frequency-domain diffraction tomography method, in Ref. 30.

The present imaging method has been derived using simplifying assumptions including zero absorption and constant density for the scattering medium. However, these assumptions do not substantially restrict the validity of the method. For example, the effect of absorption can be reduced using time-gain compensation, with or without frequency-dependent corrections,[53] of received scattered signals for each transmit/receive pair. Such time-gain compensation could be performed either using an estimated bulk attenuation for the medium (as with current clinical ultrasound scanners), or by implementation of an adaptive attenuation model in a manner similar to the time-shift compensation scheme discussed above.

Inclusion of density variations as well as sound speed variations adds additional complication to the time-domain diffraction tomography algorithm derived here. For single-frequency

diffraction tomography in the presence of sound speed and density variations, the quantity $\gamma_B(\mathbf{r}, \omega)$ reconstructed by Eq. 8 can be shown[54] to provide an estimate of a physical quantity that depends both on sound speed variations and density variations. In the notation used here, this quantity can be written

$$\gamma'(\mathbf{r}) = \gamma(\mathbf{r}) - \gamma(\mathbf{r})\gamma_\rho(\mathbf{r}) + \frac{1}{2k^2}\nabla^2\gamma_\rho(\mathbf{r}), \tag{25}$$

where the density variation is defined $\gamma_\rho = 1 - \rho_0/\rho(\mathbf{r})$. Thus, for time-domain reconstructions of media with density variations, the reconstruction formula of Eq. 18 will provide the estimate

$$\gamma_M(\mathbf{r}) \approx \gamma(\mathbf{r}) - \gamma(\mathbf{r})\gamma_\rho(\mathbf{r}) + \frac{1}{2k_0^2}\nabla^2\gamma_\rho(\mathbf{r}), \tag{26}$$

where k_0 is the wavenumber corresponding to the center frequency of the pulse employed. For media such as human tissue, where density variations are fairly small and abrupt density transitions are rare, the last two terms of Eq. (26) are small compared to $\gamma(\mathbf{r})$, so that the reconstruction algorithm derived above can still be regarded to provide an image of the sound-speed variation function $\gamma(\mathbf{r})$. However, if desired, a reconstruction employing pulses with two distinct center frequencies could allow separation of sound speed and density variations by techniques similar to those described in Refs. 25 or 54.

II. COMPUTATIONAL METHODS

The time-domain inverse scattering method described above has been tested with 2D and 3D synthetic data prepared using three numerical methods: a Born approximation method for point scatterers and 3D slabs, an exact series solution for cylindrical inhomogeneities, and a k-space method for arbitrary 2D inhomogeneous media.

The time-domain waveform employed for all the computations reported here was

$$f(t) = \cos(\omega_0 t) \, e^{-t^2/(2\sigma^2)}, \tag{27}$$

where $\omega_0 = 2\pi f_0$ for a center frequency of f_0 and σ is the temporal Gaussian parameter. This waveform has the real, even Fourier transform

$$\hat{f}(\omega) = \sqrt{\frac{\sigma^2}{8\pi}} \left(e^{-\sigma^2(\omega-\omega_0)^2/2} + e^{-\sigma^2(\omega+\omega_0)^2/2} \right) \tag{28}$$

Values used for the compurations reported here were $f_0 = 2.5$ MHz and $\sigma = 0.25$ μs, so that the -6 dB bandwidth of the signal was 1.5 MHz. These parameters correspond closely to those of an existing 2048-element ring transducer.[55]

For the case of point scatterers, the contrast function γ was assumed to take the form

$$\gamma(\mathbf{r}) = \sum_1^M \mu_j \, \delta(\mathbf{r} - \mathbf{r_j}). \tag{29}$$

Using the farfield form of the 2D Green's function and neglecting multiple scattering, Eq. (6) for the scattered far field can be rewritten as

$$\hat{p}_s(\boldsymbol{\theta}, \boldsymbol{\alpha}, \omega) = -k^2 \sqrt{\frac{i}{8\pi k R}} \, \hat{f}(\omega) \sum_j \mu_j \, e^{ik(\boldsymbol{\alpha}-\boldsymbol{\theta})\cdot\mathbf{r}_j} \tag{30}$$

for each frequency component of interest. Time-domain waveforms were synthesized by using Eq. (30) for each frequency with $\hat{f}(\omega) > 10^{-3}$ and inverting the frequency-domain scattered wavefield by a fast Fourier transform (FFT) implementation of Eq. (4). The temporal sampling rate employed was 10 MHz. An analogous formula, with a different multiplicative constant, was also employed for the 3D case.

The Born approximation was also used to compute three-dimensional scattering for slab-shaped objects defined by the equation

$$\gamma(\mathbf{r}) = \gamma_0 H(a_x - |x|) H(a_y - |y|) H(a_z - |z|). \tag{31}$$

For this object, the linearized forward problem can be solved analytically. Under the Born approximation, the frequency-domain scattered far field has the form

$$\hat{p}_s(\boldsymbol{\theta}, \boldsymbol{\alpha}, \omega) = 2\,\hat{f}(\omega)\,\gamma_0\,a_x a_y a_z\,e^{ikR}/(\pi R)$$

$$\times \frac{\sin[kL_x\,(\boldsymbol{\alpha}-\boldsymbol{\theta})\cdot\mathbf{e}_x]}{kL_x\,(\boldsymbol{\alpha}-\boldsymbol{\theta})\cdot\mathbf{e}_x}\frac{\sin[kL_y\,(\boldsymbol{\alpha}-\boldsymbol{\theta})\cdot\mathbf{e}_y]}{kL_y\,(\boldsymbol{\alpha}-\boldsymbol{\theta})\cdot\mathbf{e}_y}\frac{\sin[kL_z\,(\boldsymbol{\alpha}-\boldsymbol{\theta})\cdot\mathbf{e}_z]}{kL_z\,(\boldsymbol{\alpha}-\boldsymbol{\theta})\cdot\mathbf{e}_z}, \quad (32)$$

where $\mathbf{e}_x$, $\mathbf{e}_y$, and $\mathbf{e}_z$ represent unit vectors in the x, y, and z directions. The time domain scattered pressure $p_s(\boldsymbol{\theta}, \boldsymbol{\alpha}, t)$ is obtained, as for the point scatterer case described above, by inverse transformation of the frequency-domain wavefield for all frequencies within the bandwidth of interest.

For 2D cylindrical inhomogeneities, an analogous procedure was followed, except that the frequency-domain scattered wavefield $\hat{p}_s(\boldsymbol{\theta}, \boldsymbol{\alpha}, \omega)$ was computed using an exact series solution[37] for each frequency component of interest. In implementation of the series solution, summations were truncated when the magnitude of a single coefficient dropped below 10^{-12} times the sum of all coefficients.

Solutions were also obtained for arbitrary 2D inhomogenous media using a time-domain k-space method.[56] Grid sizes of 256×256 points, a spatial step of 0.0833 mm, and a time step of 0.02734 μs were employed. Scattered acoustic pressure signals on a circle of virtual receivers were recorded at a sampling rate of 9.144 MHz. The receiver circle, which had a radius of 3.0 mm in these computations, completely contained the inhomogeneities used. Farfield waveforms were computed by Fourier transforming the time-domain waveforms on the nearfield measurement circle, transforming these to farfield waveforms for each frequency using a numerically exact transformation method,[25] and performing inverse Fourier transformation to yield time-domain farfield waveforms. All forward and inverse temporal Fourier transforms, as well as angular transforms occurring in the nearfield-farfield transformation,[25] were performed by FFT.

The time-domain imaging method was directly implemented using Eq. (18), evaluated using straightforward numerical integration over all transmit and receive directions employed. The reconstruction formula employed can be explicitly written as

$$\gamma_M(\mathbf{r}) = \frac{1}{N_{2D}} \int_0^{2\pi}\!\!\int_0^{2\pi} |\sin(\alpha-\theta)|\,\left(p_s(\boldsymbol{\theta}, \boldsymbol{\alpha}, \tau) + i\mathbf{H}^{-1}\left[p_s(\boldsymbol{\theta}, \boldsymbol{\alpha}, \tau)\right]\right)\,d\alpha\,d\theta,$$

$$\tau = R/c_0 + \frac{(\cos\alpha - \cos\theta)\cdot x + (\sin\alpha - \sin\theta)\cdot y}{c_0} \quad (33)$$

for the 2D case, where α and θ are the angles corresponding to the direction vectors $\boldsymbol{\alpha}$ and $\boldsymbol{\theta}$, and as

$$\gamma_M(\mathbf{r}) = \frac{1}{N_{3D}} \int_0^{2\pi}\!\!\int_0^{\pi}\!\!\int_0^{2\pi}\!\!\int_0^{\pi} |\boldsymbol{\alpha} - \boldsymbol{\theta}| \left(p_s(\boldsymbol{\theta}, \alpha, \tau) + i\mathbf{H}^{-1}\left[p_s(\boldsymbol{\theta}, \alpha, \tau)\right]\right)$$
$$\times \sin(\Phi_{\boldsymbol{\alpha}}) \sin(\Phi_{\boldsymbol{\theta}})\, d\Phi_{\boldsymbol{\alpha}}\, d\Theta_{\boldsymbol{\alpha}}\, d\Phi_{\boldsymbol{\theta}}\, d\Theta_{\boldsymbol{\theta}}\,,$$
$$\tau = R/c_0 + \frac{(\boldsymbol{\alpha} - \boldsymbol{\theta}) \cdot \mathbf{r}}{c_0},$$
$$\boldsymbol{\alpha} - \boldsymbol{\theta} = (\cos\Theta_{\boldsymbol{\alpha}} \sin\Phi_{\boldsymbol{\alpha}} - \cos\Theta_{\boldsymbol{\theta}} \sin\Phi_{\boldsymbol{\theta}}) \cdot \mathbf{e}_x + (\sin\Theta_{\boldsymbol{\alpha}} \sin\Phi_{\boldsymbol{\alpha}} - \sin\Theta_{\boldsymbol{\theta}} \sin\Phi_{\boldsymbol{\theta}}) \cdot \mathbf{e}_y$$
$$+ (\cos\Phi_{\boldsymbol{\alpha}} - \cos\Phi_{\boldsymbol{\theta}}) \cdot \mathbf{e}_z \tag{34}$$

for the 3D case, where $\Theta_{\boldsymbol{\alpha}}$ and $\Phi_{\boldsymbol{\alpha}}$ are direction angles for the incident-wave direction $\boldsymbol{\alpha}$ and $\Theta_{\boldsymbol{\theta}}$ and $\Phi_{\boldsymbol{\theta}}$ are direction angles for the measurement direction $\boldsymbol{\theta}$. For each case, the normalization factor N was determined from Eq. 11 with $\hat{g}(\omega) = \hat{f}(\omega)/\hat{\mu}(\omega)$ and $\mu(\omega)$ given by Eq. 9. Before evaluation of the argument τ for each signal, the time-domain waveforms were resampled at a sampling rate of 16 times the original rate. This resampling was performed using FFT-based Fourier interpolation. The inverse Hilbert transform was performed for each signal using an FFT implementation of Eq. (16). Values of the pressure signals at the time τ were then determined using linear interpolation between samples of the resampled waveforms. The integrals of Eqs. (33) and (34) were implemented using discrete summation over all transmission and measurement directions employed.

Computations were also performed using the time-domain diffraction tomography algorithm for limited-aperture data. For these reconstructions, the integrals of Eq. (33) were evaluated only for angles corresponding to transmitters and receivers within a specified aperture of angular width ϕ_{ap}, *i.e.*,

$$|\alpha| \leq \phi_{\text{ap}}/2,$$
$$|\theta - \pi| \leq \phi_{\text{ap}}/2, \tag{35}$$

Use of a small value for ϕ_{ap} corresponds to use of a small aperture in pulse-echo mode.

III. NUMERICAL RESULTS

Two-dimensional and three-dimensional point-spread functions (PSF) for the present time-domain diffraction tomography method are illustrated in Fig. 2. The time-domain reconstructions shown here, like the other time-domain reconstructions shown in this paper, were obtained using a incident pulse of center frequency 2.5 MHz and a Gaussian envelope corresponding to a −6 dB bandwidth of 1.5 MHz. Point-spread functions were determined by reconstructing a point scatterer located at the origin. For the 2D case, in which the point scatterer can be regarded as a thin wire, synthetic scattering data was obtained using the Born approximation method outlined above for 16 incident-wave directions and 64 measurement directions. The 3D time-domain reconstruction was obtained using Born data for 72 incident-wave directions and 288 measurement directions, each evenly spaced on a rectangular grid defined by the angles Θ and Φ. For comparison, analogous point-spread functions are also shown for standard frequency-domain diffraction tomography reconstructions with single-frequency (2.5 MHz) data.

For the 2D case illustrated in Fig. 2, the time-domain reconstruction has a slightly narrower peak, indicating that point resolution has been slightly improved by the increased bandwidth employed in the time domain method. More significantly, sidelobes of the time-domain PSF are dramatically smaller than those for the frequency-domain PSF, so that contrast resolution for time-domain diffraction tomography is seen to be much higher than for single-frequency diffraction tomography. For the 3D case, the time-domain reconstruction shows a much more dramatic improvement over the frequency-domain reconstruction. In this case, both the point resolution and the contrast resolution are significantly higher for time-domain reconstruction than for single-frequency reconstruction. Furthermore, a comparison of the PSF's for 2D and 3D time-domain reconstruction indicates that much higher image quality is achievable for 3D time-domain imaging than for the 2D case. This increase in image quality suggests that the time-domain diffraction tomography method proposed here may benefit from the overdetermined nature of the general wideband 3D inverse scattering problem.[57,58]

The effect of transmit and receive aperture characteristics on image quality is illustrated in Fig. 3, which shows the point-spread function for a number of aperture configurations. All of these reconstructions employed 64 measurement directions, which were found to adequately sample the scattered far field for a single transmit direction. Figure 3(a) shows

the point-spread function for reconstructions obtained using 1, 4, 8, and 16 incident-wave directions. The point scatterer is clearly imaged even for the reconstruction using one incident-wave direction. Optimal image quality (indistinguishable from reconstructions with 64 incident-wave directions) is obtained for 16 incident-wave directions, so that scattering data obtained using one incident-wave direction for each group of four measurement directions appears to be sufficient for the present reconstruction method. The effect of limited view range on the point spread function is illustrated in Fig. 3. Limitation of the transmit and recieve apertures to angles near the backscatter direction (aperture size $\pi/2$) results in an image that resembles a conventional B-scan. Use of an aperture corresponding to pulse-echo mode in the large-aperture limit (aperture size π) yields higher resolution in all directions. Using three fourths of a circular aperture (size $3\pi/2$) yields image quality close to that for the full aperture (2π) case.

Reconstructions performed using exact solutions for scattering from cylindrical inhomogeneities provide a straightforward means to assess the accuracy of the time-domain scattering method for a range of object sizes and contrasts. Cross sections of time-domain and single-frequency reconstructions, plotted in Fig. 4, show the relative accuracy of each reconstruction method for a cylinder of 1 mm radius and purely real contrast ranging from $\gamma = 0.02$ to $\gamma = 0.08$. For the synthetic scattering data in each case, 96 measurement directions and 24 incident-wave directions were employed. The time-domain reconstructions show improvement over the single-frequency reconstructions both in improved contrast resolution (smaller sidelobes outside the support of the cylinder) and in decreased ripple (Gibbs phenomenon) artifacts within the support of the cylinder. However, for increasing contrast values, both methods show similar increases in phase error, as indicated by increased imaginary parts of the reconstructed contrast.

Further testing of accuracy for the time-domain reconstruction method is shown in Fig. 5. Real parts of time-domain reconstructions are shown for cylinder radii between 1 mm and 4 mm with contrasts between $\gamma = 0.02$ and $\gamma = 0.08$. The number of measurement directions employed for the synthetic scattering data was 96 for the 1 mm radius cylinders, 192 for the 2 mm cylinders, 288 for the 3 mm cylinders, and 384 for the 4 mm cylinders. In each case, four incident-wave directions per measurement direction were used. Using the wavenumber $k_0 = 10.472$ rad/mm corresponding to the center frequency of 2.5 MHz and a sound speed of 1.5 mm/μs, the reconstructions shown in Fig. 5 indicate that the interior of the cylinder is imaged satisfactorily for the approximate range $ka \times \gamma < 2.5$. This result is consistent with

a previous study of single-frequency diffraction tomography, which showed that adequate Born reconstructions of cylinders were obtained for the parameter range $ka \times \gamma \leq 2.2$.[59]

Reconstructions for several scattering objects without special symmetry are shown in Fig. 6. All of these reconstructions were performed using synthetic data produced by the k-space method described in Ref. 56. Synthetic scattering data were computed for 64 incident-wave directions and 256 measurement directions in each case. The first panel shows a reconstruction of a cylinder of radius 2.5 mm and contrast $\gamma = -0.0295$ with an internal cylinder of radius 0.2 mm and contrast $\gamma = 0.0632$. The second panel shows a reconstruction of a 2.5 mm-radius cylinder with random internal structure. The third reconstruction shown employed a portion of a chest wall tissue map from Ref. 60. In this case, the synthetic data was obtained using a tissue model[60] that incorporates both sound speed and density variations, so that the reconstructed quantity is given by Eq. (26).

The real part of each reconstruction shows good image quality, with high resolution and very little evidence of artifacts. Particularly notable is the accurately detailed imaging of internal structure for the random cylinder and the chest wall cross section. As expected, the density variations present in the chest wall cross section have not greatly affected the image appearance; there is, however, a slight edge enhancement, associated with the Laplacian term in Eq. (26), at boundaries between tissue regions. Also notable is the nearly-complete absence of any artifacts outside the scatterer in each case; this result indicates that high contrast resolution has been achieved. However, in each case, the imaginary part of the reconstruction is nonzero, indicating that the Born approximation is not fully applicable. Aberration correction methods [of which a simple example is given by Eq. (24)] could substantially reduce this phase error, as for multiple-frequency diffraction tomography in Ref. 30.

Three-dimensional reconstructions of a homogeneous slab are shown in Fig. 7. The scatterer is characterized by Eq. (31) with $\gamma_0 = 0.01$, $a_x = 0.5$ mm, $a_y = 1.0$ mm, and $a_z = 1.5$ mm. Synthetic data was computed using Eq. 34 for 288 transmit directions and 1152 measurement directions, each evenly spaced in the angles Φ and Θ. Signal parameters were as for the examples above, except that the initial sampling rate for the time-domain signals was 9.0 MHz. Isosurface renderings of the real part of γ_M are shown for the surfaces $\gamma_M = 0.0025$. Since the scattering data were obtained using a Born approximation for the 3D case, the imaginary part of each reconstruction is identically zero for both reconstructions. Consistent with the point-spread functions shown in Fig. 2, the time-domain

reconstruction is much more accurate than the single-frequency reconstruction. While the single-frequency reconstruction shows an erroneously rippled surface, the time-domain reconstruction is smooth. The time-domain reconstruction is nearly identical to the original object except for some rounding of edges due to the limited high-frequency content of the signal employed.

Since three-dimensional inverse scattering is a computationally demanding problem, comparison of computational efficiency for single-frequency and time-domain methods is of interest. For both reconstructions shown in Fig. 7, identical discretizations of the reconstructed medium were employed. Both computations included solution of the applicable linearized forward problem as well as the inverse problem. Nonetheless, the time-domain method was more efficient than the single-frequency method; the total CPU time required on a 200 MHz AMD K6 processor was 133.3 CPU min for the time-domain method and 287.4 CPU minutes for the single-frequency method. This gain in efficiency was possible because the greatest computational expense occurred in the "backpropagation" of the signals for each reconstruction point. For the single-frequency method, this step required evaluation of complex exponentials for each transmit direction, measurement direction, and spatial point. For the time-domain method, however, the computationally intensive steps (including the forward problem solution and Fourier interpolation of the scattered signals) needed only to be performed once for each transmit/receive pair. For the backpropagation step, performed at each point in the 3D spatial grid, the time-domain reconstruction method required only linear interpolation of the oversampled farfield pressure waveforms.

IV. CONCLUSIONS

A new method for time-domain ultrasound diffraction tomography has been presented. The method provides quantitative images of sound speed variations in unknown media; when two pulse center frequencies are employed, the method is also capable of imaging density variations. Reconstructions performed using this method are equivalent to multiple-frequency reconstructions using filtered backpropagation, but can be obtained with much greater efficiency.

The time-domain reconstruction algorithm has been derived as a simple filtered delay-and-sum operation applied to farfield scattered signals. This algorithm is closely related to time-domain confocal synthetic aperture imaging, so that it can be considered a generalization of imaging algorithms employed in current clinical instruments. The simplicity of the imaging algorithm allows straightforward addition of features such as time-gain compensation and aberration correction.

Numerical results obtained using synthetic data for 2D and 3D scattering objects show that the time-domain method can yield significantly higher image quality (and, in some cases, also greater efficiency) than single-frequency diffraction tomography. Quantitative reconstructions, obtained using signal parameters comparable to those for present-day clinical instruments, show accurate imaging of objects with simple deterministic structure, random internal structure, and structure based on a cross-sectional tissue model. The method is hoped to be useful for diagnostic imaging problems such as the detection and characterization of lesions in ultrasonic mammography.

ACKNOWLEDGMENTS

REFERENCES

[1] E. Wolf, "Three-dimensional structure determination of semi-transparent objects from holographic data," Optics Comm. **1**, 153–156 (1969).

[2] P.-C. Ho and W. H. Carter, "Structural measurement by inverse scattering in the first Born approximation," Applied Optics **15**, 313–314 (1976).

[3] R. K. Mueller, M. Kaveh, and G. Wade, "Reconstructive tomography and applications to ultrasonics," Proc. IEEE **67**, 567–587 (1979).

[4] A. J. Devaney, "A filtered backpropagation algorithm for diffraction tomography," Ultrason. Imag. **4**, 336–350 (1982).

[5] J. M. Blackledge and L. Zapalowski, "Quantitative solutions to the inverse scattering problem with applications to medical imaging," Inverse Problems **1**, 17–32 (1985).

[6] M. Soumekh, "An improvement to the Rytov approximation in diffraction tomography," IEEE Trans. Ultrason. Ferrolectr. Freq. Contr. **33**, 394–401 (394–401).

[7] A. Witten, J. Tuggle, and R. C. Waag, "Ultrasonic imaging with a fixed instrument configuration," Appl. Phys. Lett. **53**, 16–18 (1988).

[8] D. T. Borup, S. A. Johnson, W. W. Kim, and M. J. Berggren, "Nonperturbative diffraction tomography via Gauss-Newton iteration applied to the scattering integral equation," Ultrason. Imag. **14**, 69–85 (1992).

[9] S. Gutman and M. Klibanov, "Two versions of quasi-Newton method for multidimensional inverse scattering problem," J. Comp. Acoust. **1**, 197–228 (1993).

[10] N. Sponheim, L.-J. Gelius, I. Johansen, and J. J. Stamnes, "Ultrasound tomography of biological tissue," Ultrason. Imag. **16**, 19–32 (1994).

[11] C. W. Manry and S. L. Broschat, "Inverse imaging of the breast with a material classification technique," J. Acoust. Soc. Am. **103**, 1538–1546 (1998).

[12] F. W. Kremkau, *Diagnostic Ultrasound: Physical Principles and Exercises* (Grune and Stratton, New York, 1980).

[13] J. L. Schwartz and B. D. Steinberg, "Ultrasparse, ultrawideband arrays," IEEE Trans. Ultrason. Ferrolectr. Freq. Contr. **45**, 376–393 (1998).

[14] S. H. Maslak, "Computed sonography," in *Ultrasound Annual 1985* (Raven, New York, 1985), pp. 1–16.

[15] E. L. Madsen, J. A. Zagzebski, and G. R. Frank, *AIUM Quality Control Manual for Gray-Scale Ultrasound Scanners* (American Institute of Ultrasound in Medicine, Rockville Center, Maryland, 1995).

[16] S. J. Norton, "Reconstruction of a reflectivity field from line integrals over circular paths," J. Acoust. Soc. Am. **67**, 853–863 (1980).

[17] S. J. Norton, "Reconstruction of a two-dimensional reflecting medium over a circular domain: exact solution," J. Acoust. Soc. Am. **67**, 1266–1273 (1980).

[18] S. J. Norton and M. Linzer, "Ultrasonic reflectivity imaging in three dimensions: exact inverse scattering solutions for plane, cylindrical, and circular apertures," IEEE Trans. Biomed. Eng. **28**, 202–220 (1980).

[19] J. H. Kim, S. B. Park, and S. A. Johnson, "Tomographic imaging of ultrasonic reflectivity with correction for acoustic speed variations," Ultrasonic Imaging **6**, 304–312 (1984).

[20] C. Q. Lan and W. Xiong, "An iterative method of ultrasonic reflection mode tomography," IEEE Trans. Med. Imag. **13**, 419–425 (1994).

[21] D. Miller, M. Oristaglio, and G. Beylkin, "A new slant on seismic imaging: migration and internal geometry," Geophysics **52**, 943–964 (1987).

[22] T. Melamed, Y. Ehrlich and E. Heymann, "Short-pulse inversion of inhomogeneous media: a time-domain diffraction tomography," Inverse Problems **12**, 977–993 (1996).

[23] T. Melamed and E. Heymann, "Spectral analysis of time-domain diffraction tomography," Radio Science **32**, 593–603 (1997).

[24] S. Pourjavid and O. Tretiak, "Ultrasound imaging through time-domain diffraction tomography," IEEE Trans. Ultrason. Ferrolectr. Freq. Contr. **38**, 74–85 (1991).

[25] A. Witten, J. Tuggle, and R. C. Waag, "A practical approach to ultrasonic imaging using diffraction tomography," J. Acoust. Soc. Am. **83**, 1645–1652 (1988).

[26] T. J. Cavicchi and W. D. O'Brien, "Numerical study of higher-order diffraction tomography via the sinc basis moment method," Ultrasonic Imaging **11**, 42–74 (1989).

[27] H. Gan, R. Ludwig, and P. L. Levin, "Nonlinear diffractive inverse scattering for multiple scattering in inhomogeneous acoustic background media," J. Acoust. Soc. Am. **97**, 764–776 (1995).

[28] C. Lu, J. Lin, W. Chew, and G. Otto, "Image reconstruction with acoustic measurement using distorted Born iteration method," Ultrason. Imag. **18**, 140–156 (1996).

[29] A. V. Osetrov and S. N. Samolenkov, "Two models of acoustic scatterers in diffraction tomography," Acoustical Physics **42**, 598–605 (1996).

[30] T. D. Mast, A. I. Nachman, and R. C. Waag, "Focusing and imaging using eigenfunctions of the scattering operator," *J. Acoust. Soc. Am.* **102**, 715–725 (1997).

[31] M. P. André, H. S. Janée, P. J. Martin, G. P. Otto, B. A. Spivey, and D. A. Palmer, "High-speed data acquisition in a diffraction tomography system employing large-scale toroidal arrays," Int. J. Imag. Syst. Tech. **8**, 137–147 (1997).

[32] O. S. Haddadin and E. S. Ebbini, "Imaging strongly scattering media using a multiple frequency distorted Born iterative method," IEEE Trans. Ultrason. Ferrolectr. Freq. Contr. **45**, 1485–1496 (1998).

[33] J. M. Blackledge, R. E. Burge, K. I. Hopcraft, and R. J. Wombell, "Quantitative diffraction tomography: I. Pulsed acoustic fields," J. Phys. D: Appl. Phys. **20**, 1–10 (1987).

[34] S. Mensah and J.-P. Lefebvre, "Enhanced compressibility tomography," IEEE Trans. Ultrason. Ferrolectr. Freq. Contr. **44**, 1245–1252 (1997).

[35] G. Prokoph and H. Ermert, "A comparison of broadband holographic and tomographic imaging concepts," Acoustical Imaging **18**, 381–390 (1991).

[36] V. A. Burov and O. D. Rumyantseva, "Linearized inverse problem of scattering in monochromatic and pulse modes," Acoustical Physics **40**, 34–42 (1996).

[37] P. M. Morse and K. U. Ingard, *Theoretical Acoustics* (New York, McGraw-Hill, 1968), ch. 8.

[38] P. M. Morse and H. Feshbach, *Methods of Theoretical Physics* (New York: McGraw-Hill, 1953), v. I.

[39] A. J. Devaney, "Inversion formula for inverse scattering within the Born approximation," Optics Lett. **7**, 111–112 (1982).

[40] G. Beylkin, "The fundamental identity for iterated spherical means and the inversion formula for diffraction tomography and inverse scattering," J. Math. Phys. **24**, 1399–1400 (1982).

[41] A. Papoulis, *The Fourier Integral and Its Applications* (McGraw-Hill, New York, 1962), ch. 10.

[42] J. Ylitalo, E. Alasaarela, and J. Koivukangas, "Ultrasound holographic B-scan imaging," IEEE Trans. Ultrason. Ferrolectr. Freq. Contr. **36**, 376–383 (1989).

[43] K. E. Thomenius, "Evolution of ultrasound beamformers," Proc. IEEE Ultrason. Symp. **2**, 1615–1622 (1996).

[44] M. Lang and H. Ermert, "Linear synthetic aperture modes for ultrasonic pulse-echo imaging," Biomed. Technik **42**, 108–115 (1997).

[45] M. O'Donnell, M. J. Eberle, D. N. Stephens, J. L. Litzza, K. S. Vicente, and B. M. Shapo, "Synthetic phased arrays for intraluminal imaging of coronary arteries," IEEE Trans. Ultrason. Ferrolectr. Freq. Contr. **44**, 714–721 (1997).

[46] R. Snieder, "A perturbative analysis of non-linear inversion," Geophys. J. Int. **101**, 545–556 (1990).

[47] T. D. Mast, L. M. Hinkelman, M. J. Orr, V. W. Sparrow, and R. C. Waag, "Simulation of ultrasonic pulse propagation through the abdominal wall," J. Acoust. Soc. Am. **102**, 1177–1190 (1997). [Erratum: J. Acoust. Soc. Am. **104**, 1124–1125 (1998).]

[48] T. D. Mast, L. M. Hinkelman, M. J. Orr, and R. C. Waag, "The effect of abdominal wall morphology on ultrasonic pulse distortion. Part II. Simulations," J. Acoust. Soc. Am. **104**, 3651–3664 (1998).

[49] D.-L. Liu and R. C. Waag, "Correction of ultrasonic wavefront distortion using backpropagation and a reference waveform method for time-shift compensation," J. Acoust. Soc. Am. **96**(2), 649–660 (1994).

[50] C. Dorme and M. Fink, "Ultrasonic beam steering through inhomogeneous layers with a time reversal mirror," IEEE Trans. Ultrason. Ferrolectr. Freq. Control **43**(1), 167–175 (1996).

[51] S. Krishnan, P.-C. Li, and M. O'Donnell, "Adaptive compensation for phase and magnitude aberrations," IEEE Trans. Ultrason. Ferrolectr. Freq. Control **43**(1), 44–55 (1996).

[52] Q. Zhu and B. D. Steinberg, "Deabberation of incoherent wavefront distortion: an approach toward inverse filtering," IEEE Trans. Ultrason. Ferrolectr. Freq. Control **44**, 575–589 (1997).

[53] I. Claesson and G. Salomonsson, "Frequency- and depth-dependent compensation of ultrasonic signals," IEEE Trans. Ultrason. Ferrolectr. Freq. Control **35**, 582–592 (1988).

[54] A. J. Devaney, "Variable density acoustics tomography," J. Acoust. Soc. Am. **78**, 120–130 (1985).

[55] T. T. Jansson, T. D. Mast, and R. C. Waag, "Measurements of differential scattering cross section using a ring transducer," J. Acoust. Soc. Am. **103**, 3169–3179 (1998).

[56] L. P. Souriau, T. D. Mast, D.-L. Liu, R. C. Waag, and A. I. Nachman, "A k-space method for large-scale models of wave propagation in tissue," submitted to IEEE Trans. Ultrason. Ferrolectr. Freq. Contr. (1999).

[57] A. Nachman, "Reconstructions from boundary measurements," Ann. Math. **128**, 531–576 (1988).

[58] D. Colton and R. Kress, *Inverse Acoustic and Electromagnetic Scattering Theory*, Second Edition (Berlin: Springer-Verlag, 1998), Ch. 10.

[59] M. Slaney, A. C. Kak, and L. E. Larsen, "Limitations of imaging with first-order diffraction tomography," IEEE Trans. Microwave Theory Tech. **32**, 860–874 (1984).

[60] T. D. Mast, L. M. Hinkelman, M. J. Orr, and R. C. Waag, "Simulation of ultrasonic pulse propagation, distortion, and attenuation in the human chest wall," submitted to J. Acoust. Soc. Am. (1999).
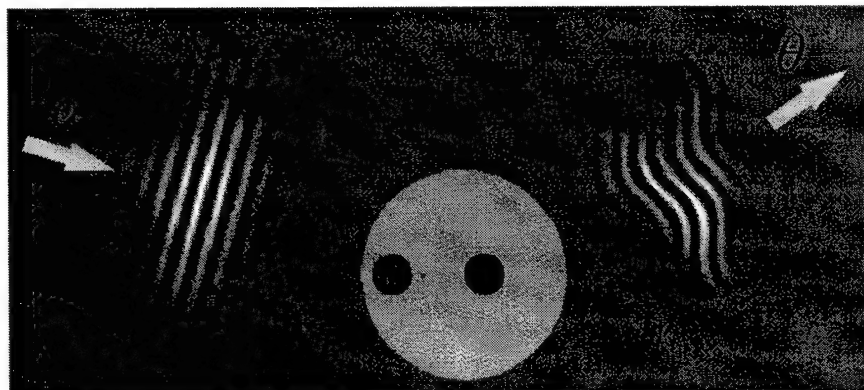
FIGURES

FIG. 1. Scattering configuration. An incident pressure pulse of the form $f(t - \boldsymbol{\alpha} \cdot r/c)$ is scattered by an inhomogeneous medium and the time-domain scattered field $p_s(\boldsymbol{\theta}, \boldsymbol{\alpha}, t)$ is measured at a radius R in the far field.
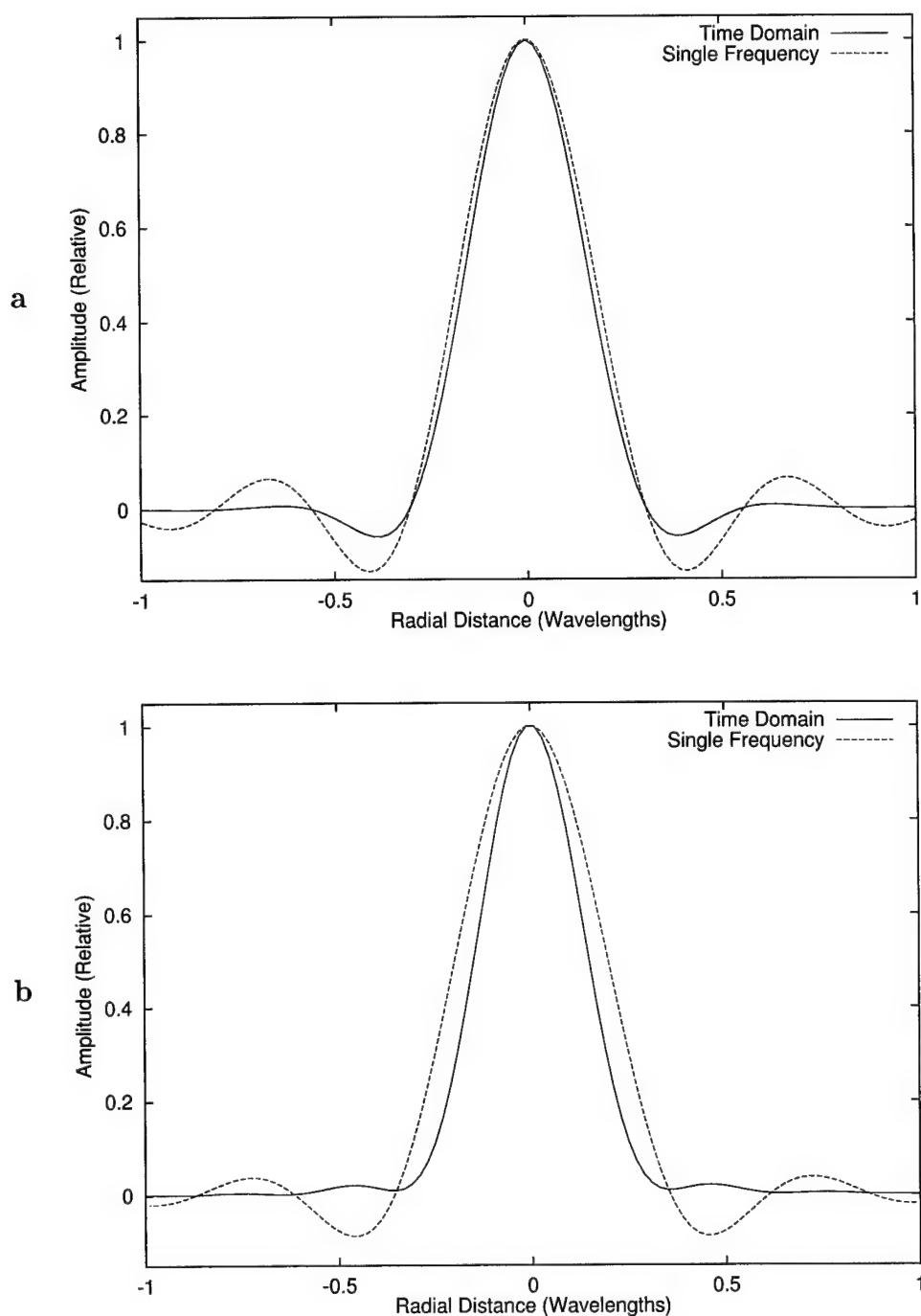
FIG. 2. Point-spread functions for time-domain and single-frequency diffraction tomography methods. In each panel, the vertical scale corresponds to the relative amplitude of the reconstructed contrast $\gamma(\mathbf{r})$, while the horizontal scale corresponds to number of wavelengths at the center frequency. (a) Two-dimensional case. (b) Three-dimensional case.
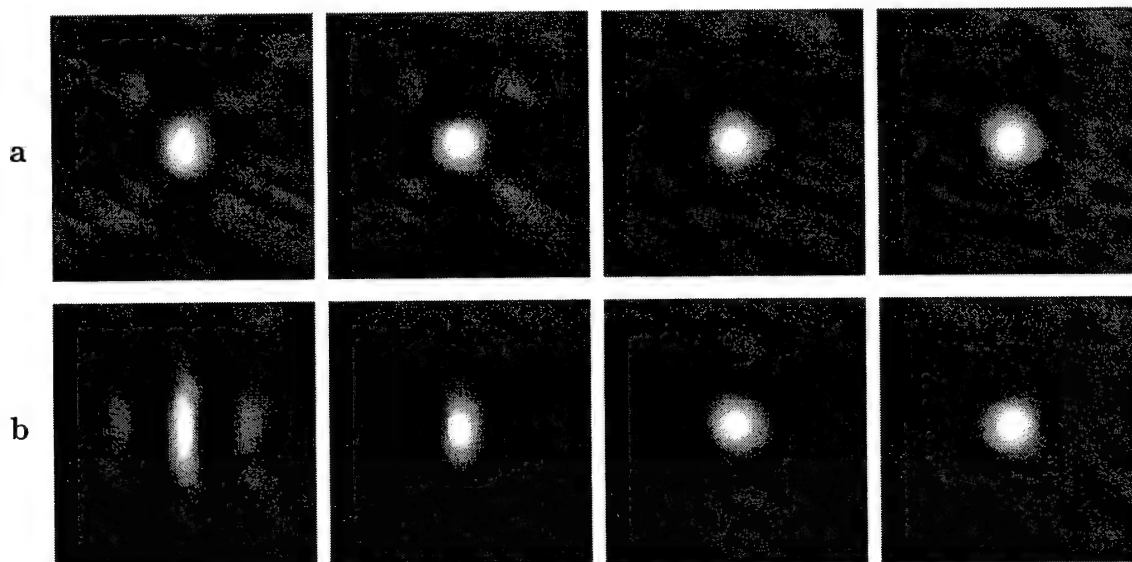
FIG. 3. Effect of aperture characteristics on image quality. The point-spread function (PSF), determined as the real part of the reconstructed contrast $\gamma_M(\mathbf{r})$, is shown for the same waveform parameters as in Fig. 2. Each panel shows an area of 0.6 mm $\times$ 0.6 mm, corresponding to one square wavelength at the center frequency. In each case, 64 measurement directions were employed. (a) PSF for 1, 4, 8, and 16 incident-wave directions. (b) PSF for aperture sizes of $\pi/2$, π, $3\pi/2$, and 2π radians.
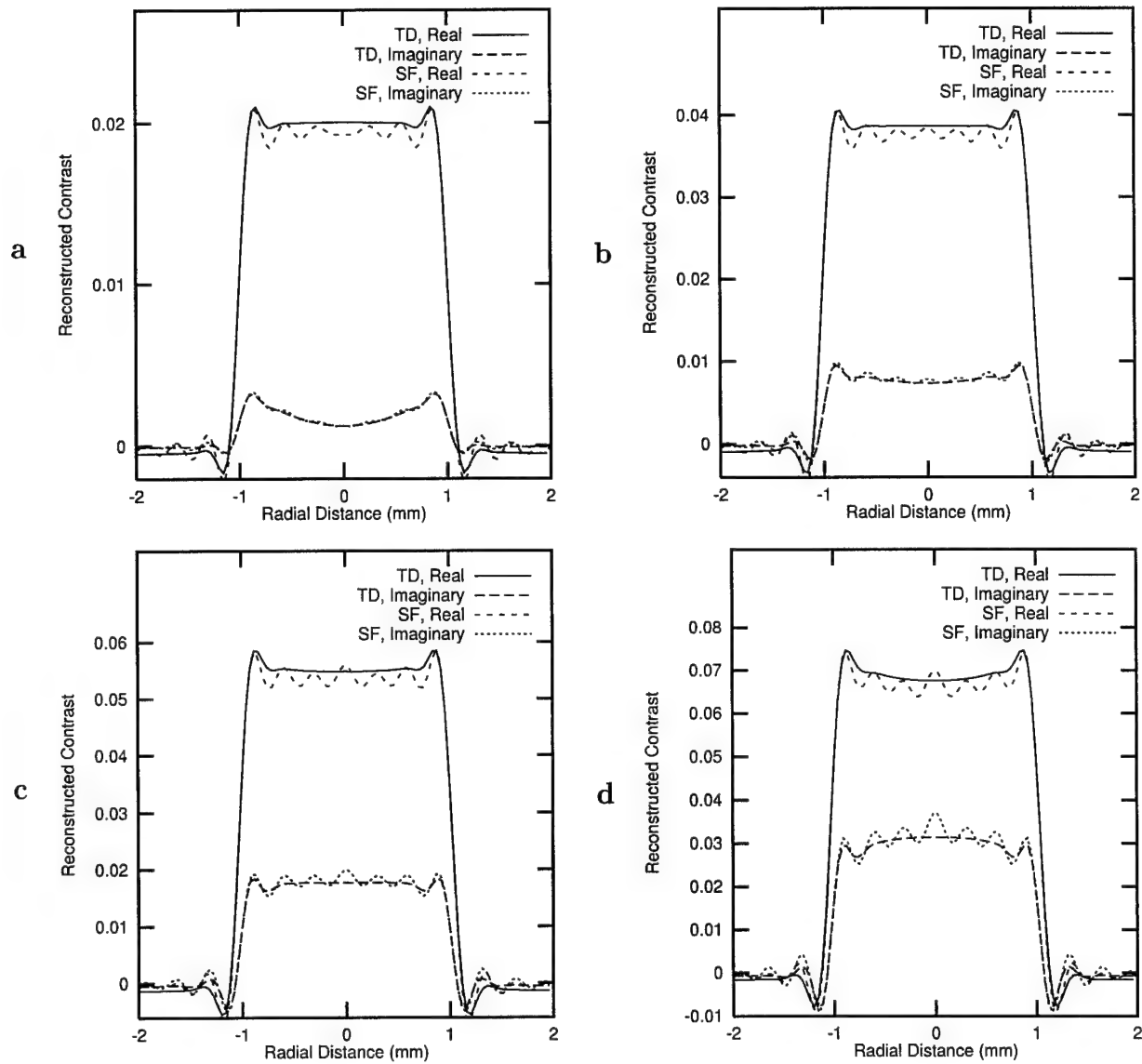
FIG. 4. Cross sections of reconstructed contrast functions $\gamma(\mathbf{r})$ for a cylinder of radius 1 mm, using time-domain (TD) and single-frequency (SF) diffraction tomography. Waveform parameters are as in Fig. 1. (a) $\gamma = 0.02$. (b) $\gamma = 0.04$. (c) $\gamma = 0.06$. (d) $\gamma = 0.08$.
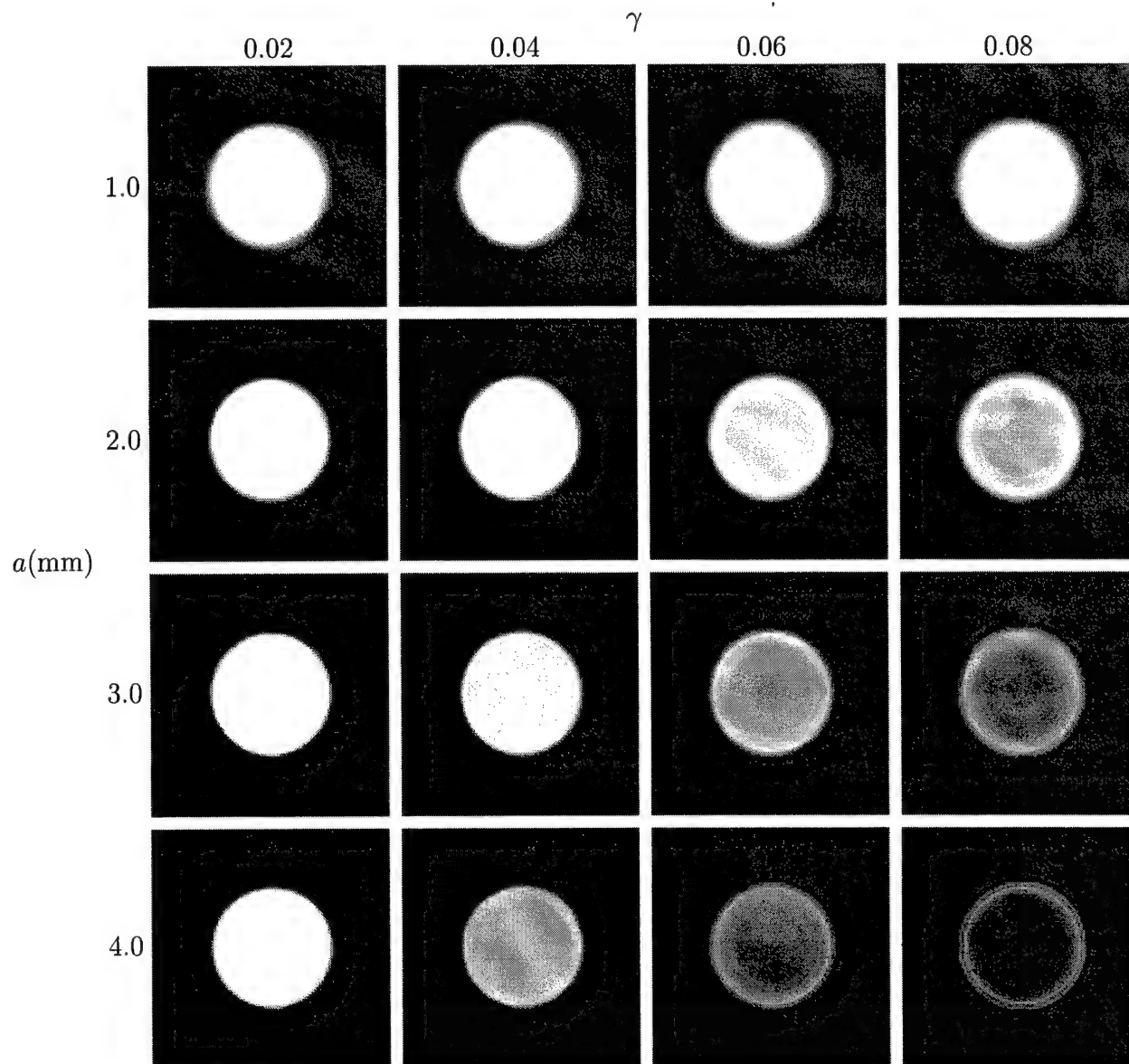
FIG. 5. Time-domain reconstructions for cylinders of varying size and contrast. Each panel shows the real part of the reconstructed contrast $\gamma_M(\mathbf{r})$ for a pulse of center frequency 2.5 MHz and -6 dB bandwidth 1.5 MHz. In each case, the ratio of measurement directions to incident-wave directions is four. All images are shown on a linear, bipolar gray scale where white represents the maximum amplitude of $|\gamma_M(\mathbf{r})|$ and black represents -1 times the maximum amplitude.
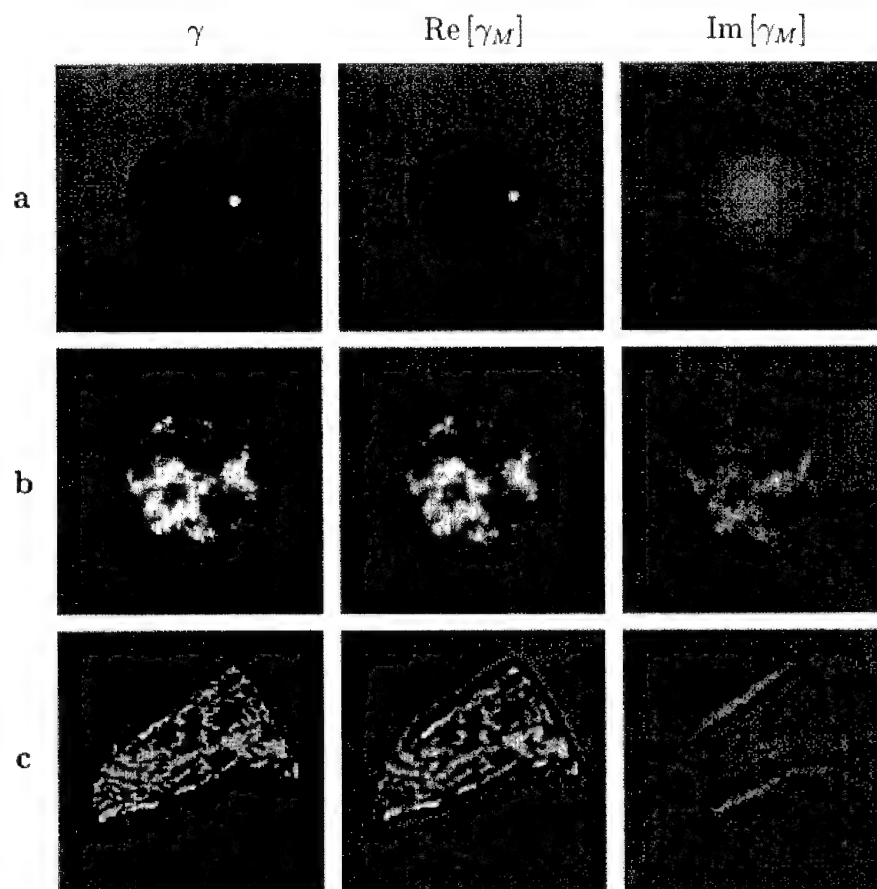
FIG. 6. Time-domain reconstructions from full-wave synthetic data for three arbitrary scattering objects. Each row shows the actual (purely real) contrast function γ together with the real and imaginary parts of the reconstructed contrast function γ_M, using the same linear bipolar gray scale for each panel. Each panel shows a reconstruction area of 5 mm $\times$ 5 mm. (a) Cylinder, radius 2.5 mm, with an internal cylinder of radius 0.2 mm. (b) Cylinder, radius 2.5 mm, with random internal structure. (c) Tissue structure, with variable sound speed and density, from chest wall cross section 5L in Ref. 56.
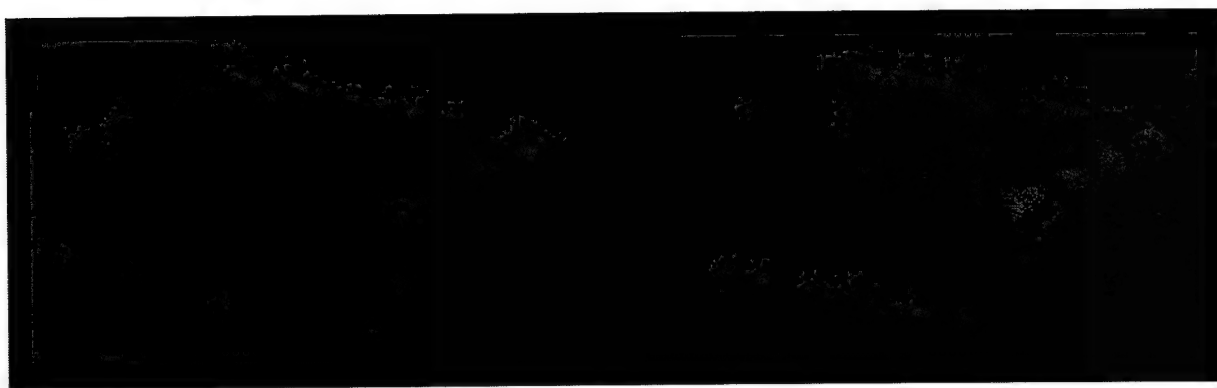
FIG. 7. Three-dimensional reconstructions of a uniform slab with contrast $\gamma = 0.01$. Each reconstruction shows an isosurface rendering of the surface $\gamma_M = 0.0025$. Left: single-frequency reconstruction. Right: time-domain reconstruction.

Appendix B

Simulation of Ultrasonic Pulse Propagation, Distortion,
and Attenuation in the Human Chest Wall

Submitted to *Journal of the Acoustical Society of America*

Simulation of ultrasonic pulse propagation, distortion, and attenuation in the human chest wall

T. Douglas Mast

Applied Research Laboratory, The Pennsylvania State University,

University Park, Pennsylvania 16802

Laura M. Hinkelman

Department of Electrical and Computer Engineering, University of Rochester,

Rochester, New York 14627 *

Leon A. Metlay

Department of Pathology and Laboratory Medicine, University of Rochester Medical School,

Rochester, New York 14642

Michael J. Orr

Department of Electrical and Computer Engineering, University of Rochester,

Rochester, New York 14627

Robert C. Waag

Departments of Electrical and Computer Engineering and Radiology, University of Rochester,

Rochester, New York 14627

April 2, 1999

---

*Present address: Department of Meteorology, The Pennsylvania State University, University Park, Pennsylvania 16802

Abstract

A finite-difference time-domain model for ultrasonic pulse propagation through soft tissue has been extended to incorporate absorption effects as well as longitudinal-wave propagation in cartilage and bone. This extended model has been used to simulate ultrasonic propagation through anatomically detailed representations of chest wall structure. The inhomogeneous chest wall tissue is represented by two-dimensional maps determined by staining chest wall cross sections to distinguish between tissue types, digitally scanning the stained cross sections, and mapping each pixel of the scanned images to fat, muscle, connective tissue, cartilage, or bone. Each pixel of the tissue map is then assigned a sound speed, density, and absorption value determined from published measurements and assumed to be representative of the local tissue type. Computational results for energy level fluctuations and arrival time fluctuations show qualitative agreement with measurements performed on the same specimens, but show significantly less waveform distortion than measurements. Visualization of simulated tissue-ultrasound interactions in the chest wall shows possible mechanisms for image aberration in echocardiography, including effects associated with reflection and diffraction caused by rib structures. Comparison of distortion effects for varying pulse center frequencies shows that, for soft tissue paths through the chest wall, energy level and waveform distortion increase markedly with rising ultrasonic frequency and that arrival-time fluctuations increase to a lesser degree.

43.80.Qf, 43.20.Fn, 43.58.Ta, 43.80.Cs

INTRODUCTION

Echocardiography is widely employed for diagnosis of cardiac disease including valvular defects, pericardial effusion, and wall motion abnormalities.[1-3] Commonly, echocardiography is performed noninvasively through the chest (transthoracic) using an external probe placed on the chest wall. The chest wall, however, can considerably degrade image quality because acoustic paths between the skin and heart can contain ribs and cartilage as well as inhomogeneous muscle and fatty tissue. The result is that as many as 10-30% of patients cannot be successfully imaged with present transthoracic techniques.[4] This limitation of transthoracic echocardiography has led to the development of transesophageal echocardiography, in which the heart is imaged by a transducer inserted within the esophagus.[1-4] Although transesophageal echocardiography provides superior image quality, resulting in high diagnostic sensitivity and specificity, the invasiveness of the procedure is accompanied by increased risk.[3-6] For this reason, improvement in the noninvasive transthoracic approach is desirable, for example, by the development of methods to compensate for image degradation caused by the chest wall.

An understanding of ultrasonic aberration produced by the chest wall is important to the development of appropriate compensation methods for transthoracic ultrasonic imaging. Direct measurements of ultrasonic distortion produced by chest wall specimens[7,8] have been helpful. The study reported in Ref. 7 shows that propagation through the chest wall causes substantial beam distortion. However, that study did not distinguish the effect of soft tissue from effects caused by rib structures. In Ref. 8, a detailed study of distortion caused by soft tissue paths indicates that soft tissue distortion in the chest wall is substantially less than corresponding distortion in the human abdominal wall. However, distortion caused by ribs was only treated qualitatively in the latter study because the physical mechanisms of rib-induced distortion could not be adequately described by the method reported there. Although a model of ultrasound propagation in the chest wall has previously been described,[9] that model is based on coarse depictions of chest wall morphology including homogeneous

tissue layers and evenly-spaced, uniformly-shaped ribs. These previous experiments and simulations, therefore, have left gaps in knowledge about the physical causes of ultrasonic wavefront distortion caused by the chest wall.

Recent work on simulation of ultrasonic pulse propagation[10–12] has provided insight about the wavefront distortion caused by the human abdominal wall. Although these studies have provided specific information about the relationships between soft tissue morphology and ultrasonic wavefront distortion, the work is not fully applicable to distortion caused by the human chest wall. The morphology of chest wall soft tissue has been hypothesized to be different from the abdominal wall in ways that affect ultrasonic wavefront distortion.[8] Furthermore, imaging through the chest wall is complicated by ribs that limit the usable acoustic window size and cause scattering and reflection.

The study reported here applies quantitative simulation methods, similar to those presented in Refs. 10 and 12, to anatomically detailed chest wall models that include the ribs. To accurately model the strong losses associated with propagation through bone and cartilage, the finite-difference method described in Ref. 10 has been extended to include absorption. Quantitative descriptions of the distortion caused by soft tissues are obtained by statistical analysis of simulated distortion. Visualizations of wavefronts propagating through maps of chest cross sections provide evidence about physical relationships between wavefront distortion and the morphology of ribs and soft tissue structures in the chest wall. Further insight about wavefront distortion mechanisms is provided by comparison of distortion results for incident pulses of different center frequencies.

I. THEORY

Ultrasonic pulse propagation through the human chest wall is modeled here using the equations of motion for a fluid of variable sound speed, density, and absorption. The tissue is assumed motionless except for small acoustic perturbations. Absorption is included using an adaptation of the Maxwell solid model, in which all absorption effects are represented by a single relaxation time. This assumption results in frequency-independent absorption characteristics.[13] For such a fluid, the linearized equations of mass conservation, momentum conservation, and state can be combined to obtain the first-order, two-dimensional, coupled propagation equations

$$\frac{\partial p(x,y,t)}{\partial t} + \rho(x,y)\, c(x,y)^2\, \nabla \cdot \mathbf{v}(x,y,t) = -\alpha(x,y)\, p(x,y,t), \tag{1}$$

$$\rho(x,y)\, \frac{\partial \mathbf{v}(x,y,t)}{\partial t} + \nabla p(x,y,t) = 0. \tag{2}$$

Here, $p(x,y,t)$ is the acoustic perturbation in fluid pressure, $\mathbf{v}(x,y,t)$ is the vector acoustic velocity, $\rho(x,y)$ is the ambient density, $c(x,y)$ is the ambient sound speed, and $\alpha(x,y)$ is an absorption coefficient that is equivalent to the inverse of a spatially-dependent relaxation time $\tau(x,y)$.

The absorption coefficient α, defined as a real quantity, is related to the energy lost per unit length as follows. The propagation equations (1) and (2) lead, for plane-wave propagation of the form $p = e^{i(kx - \omega t)}$, to the dispersion relation

$$k = \frac{\omega}{c}\sqrt{1 + \frac{i\alpha}{\omega}}, \tag{3}$$

where k is the complex wavenumber, ω is the (real) radial frequency $2\pi f$, and c is the (real) sound speed. The imaginary part of the wavenumber k is the absorption in nepers per unit length. Thus, the absorption parameter α can be obtained by numerical solution of the equation

$$\mathrm{Im}[k] = \frac{\mathrm{loss\ (dB/length)}}{20\log_{10}(e)} = \mathrm{Im}\left[\frac{\omega}{c}\sqrt{1 + \frac{i\alpha}{\omega}}\right]. \tag{4}$$

Solution of Eq. (4) results in wavenumbers having a real part that differs from ω/c. Since this discrepancy is less than 1% over the range of tissue properties employed in the present study, use of absorption coefficients computed from Eq. (4) does not significantly affect propagation characteristics except by adding the specified absorption.

Equations (1) and (2) were solved numerically using the finite-difference time-domain (FDTD) method described in Refs. 10 and 14. This method is a two-step MacCormack algorithm that is fourth-order accurate in space and second-order accurate in time. Further details on this class of finite difference algorithms can be found in Refs. 15–17.

The initial condition was chosen to model the experimental configuration in Ref. 8, in which a spatially broad, nearly planar wavefront was emitted from a wideband, pulsed, unfocused source far from the tissue layer. The initial wavefront was represented in the present simulation as a plane wave pulse propagating in the $+y$ direction:

$$
p(x, y, 0) = -\sin[k_0(y - y_0)] \, e^{-(y-y_0)^2/(2\sigma^2)},
$$

$$
u(x, y, 0) = 0, \quad \text{and}
$$

$$
v(x, y, 0) = \frac{p(x, y, 0)}{\rho c}, \tag{5}
$$

where the wavenumber k_0 is equal to $2\pi f_0/c$ for a center frequency of f_0 and σ is the Gaussian parameter of the pulse temporal envelope. The spatial Gaussian parameter σ was chosen to simulate the bandwidth of the pulse used in the experiments, as discussed below in the Method.

The computational configuration is analogous to that described in Ref. 10. The domain of computation is two-dimensional, with the y direction taken to be parallel to the direction of propagation and the x direction parallel to the initial wavefront. As in Ref. 10, periodic boundary conditions were applied on the domain edges that were parallel to the direction of propagation, while radiation boundary conditions were applied on the edges perpendicular to the direction of propagation.

II. METHOD

This study employed six chest wall specimens from four different donors between 79 and 85 years of age. One specimen (4L) was from a white female, while the others were from white males. All specimens were obtained from autopsy, stored unfixed at $-20\,°C$, and thawed when needed for study. Wavefront distortion measurements made on some of these specimens as well as other specimens are described in Ref. 8. The nomenclature employed here for the cross sections corresponds to that of Ref. 8 for the whole specimens from which the cross sections were taken; each cross section is identified by a donor number together with "L" or "R" to indicate whether the specimen was taken from the left or right side of the breastplate. Additional numbers were used in Ref. 8 to indicate the intercostal space used in each measurement; here, letters are used to indicate independent acoustic paths. Four of the cross sections employed here (4L, 5L, 7L, and 7R) were taken from specimens employed in Ref. 8. Cross sections 8L and 8R were taken from specimens through which ultrasonic transmission was measured in the study described in Ref. 8, but distortion statistics for these specimens were not reported in Ref. 8 because of limited acoustic windows.

After the wavefront distortion measurements, the specimens were cut into cross sections using the technique described in Ref. 10. The cross sections were fixed and stained with a modified Gomori's trichrome stain according to the procedure detailed in Ref. 18, so that tissue types could be distinguished. This stain colored muscle tissue red and connective tissue blue while leaving the fat its natural color. Calcified tissue, including bone and cartilage in the current specimens, was not differentially stained by this technique, but the natural contrast between bone, cartilage, and marrow was sufficient to allow tissue mapping. Full-color 300 d.p.i. images of the cross sections were created by placing each stained tissue cross section directly onto the surface of a flatbed digital scanner. Image editing packages[19] were used to manually segment the cross sectional images, *i.e.*, to map the images into regions that corresponded to one of six media. The media were water (representing water external to specimens or blood inside blood vessels), fat (including subcutaneous fat, fat interlaced

7

within muscle layers, and marrow), muscle, connective tissue (including skin, septa, and fasciae), cartilage, and bone (including cortical bone and trabeculae within cancellous bone).

The six segmented tissue maps are shown in Fig. 1. All of the cross sections contain a layer of septated subcutaneous fat below the skin. Most of the cross sections also include a layer composed primarily of the major pectoral muscles and their connective fasciae above the ribs. Between the ribs are regions of muscle (internal intercostal and external intercostal groups) interlaced with fat. In some cases, additional thin layers of fat between muscle layers are apparent. Cross sections 4L and 7R are cut along the intercostal spaces parallel to the ribs, so that in each a wide cross section of soft tissue appears. Cross sections 5L, 7L, and 8L are cut perpendicular to the ribs, so that each contains soft-tissue acoustic paths with width equal to the width of the corresponding intercostal spaces. Cross section 8R is cut perpendicular to the sternum at a location of large curvature in the ribs, so that the ribs are diagonally sectioned. Several blood vessels appear in cross sections 4L, 7L, 7R, and 7R; the largest of these is the internal mammary artery.

The basic structure of the cross sections is consistent with standard descriptions of chest wall anatomy.[20,21] Ribs appear in each cross section; each rib is composed of a "costal cartilage" near the sternum (shown in most of the cross sections considered here) attached to a "true rib" (composed primarily of cancellous bone) at the edge farther from the sternum. In the cross sections considered here, the costal cartilages are primarily composed of calcified cartilage, surrounded by a thin layer of cortical bone (solid, dense bone with microscopic porous structure), which in turn is surrounded by the periosteum, a thin membrane of connective tissue. Cross sections 7L and 7R also appear to contain a small amount of cortical bone in the central portion of the ribs. This phenomenon may be associated with advanced calcification known to occur in aging humans.[22] Cancellous bone, composed of thin trabeculae that forms macroscopic cells filled with marrow, is seen in all the ribs of cross section 5L, which was taken at a distance farther from the sternum so that the true ribs, rather than the costal cartilages, were included in this cross section. Some cancellous bone is also apparent within portions of the ribs of cross sections 4L and 8R. In each case,

8

the cancellous bone is surrounded by a thin layer of cortical bone and by the periosteum. A portion of the sternum, composed of cancellous bone surrounded by cortical bone, is visible at the left side of cross section 4L.

The density and sound speed arrays needed for the finite-difference computation were created by mapping regions of the segmented tissue images to reference density and sound speed values for the five tissue types and water. The water sound speed and density employed are those of pure water at body temperature (37.0 °C).[23,24] Sound speeds for muscle and fat were obtained by averaging values for human tissues given in Refs. 25 and 26. A representative sound speed for connective tissue was determined using an empirical formula relating collagen content to ultrasonic sound speed[27] together with a measured value for the collagen content of human skin.[28] The sound speed employed for bone was obtained from an average of values reported in Ref. 29 for longitudinal-wave propagation in human cortical bone. The sound speed used here for cartilage is that given in Ref. 30 as quoted in Ref. 25. Density values for soft tissues were determined from Ref. 31 by averaging values reported for adipose tissue, skeletal muscle, and skin, respectively. Density values employed for bone and cartilage are average values from Ref. 29.

Attenuation values were determined from measurements summarized in Ref. 25 for human fat at 37°C, human bicep muscle at 37° C, human skin at 40° C, human and bovine cartilage at 23° C, and human skull (temperature not reported). Attenuation values reported at other ultrasonic frequencies were interpolated (or, for the skull data, extrapolated) to obtain values for 2.3 MHz (corresponding to the pulse center frequency employed here and in Ref. 8) assuming a linear dependence of attenuation on frequency. The attenuation for water was estimated by extrapolating frequency- and temperature-dependent attenuation values summarized in Ref. 32 to 2.3 MHz and 37.0° C. The values of tissue parameters employed in the present study are given in Table I.

The finite-difference program was employed to compute propagation of a plane wave pulse through each scanned cross section from the skin to the peritoneal membrane, mimicking the propagation path employed in the distortion measurements of Ref. 8. The spatial step

9

size of the finite-difference grid was chosen to be 0.0442 mm, or 1/15 wavelength in water at the center frequency of 2.3 MHz. The temporal step size was chosen to be 0.00725 μs, for an optimal Courant-Friedrichs-Levy number $c\Delta t/\Delta x$ of 0.25.[17] The Gaussian parameter σ of the source pulse was chosen to be 0.4766 mm in accordance with the experimentally measured pulse bandwidth (for pulses transmitted through a water path) of 1.2 MHz. Visual comparison confirmed that the simulated pulse closely matched the measured pulses in shape and length.

Each simulation was performed on a workstation with 128 MB of random-access memory. Finite-difference grids on the order of 1500×1000 points were employed. At each time step, the wave field was updated on a grid subset chosen to include the entire support of the acoustic wave but to exclude quiescent regions. The entire pressure field was saved as a raster image at intervals of 0.725 μs for later visualization. The computation time for each simulation was on the order of five hours.[33]

Signals were recorded for 8.62 μs at a sampling frequency of 138 MHz by simulated apertures with dimensions close to those in the experimental study of Ref. 8. Positions of all simulated apertures employed are sketched in Fig. 1. The simulation of receiving elements was performed by integrating the locally-computed pressure over the element pitch of 0.21 mm. For cross sections cut parallel to the ribs, the simulated apertures contained 68 elements for an aperture width of 14.28 mm. For cross sections cut perpendicular to the ribs, 55 simulated elements were used to form 11.55 mm apertures. Element directivity effects were implicitly included by the integration of omnidirectional sensitivity functions over the width of each element.

A one-dimensional version of the reference waveform method[10,34] was used to calculate the arrival time of the pulse at each receiving position in the simulation data. The arrival time fluctuations across the receiving aperture caused by each cross section were calculated by subtracting a linear fit from these calculated arrival times. Energy level fluctuations in the data were calculated by summing the squared amplitudes of each waveform over a 2.4 μs window that isolated the main pulse, converting to decibel units, and subtracting

10

the best linear fit from the resulting values. As for polynomial fits previously employed in wavefront distortion measurements,[8] the purpose of the linear fit removal in each case was to compensate for gross changes in tissue thickness across the array. Variations in pulse shape across the aperture were evaluated using the waveform similarity factor;[34] this quantity, which can be considered a generalized cross-correlation coefficient, has a maximum of unity when all received waveforms are identically shaped.

To test the frequency dependence of chest wall wavefront distortion, propagation through eight portions of specimens, each containing only soft tissue, was also computed for wavefronts having center frequencies of 1.6 and 3.0 MHz. In each case, the initial wavefront was chosen to have the same temporal envelope as above. The absorption coefficient at these frequencies for each tissue type was extrapolated from the value employed at 2.3 MHz using the assumption that absorption depended linearly on the center frequency. The spatial and temporal sampling rates were also varied in inverse proportion to the pulse center frequency. All runs were otherwise identical in configuration and processing to those described above.

III. RESULTS

Wavefront distortion results for 13 soft tissue paths (*i.e.*, paths in which wavefront distortion was not significantly influenced by the ribs) are shown in Table II. These results indicate that soft tissue paths cause a wide range of wavefront distortion effects depending on the specific morphology of each path. For instance, path 7R-c causes arrival time and energy level fluctuations that are more than twice the magnitude of those caused by the adjacent path 7R-d. This difference is thought to arise from morphological features, including muscle tissue with interlaced fat and a large amount of connective tissue, of the tissue within path 7R-c. Also notable is that the specimen thickness does not closely correspond to variations in distortion. The largest rms arrival time fluctuation and lowest waveform similarity factor, for example, are caused by path 4L-c, which has an average thickness less than the mean for all the tissue paths.

Wavefront distortion statistics for the 13 soft tissue paths are graphically summarized in Fig. 2 together with corresponding statistics for all of the soft tissue measurements reported in Ref. 8. This comparison indicates that wavefront distortion caused by soft tissues in the chest wall simulations is comparable to measured distortion. Arrival time fluctuations and energy level fluctuations for simulated distortion are slightly less than measured values, but mean values of both fluctuations for the simulations fall well within one standard deviation of the corresponding mean fluctuation for the measurements. The waveform similarity factor, however, is substantially higher for simulations than measurements, indicating that simulated waveforms were distorted considerably less than measured waveforms. Correlation lengths for the simulated distortions are somewhat less than measured values. However, consistent with measurements, the mean correlation length of the simulated arrival time fluctuations is greater than that for the simulated energy level fluctuations.

As in Ref. 8, rib structures were found to cause much more distortion than soft tissue alone. The varied nature of distortion caused by rib effects is illustrated in Fig. 3, which shows three representative sets of measured signals for specimen 8L. These measurements

12

were obtained by the methods reported in Ref. 8. The first panel shows 96 adjacent measured signals, along the array direction (approximately parallel to the ribs) for propagation through a tissue path within an intercostal space. The signals are not severely distorted; secondary arrivals are discernible, but are of lower amplitude than the main arrival. The second panel shows 96 measured signals for an elevation over a rib. Here, all signals are severely distorted. Multiple arrivals, as well as high-amplitude spatially-random fluctuations, are seen. The third panel shows 50 measured signals along the elevation direction (perpendicular to the ribs), centered over the soft tissue between the ribs. Here, the main wavefront is curved rather than straight, an additional arrival behind the main wavefront is seen, and portions of the signals from over the ribs (at both edges of the panel) are advanced relative to the signals from the central soft tissue region.

The present simulations allow more detailed qualitative and quantitative investigation of rib effects than were possible from the previous measurements. Propagation through two rib-influenced paths is illustrated in Figs. 4 and 5 by images shown in formats similar to visualizations of propagation through soft tissue in Ref. 10. Simulated ultrasonic pulses are superimposed on portions of the tissue maps from Fig. 1.

Figure 4 shows propagation through a thin rib, composed chiefly of cancellous bone, in cross section 5L (corresponding approximately to path 5L-b). A strong reflection occurs at the first interface between bone and soft tissue, removing a substantial amount of energy from the main wavefront. The small, high-contrast trabeculae within the rib cause considerable scattering, as can be observed in panel (b) of Fig. 4. The scattering causes random fluctuations behind the main wavefront; these fluctuations somewhat resemble those seen in the measured data of Fig. 3(b). After passing through the rib, as seen in panels (c) and (d) of Fig. 4, the central portion of the wavefront shows substantial attenuation and distortion. However, the average arrival time of the wavefront is not greatly changed by propagation through the rib, but is advanced by only about one-half period. This phenomenon apparently occurs because the influence of the "slow" marrow (modeled here as fat) counteracts the influence of the "fast" trabeculae. Noteworthy is that the predominant ultrasonic wave-

length has increased after propagation through the rib, so that the effective center frequency of the wavefront has been lowered. Since the absorption model used in the present study includes only frequency-independent absorption, the loss of short-wavelength components in this simulation results only from frequency-dependent scattering caused by the trabeculae.

Propagation within path 8L-b, which includes two larger ribs and the corresponding intercostal space, is illustrated in Figure 5. At the position of the cross section, these ribs are composed primarily of cartilage and surrounded by a thin layer of cortical bone. Since the cartilage and bone of these ribs is modeled as homogeneous, small-scale scattering within these tissues did not occur in this simulation. Instead, the wavefront is reflected from interfaces between cartilage, bone, and soft tissue.

The visualization shown in Fig. 5 provides physical reasons for all the rib-related distortion phenomena seen in the measured data of Fig. 3(c). The wavefronts propagating through the ribs show greater attenuation than that in Fig. 4, both because of the high absorption of the ribs and because of the reflections noted above. These wavefronts are also advanced relative to the wavefront propagating through the intercostal space, because of the higher sound speed of both bone and cartilage. The wavefront propagating through the intercostal space is distorted somewhat by the inhomogeneous soft tissue path, as can be observed in panels (b) and (c). However, much greater distortion results from interaction between the wavefront and the ribs. A rightward-propagating reflection, seen in panels (b) and (c), combines with the main wavefront in panel (d) to result in severe distortion at the right side of the central wavefront. Furthermore, diffraction from the edges of the ribs results in large curvature of the soft-tissue wavefront.

Distortion and attenuation statistics for a variety of rib-influenced paths are shown in Table III. Footnotes in Table III indicate physical causes of distortion present within each path. A variety of distortion and attenuation mechanisms are illustrated. Propagation through small intercostal spaces (paths 4L-a, 8L-b, 8L-f, and 7R-a) causes diffraction effects that introduce substantial curvature into the wavefront, as seen in Fig. 5. This large-scale wavefront curvature is associated with large arrival time fluctuation values although the

14

wavefronts generally appear to be locally smooth. Interference between directly-transmitted and rib-reflected wavefronts (paths 4L-a, 8L-b, 8L-d, 8L-f, and 7R-a) introduces arrival time, energy level, and waveform distortion substantially greater than that for soft tissue paths without ribs. Propagation through cancellous bone (paths 4L-a, 4L-b, 5L-b, and 8R-c) results in considerable attenuation and large waveform distortion, while propagation through cortical bone and cartilage (paths 4L-a, 4L-b, 8L-a, 8L-c, 8L-e, 8L-g, 7L-c, 7R-a, 7R-b, and 8R-c) results in even larger attenuation but smaller distortion. Where bone is embedded within cartilage (paths 7-Lc and 7R-b), additional scattering also occurs. For the path including a large bone inclusion (paths 7R-b), this scattering results in extremely high energy level and waveform distortion.

Frequency-dependent wavefront distortion statistics are summarized in Fig. 6. Tissue paths used for these computations, none of which include rib structures, are those labeled 4L-d, 4L-f, 5L-a, 5L-c, 8R-a, 8R-b, 7L-a, and 7L-b in Fig. 1. The results shown in Fig. 6 indicate that arrival time fluctuations, energy level fluctuations, and waveform distortion all become more severe with increasing pulse frequency. The most dramatic change is in the energy level distortion; on average, the rms energy level fluctuations for the 3.0 MHz signals are 2.3 times those for the 1.6 MHz signals. Correlation lengths of both arrival time and energy level fluctuations decrease with frequency, so that the predominant length scales of ultrasonic wavefront distortion are seen to decrease with the ultrasonic wavelength. As with the rms distortion statistics, the most dramatic frequency-dependent change is in the energy level fluctuations. Still, even the high-frequency pulses here show substantially smaller distortion than that previously observed in experiments and simulations for the human abdominal wall.[10-12,35]

IV. DISCUSSION

As with earlier simulations of propagation through tissue,[10,12] the current study shows qualitative agreement with measured wavefront distortion results for similar specimens.[8] However, the accuracy of the present model is limited by simplifications of true tissue structure. In particular, the computational model here does not account for property variations within tissue types, tissue microstructure, or three-dimensional tissue structure. These limitations are discussed, with respect to soft tissues, in Ref. 10.

The modeling of ribs adds additional complication. In the current study, individual trabeculae were assumed to be composed of tissue having properties identical to cortical bone, an assumption known as Wolff's hypothesis.[36] The validity of this hypothesis has been questioned;[37,38] however, measured elastic properties of individual trabeculae vary widely[37,38] and recent work[39] has provided support for Wolff's hypothesis. Thus, the properties employed here for trabecular bone can be regarded as a reasonable order-of-magnitude estimate. Likewise, the modeling of marrow as fat tissue is a simplifying assumption that may have limited validity, although available data suggest that the density and sound speed of marrow are close to those for other adipose tissues.[29] In addition, the present model for cartilage is based on measurements of normal cartilage, while the cartilage present in the specimens employed here was calcified due to the age of the donors. However, density measurements made on eight representative samples of calcified cartilage (two from specimen 7R, four from specimen 1R,[8] and two from an unused specimen) resulted in an average density of 0.00111 kg/m^3, which is different by only 1% from the density assumed here. Since sound speed in calcified tissue has been empirically shown to be directly related to density,[40,41] this small change in density suggests that the acoustic properties of the calcified cartilage in our specimens is close to that for normal cartilage.

The computations reported here model the chest wall as a fluid of variable sound speed, density, and compressibility. This model implicitly neglects shear wave propagation. The neglect of shear waves in soft tissues is believed to be justified because absorption of shear

waves in soft tissues is much greater than absorption of longitudinal waves.[42,43] In calcified tissues, however, significant shear waves are known to be generated.[44,45] In the current scattering configuration, some shear waves are likely generated wherever the rib surface is far from parallel to the wavefront. However, since shear wave absorption has been found to be somewhat larger than longitudinal wave absorption for ultrasonic propagation in bone,[44] the significance of shear-wave propagation within bone on transmitted ultrasonic wavefronts is questionable. For this reason, omission of nonlongitudinal waves in the present study, as in another computational study of ultrasonic scattering from bone,[46] is believed to be justified; however, further study would be required to confirm this assumption.

The absence of frequency-dependent absorption is a possible source of error in the present estimates of total tissue attenuation, energy level fluctuations, and waveform distortion. However, since absorption in tissue increases approximately linearly with frequency, lower absorption for frequency components below the pulse center frequency would nearly cancel higher absorption for frequency components above the center frequency, so that the average absorption incurred by a wideband pulse should still be computed with fair accuracy. For this reason, the absence of frequency-dependent absorption in the calculations reported here is not considered to be a significant source of error in the computed attenuation or energy level fluctuation curves. Still, inclusion of frequency-dependent absorption would result in additional waveform distortion effects. The lack of this effect is a likely reason for the lower waveform distortion (higher waveform similarity factors) obtained from simulations as compared to measurements. However, the absence of frequency-dependent absorption effects allowed frequency-dependent scattering effects to be clearly quantified separately from absorption effects.

Although the simulations were planned to match the measurements of Ref. 8 closely, a number of differences remain. The most important of these, as discussed in Ref. 10, is that the simulations were performed using a two-dimensional tissue model while the measurements were inherently three-dimensional. Other differences include details of the source waveform and wavefront shape, variations in the specimen orientations and the regions in-

terrogated, and variations in the distance between the specimen and the real or simulated receiving aperture. All of these differences could contribute to discrepancies between measurements and simulations.

In general, most of the simplifying assumptions in the present tissue model are likely to result in underestimation of wavefront distortion produced by the human chest wall. Incorporation of tissue microstructure, spatially-dependent acoustic properties for each tissue type, shear wave propagation in bone and cartilage, three-dimensional propagation, and frequency-dependent absorption could all result in greater spatial and temporal variations in the propagating acoustic fields, so that these features could produce simulated distortion with characteristics closer to measurements. For this reason, distortion statistics computed using the present tissue model should be interpreted as lower limits for the statistics of distortion occurring in real chest wall tissue.

Additionally, some of the discrepancy between simulated and measured distortion may be explained by the nonuniform characteristics of the receiving transducer employed in the measurements.[8] The water-path measurements reported in Ref. 8 show arrival time fluctuations (mean 2.21 ns) and energy level fluctuations (mean 0.36 dB); although small, these fluctuations are comparable to the difference between the average measured and simulated fluctuations. Thus, compensation for arrival time and energy level fluctuations due to transducer irregularities could reduce measured distortion to levels closer to the simulations. Also, the waveform similarity factor for water path measurements was 0.991,[8] which indicates greater waveform distortion than the average value of 0.995 computed here for soft tissue paths. Thus, compensation of the measured data for transducer impulse-response variations could raise the measured waveform similarity factor to a value in closer agreement with simulations.

Previous experimental measurements of wavefront distortion caused by the human chest wall[8] have suggested that distortion caused by chest wall soft tissues is less severe than that caused by the human abdominal wall.[11,35] This difference has been observed to occur even though average specimen thicknesses were comparable in chest wall[8] and abdominal wall[11,35]

measurements. The present study provides support for these results; arrival time and energy level distortion by the chest wall was found here to be smaller than that produced by the abdominal wall in previous simulation studies.[10,12] For the simulations, this difference may be partially explained by the fact that the chest wall specimens employed here are thinner on average (mean thickness 17.5 mm) than the abdominal wall cross sections employed in Refs. 10 and Ref. 12 (mean thickness 26.7 mm). Another possible partial explanation is that the pulse center frequency employed in abdominal wall measurements and simulations was 3.75 MHz, significantly higher than the center frequency of 2.3 MHz for the chest wall measurements and simulations. Differences in pulse frequency and specimen thickness may explain the discrepancy in energy level distortion between the abdominal wall and chest wall, but do not fully explain the discrepancy in arrival time distortion results. For instance, the mean arrival time and energy level fluctuations per unit length are 1.02 ns/mm and 0.083 dB/mm for the present study vs. 1.96 ns/mm and 0.105 dB/mm for the abdominal wall cross sections of Ref. 10 and 12. Arrival time distortion was shown here to increase only subtly with increasing pulse frequency, so that this discrepancy in arrival time fluctuations is not fully explained by pulse frequency differences. However, energy level fluctuations increase markedly with frequency for chest wall tissue. Thus, for equal ultrasonic pulse frequencies, chest wall tissue should cause energy level distortion per unit length comparable to that caused by abdominal wall tissue.

It was suggested in Ref. 8 that chest wall morphology may differ from abdominal morphology in a manner that results in smaller ultrasonic wavefront distortion. The cross sections employed here can be compared with those employed in Ref. 10 and Ref. 12 to evaluate the importance of morphological differences between chest wall and abdominal wall tissue. One difference between the two groups of cross sections is the nature of the subcutaneous fat layers. The abdominal wall cross sections generally contain thicker fat layers, containing many more lobular structures than the chest wall cross sections. Since the high contrast between septa and fat causes substantial ultrasonic scattering,[10-12] this morphological difference is likely to result in lower overall energy level and waveform distortion for chest

wall tissue (although, as discussed above, the energy level distortion per unit propagation length should be comparable). Also, the abdominal wall and chest wall cross sections have markedly different structure within the muscle layers that occur below the subcutaneous fat. The abdominal wall cross sections have many large-scale features due to aponeuroses (interfaces between muscle groups, composed of connective tissue and fat) and large fatty regions. These large-scale features cause large wavefront fluctuations that are associated with large rms arrival time fluctuations.[10,12] In contrast, muscle layers of the chest wall cross sections considered here contain primarily smaller-scale structure associated with small islands of interlaced fatty tissue. This morphological difference may result in lower large-scale arrival time fluctuations but significant energy level fluctuations associated with scattering, consistent with the differences between distortion caused by soft tissues in the abdominal wall and the chest wall.

The present results for frequency dependence of distortion provide further insight into the importance of scattering effects relative to large-scale structure in wavefront distortion caused by soft tissues. If wavefront distortion in the chest wall were caused only by large-scale tissue structures, wavefront distortion to be roughly independent of frequency, since propagation effects are independent of frequency in the geometric acoustics limit. However, distortion caused by scattering effects should increase with the pulse frequency for inhomogeneities of size comparable to the wavelength. Previous simulation and experimental studies[10-12] on distortion caused by the human abdominal wall have suggested that energy level fluctuations and waveform distortion are generally associated with scattering effects, while arrival time fluctuations are predominantly caused by large-scale path length differences. The present results, while consistent with those conclusions, indicate that scattering plays a role in all types of distortion considered here. Since energy level fluctuations and waveform similarity factors exhibit more dramatic increases in distortion with increasing pulse frequency, the present results suggest that scattering is of primary importance in causing energy level and waveform distortion and of secondary importance in causing arrival time distortion.

These results can be employed to evaluate the potential of various approaches to improve echocardiographic imaging. Available acoustic windows for transthoracic imaging are severely limited by the presence of the ribs, so that image quality cannot be significantly improved by increase of aperture size. The present results also indicate that use of higher-frequency probes may provide less benefit than expected because of frequency-dependent scattering in the chest wall.

For these reasons, aberration correction methods are potentially important in transthoracic echocardiography, particularly for higher-frequency imaging. The frequency-dependent distortion results reported here suggest that distortion models employing single phase screens may be of some benefit for aberration correction in echocardiography through soft tissue paths. The relatively weak dependence of arrival time fluctuations on pulse frequency suggests that a large portion of arrival time variations are caused by tissue structures too large to cause significant frequency-dependent scattering effects. Similar conclusions regarding the importance of large-scale structure to arrival time fluctuations have also been drawn from results presented in Refs. 10 and 12.

Still, the present results, like those from earlier studies,[10–12] suggest that single phase screens will not provide complete correction for distortion caused by soft tissues. In particular, methods employing single phase screens will not completely remove distortion caused by scattering. The sharp increase of amplitude and waveform distortion with frequency, as well as the moderate increase of arrival time distortion with frequency, indicate that scattering effects become much more important to ultrasonic aberration as imaging frequencies increase. Furthermore, phase screen models do not inherently account for distortion caused by rib structures, shown here to produce diffraction, reflection, and scattering. Thus, any attempted correction using only phase screen models is likely to provide little improvement in the presence of strong rib-induced effects.

Other correction models that incorporate rib structures may provide greater image improvements for the distortions most important to echocardiography. Processing wavefronts with techniques such as angular spectrum filtering can remove some spurious arrivals,[47] al-

though such computations may be difficult to incorporate into a general correction algorithm. Other possible methods include those incorporating models of tissue structure. Models incorporating ray acoustics[9] may provide improvement, but implicitly neglect diffraction and scattering effects, so that aberration correction would be incomplete, particularly for small intercostal spaces. A more complete aberration correction method could employ synthetic focusing using full-wave numerical computation of acoustic fields within sufficiently accurate models of tissue structure. This method has been implemented, within the context of a quantitative frequency-domain inverse scattering method, in Ref. 48. However, the results presented here indicate that distortion caused by soft tissue and rib structures varies widely based on morphological variations between (and within) individuals. Thus, for any general correction method employing models of tissue structure, separate models of tissue structure must be constructed for each region of interest.

V. CONCLUSIONS

A computational study of ultrasonic propagation through the chest wall, including tissue-dependent absorption as well as detailed anatomical cross sections, has been presented. For soft-tissue paths, computational results for arrival time distortion, energy level distortion, and correlation lengths of these distortions are comparable to those reported in previous chest wall measurements. Both simulations and measurements indicate that arrival time distortion and energy level distortion caused by soft tissues in the human chest wall is smaller than that caused by the human abdominal wall. Differences in morphology between the abdominal wall and the chest wall provide a probable explanation for this difference.

Distortion caused by rib structures is much more severe than that caused by soft tissues. Reflections and diffraction from rib structures complicate wavefronts that travel through soft tissue paths adjacent to ribs and can cause arrival time and energy level fluctuations much greater than those induced by soft tissue structures. Wavefronts propagating directly through rib structures are attenuated by both internal absorption and reflection at interfaces between bone, cartilage, and soft tissue. Internal scattering within rib structures causes distortion phenomena that include severe waveform and energy level distortion, additional attenuation, and lowering of the effective frequency for the transmitted pulse. The strong dependence of distortion on the morphological details of rib structures presents a major challenge for aberration correction in echocardiography.

Simulation of propagation through soft-tissue paths using three different pulse frequencies has indicated that the distortion types investigated here have different frequency dependence. Arrival time fluctuations increase subtly with frequency, while energy level and waveform distortion increase greatly. Thus, a substantial portion of arrival time fluctuations in the chest wall may be explained by large-scale tissue variations, but some arrival time distortion and most energy level and waveform distortion apparently result from scattering. Thus, correction of wavefront distortion caused by soft tissues should become both more important and more challenging as pulse frequencies employed in imaging systems are increased.

ACKNOWLEDGMENTS

REFERENCES

[1] H. Feigenbaum, *Echocardiography* (Lea and Febiger, Philadelphia, 1994).

[2] A. E. Weyman, *Principles and Practice of Echocardiography*, Fifth Edition (Lea and Febiger, Philadelphia, 1994).

[3] J. T. T. Chen, *Essentials of Cardiac Imaging*, Second Edition (Lippincott-Raven, Philadelphia, 1997).

[4] F. M. Clements and N. P. de Bruijn, *Transesophageal Echocardiography* (Little, Brown, and Company, Boston, 1991).

[5] K.-L. Chan, G. I. Cohen, R. A. Sochowski, and M. G. Baird, "Complications of transesophageal echocardiography in ambulatory adult patients: analysis of 1500 consecutive examinations," J. Am. Soc. Echocardiogr. **4**, 577–582 (1991).

[6] W. G. Daniel *et al.*, "Safety of transesophageal echocardiography: a multicenter survey of 10,419 examinations," Circulation **83**, 817–821 (1991).

[7] A. D. Savakur, K. K. Shung, and N. B. Miller, "Distortions of ultrasonic field introduced by the rib cage in echocardiography," J. Clin. Ultrasound **10**, 413–419 (1982).

[8] L. M. Hinkelman, T. L. Szabo, and R. C. Waag, "Measurements of ultrasonic pulse distortion produced by the human chest wall," J. Acoust. Soc. Am. **101**, 2365–2373 (1997).

[9] Y. Y. Botros, E. S. Ebbini, and J. L. Volakis, "Two-step hybrid virtual array-ray (VAR) technique for focusing through the rib cage," IEEE Trans. Ultrason. Ferroelec. Freq. Contr. **45**, 989–999 (1998).

[10] T. D. Mast, L. M. Hinkelman, M. J. Orr, V. W. Sparrow, and R. C. Waag, "Simulation of ultrasonic pulse propagation through the abdominal wall," J. Acoust. Soc. Am. **102**, 1177–1190 (1997).

[11] L. M. Hinkelman, T. D. Mast, L. A. Metlay, and R. C. Waag, "The effect of abdominal wall morphology on ultrasonic pulse distortion. Part I: Measurements," J. Acoust. Soc. Am. **104**, 3635–3649 (1998).

[12] T. D. Mast, L. M. Hinkelman, M. J. Orr, and R. C. Waag, "The effect of abdominal wall morphology on ultrasonic pulse distortion. Part II: Simulations," J. Acoust. Soc. Am. **104**, 3651–3664(1998).

[13] H. Kolsky, *Stress Waves in Solids* (Clarendon Press, Oxford, UK, 1953), pp. 99–129.

[14] V. W. Sparrow and R. Raspet, "A numerical method for general finite amplitude wave propagation and its application to spark pulses," J. Acoust. Soc. Am. **90**, 2683–2691 (1991).

[15] R. W. MacCormack, *Lecture Notes in Physics* (Springer-Verlag, Berlin, 1971), Vol. 8, p. 151.

[16] D. Gottlieb and A. Turkel, "Dissipative two-four methods for time-dependent problems," Math. Comp. **30**, 703–723 (1976).

[17] E. Turkel, "On the practical use of high-order methods for hyperbolic systems," J. Comp. Phys. **35**, 319–340 (1980).

[18] L. M. Hinkelman, L. A. Metlay, C. J. Churukian, and R. C. Waag, "Modified Gomori trichrome stain for macroscopic tissue slices," J. Histotech. **19**, 321–323 (1996).

[19] Images were processed using Adobe Photoshop, Version 3.0, and the Gnu Image Manipulation Program, Version 1.0.

[20] H. Gray, *Gray's Anatomy*, T. P. Pick and R. Howden, Eds., (New York: Gramercy, 1977), pp. 358–364 (facsimile of 1901 American edition of *Anatomy, Descriptive and Surgical*).

[21] R. Warwick and P. L. Williams, Eds. *Gray's Anatomy*, 35th Ed. (W. B. Saunders, Philadelphia, 1973), pp. 488-490, 519–527.

[22] A. Elkeles, "Sex differences in the calcification of the costal cartilages," J. Am. Geriatrics Soc. **14**, 456–461 (1966).

[23] N. Bilaniuk and G. S. K. Wong, "Speed of sound in pure water as a function of temperature," J. Acoust. Soc. Am. **93**, 1609–1612 (1993).

[24] *Handbook of Chemistry and Physics*, R. C. Weast, Ed. (CRC Press, Boca Raton, 1985), p. F-10.

[25] S. A. Goss, R. L. Johnston, and F. Dunn, "Comprehensive compilation of empirical ultrasonic properties of mammalian tissues," J. Acoust. Soc. Am. **64**, 423–457 (1978).

[26] S. A. Goss, R. L. Johnston, and F. Dunn, "Compilation of empirical ultrasonic properties of mammalian tissues II," J. Acoust. Soc. Am. **68**, 93–108 (1980).

[27] J. E. Olerud, W. O'Brien, M. A. Riederer-Henderson, D. Steiger, F. K. Forster, C. Daly, D. J. Ketterer, and G. F. Odland, "Ultrasonic assessment of skin and wounds with the scanning laser acoustic microscope," J. Invest. Derm. **8**, 615–623 (1987).

[28] R. E. Neuman and M. A. Logan, "The determination of collagen and elastin in tissues," J. Biol. Chem. **186**, 549–556 (1950).

[29] F. A. Duck, *Physical Properties of Tissue: A Comprehensive Reference Book* (Academic Press, New York, 1990).

[30] K. T. Dussik and D. J. Fritch, "Determination of sound attenuation and sound velocity in the structure constituting the joints, and of the ultrasonic field distribution within the joints on living tissues and anatomical preparations, both in normal and pathological con-

ditions," Progress Report to Public Health Service, National Institutes of Health Project A454 (15 September 1956).

[31] H. Q. Woodard and D. R. White, "The composition of body tissues," Br. J. Radiol. **59**, 1209–1219 (1986).

[32] K. H. Herzfeld and T. A. Litovitz, *Absorption and Dispersion of Ultrasonic Waves* (Academic Press, New York, 1959), pp. 353–361.

[33] Simulations were performed on a Linux workstation with an AMD K6 processor running at 200 MHz and 128 MB of random-access memory. The simulation code was written in Fortran 77 and compiled using the front end fort77 and the Fortran-to-C converter f2c with the Gnu C compiler gcc.

[34] D.-L. Liu and R. C. Waag, "Correction of ultrasonic wavefront distortion using backpropagation and a reference waveform method for time-shift compensation," J. Acoust. Soc. Am. **96**, 649–660 (1994).

[35] L. M. Hinkelman, D.-L. Liu, L. A. Metlay, and R. C. Waag, "Measurements of ultrasonic pulse arrival time and energy level variations produced by propagation through abdominal wall," J. Acoust. Soc. Am. **95**, 530–541 (1994).

[36] J. Wolff, *Das Gesetz der Transformation der Knochen* (Hirschwald, Berlin, 1892).

[37] J. C. Rice, S. C. Cowin, and J. A. Bowman, "On the dependence of the elasticity and strength of cancellous bone on apparent density," J. Biomech. **21**, 155–168 (1988).

[38] J. Y. Rho, R. B. Ashman, and C. H. Turner, "Young's modulus of trabecular and cortical bone material: ultrasonic and tensile measurements," J. Biomech. **26**, 111–119 (1993).

[39] C. H. Turner, J. Rho, Y. Takano, T. Y. Tsui, and G. M. Pharr, "The elastic properties of trabecular and cortical bone tissues are similar: results from two microscopic measurement techniques," J. Biomech. **32**, 437–441 (1999).

[40] S. Lees, J. M. Ahern, and M. Leonard, "Parameters influencing the sonic velocity in compact calcified tissues of various species," J. Acoust. Soc. Am. **74**, 28–33 (1983).

[41] S. Lees, "Sonic properties of mineralized tissues," in *Tissue Characterization with Ultrasound*, J. F. Greenleaf, Ed., (CRC Press, Boca Raton, 1986), pp. 207–226.

[42] L. A. Frizzell, E. L. Carstensen, and J. F. Dyro, "Shear properties of mammalian tissues at low MHz frequencies," J. Acoust. Soc. Am. **60**, 1409–1411 (1976).

[43] E. L. Madsen, H. J. Sathoff, and J. A. Zagzebski, "Ultrasonic shear wave properties of soft tissues and tissuelike materials," J. Acoust. Soc. Am. **74**, 1346–1355 (1983).

[44] L. Adler and K. V. Cook, "Ultrasonic properties of freshly frozen dog tibia," J. Acoust. Soc. Am. **58**, 1107–1108 (1975).

[45] S. S. Kohles, J. R. Bowers, A. C. Vailas, and R. Vanderby, "Ultrasonic wave velocity measurement in small polymeric and cortical bone specimens," J. Biomech. Eng. **119**, 232–236 (1997).

[46] K. Chandra and C. Thompson, "Ultrasonic characterization of fractal media," Proc. IEEE **81**, 1523–1533 (1993).

[47] L. M. Hinkelman and D.-L. Liu, "Measurement and analysis of ultrasonic pulse wavefront distortion produced by chest wall," Proc. 12th Ann. Univ. Rochester Diagnostic Ultras. Res. Lab. Indust. Assoc. Mtg. 8–25 (1995).

[48] T. D. Mast, A. I. Nachman, and R. C. Waag, "Focusing and imaging using eigenfunctions of the scattering operator," J. Acoust. Soc. Am. **102**, 715–725 (1997).

TABLES

TABLE I. Assumed physical properties for each tissue type employed in the simulations.

Tissue Type	Sound Speed (mm/μs)	Density (g/cc)	Absorption (dB/mm)
Water	1.524	0.993	0.0007
Fat	1.478	0.950	0.12
Muscle	1.547	1.050	0.21
Connective	1.613	1.120	0.37
Cartilage	1.665	1.098	0.97
Bone	3.540	1.990	4.37

TABLE II. Statistics of wavefront distortion caused by thirteen soft-tissue paths within chest wall cross sections. The statistics shown include the average specimen thickness for the tissue path considered, rms values and correlation lengths (CL) of the arrival time fluctuations (ATF) and the energy level fluctuations (ELF), the waveform similarity factor (WSF), and the total attenuation.

Path	Thickness (mm)	ATF rms (ns)	ATF CL (mm)	ELF rms (dB)	ELF CL (mm)	WSF	Attenuation (dB)
4L-c	15.4	32.0	0.60	1.98	1.68	0.981	5.62
4L-d	12.7	10.0	2.58	0.46	1.23	0.999	4.08
4L-e	16.0	10.0	1.37	1.61	1.74	0.998	5.26
4L-f	17.0	17.3	2.48	0.92	1.61	0.999	5.33
5L-a	11.0	11.6	0.95	1.51	1.13	0.991	4.29
5L-c	15.0	14.8	1.03	1.15	1.19	0.996	5.01
7L-a	16.2	16.8	2.64	0.95	1.29	0.999	5.46
7L-b	14.9	22.5	2.66	1.19	1.61	0.998	4.91
7R-c	17.7	17.4	1.77	2.52	2.07	0.997	5.83
7R-d	21.0	8.3	1.10	0.85	1.79	0.999	7.07
7R-e	24.7	13.7	1.37	1.06	1.62	0.997	8.69
8R-a	23.8	26.6	1.78	2.58	1.40	0.992	7.76
8R-b	22.2	29.9	1.44	1.95	1.11	0.989	6.09
Mean	17.5	17.8	1.67	1.44	1.50	0.995	5.80
St. Dev.	4.2	7.8	0.71	0.66	0.30	0.005	1.33

TABLE III. Statistics of wavefront distortion caused by fourteen tissue paths including rib structures. The footnotes associated with the label for each path indicate morphological features and physical phenomena that affected the wavefront distortion computed for that path. The format is analogous to that in Table II.

Path	Thickness (mm)	ATF rms (ns)	ATF CL (mm)	ELF rms (dB)	ELF CL (mm)	WSF	Attenuation (dB)
4L-a[1,2,3,4]	21.0	260.3	3.00	2.58	2.72	0.968	15.33
4L-b[2,3]	17.6	161.9	1.90	4.16	1.49	0.641	43.35
5L-b[2]	14.2	92.5	0.69	3.06	1.92	0.775	26.87
7L-c[3,5]	17.8	47.2	1.58	5.33	2.04	0.958	19.66
7R-a[1,3,4]	30.4	123.1	2.12	3.80	1.78	0.960	16.57
7R-b[3,5]	24.3	165.6	2.71	6.88	2.07	0.274	43.06
8L-a[3]	25.3	113.9	1.18	7.75	2.29	0.907	32.44
8L-b[1,4]	22.8	109.7	2.05	3.43	1.22	0.974	10.28
8L-c[3]	28.8	134.0	2.75	3.04	1.57	0.944	40.47
8L-d[4]	23.6	78.9	0.64	3.06	1.55	0.950	6.78
8L-e[3]	26.4	208.8	1.91	3.62	1.50	0.810	44.27
8L-f[1,4]	28.5	169.9	1.79	5.02	1.95	0.916	10.70
8L-g[3]	27.6	210.8	1.40	3.36	1.35	0.892	44.22
8R-c[2,3]	24.9	81.4	2.08	2.76	1.25	0.962	44.32

[1]Small intercostal spaces
[2]Cancellous bone
[3]Cortical bone and cartilage
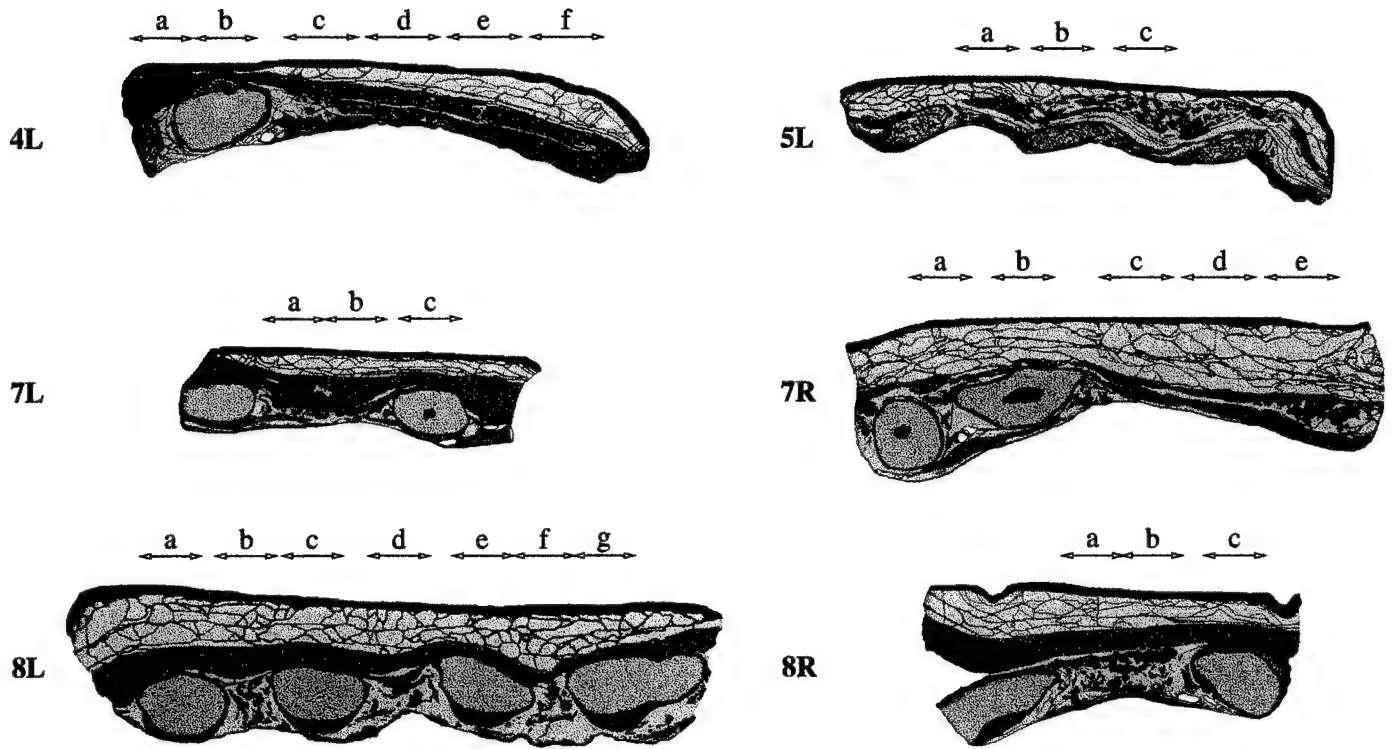[4]Strong rib reflections
[5]Cortical bone within cartilage

FIG. 1. Chest tissue maps used in simulations. Simulated apertures are indicated using lower-case letters for each cross section. Smaller arrows indicate 55-element (11.60 mm) apertures while large arrows indicate 68-element (14.28 mm) apertures.
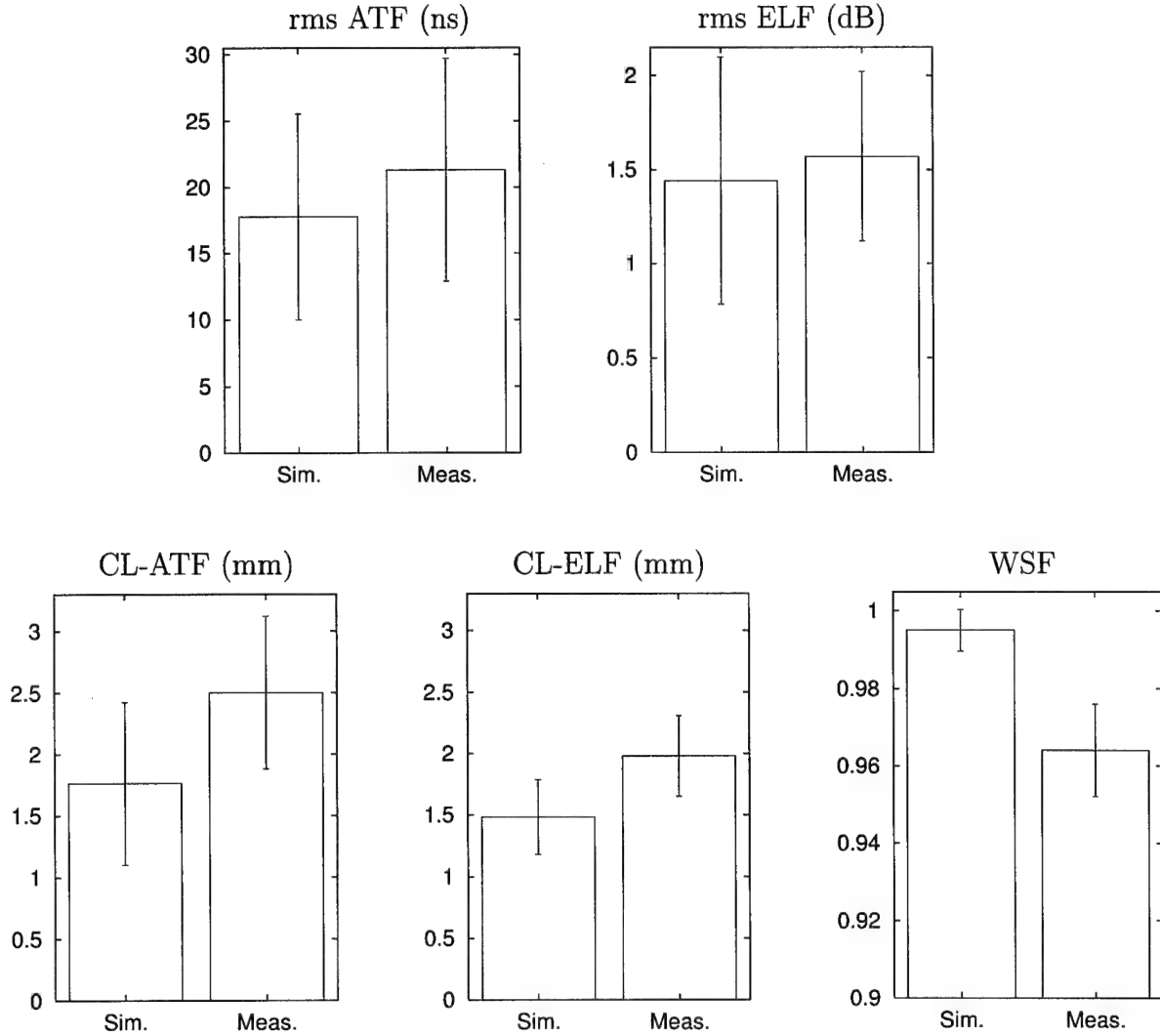
FIG. 2. Summary of distortion statistics for soft tissue paths. The bar chart shows mean values of the rms arrival time fluctuations (ATF), rms energy level fluctuations (ELF), correlations lengths (CL) of these fluctuations, and waveform similarity factors (WSF) for the simulations performed in the present paper and the experiments reported in Ref. 8. Error bars indicate a range of plus or minus one standard deviation from the mean.
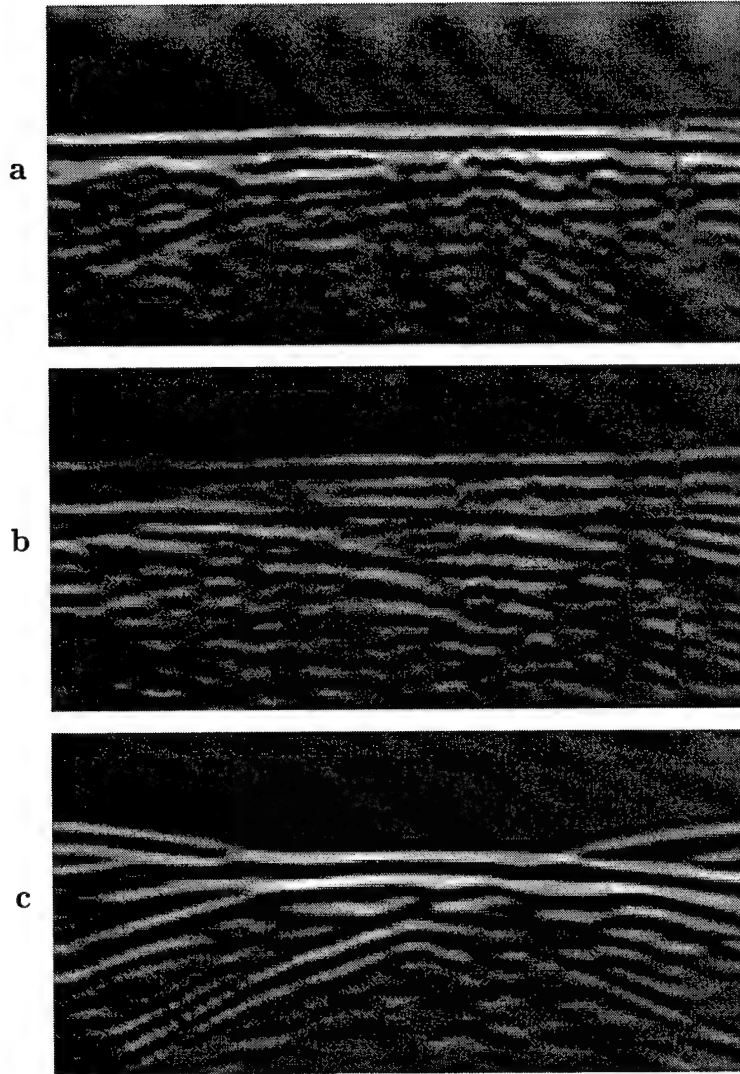
FIG. 3. Measured waveforms for three propagation paths in specimen 8L. Each panel shows received waveforms on a bipolar logarithmic gray scale with a dynamic range of 40 dB. The horizontal range shown in each panel is 20 mm and the vertical range shown is 6.4 μs. (a) Tissue path between two ribs, in azimuth direction (parallel to ribs). (b) Path including a rib, azimuth direction. (c) Tissue path including intercostal space between two ribs, elevation direction (perpendicular to ribs).
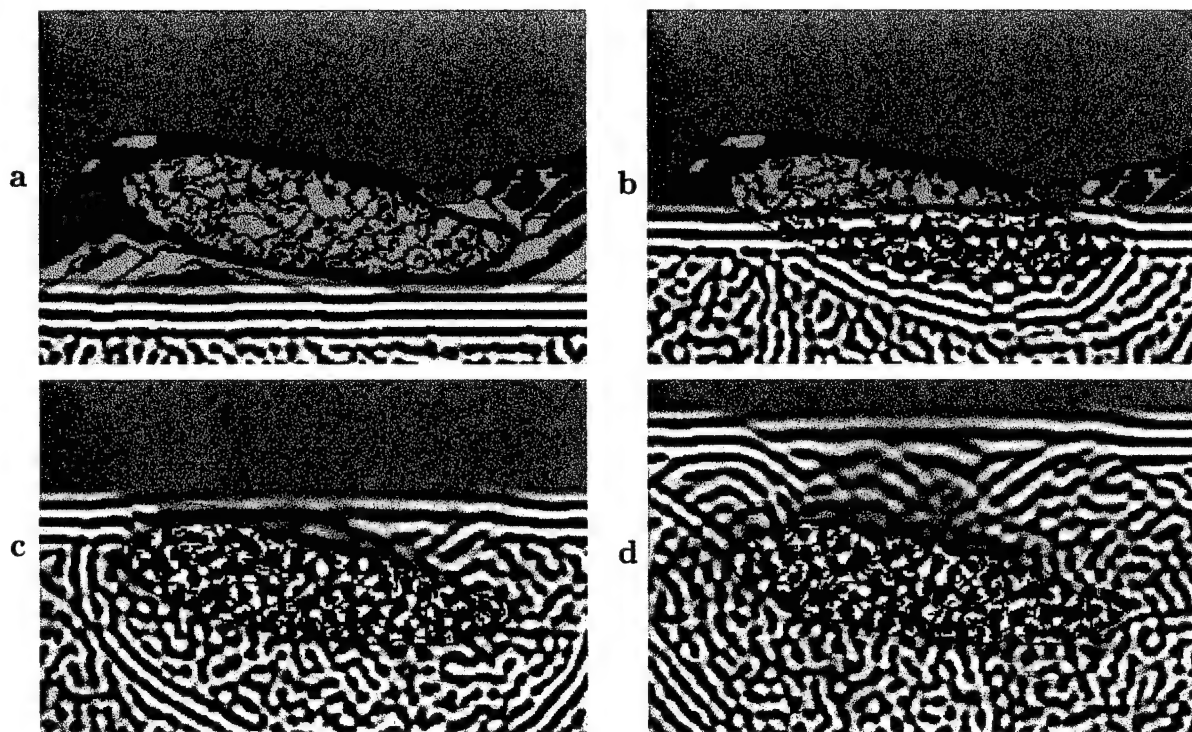
FIG. 4. Propagation through the central rib in cross section 5L (path 5L-b). Panels (a)–(d) show instantaneous acoustic pressure fields at successive intervals of 2.17 μs. Each panel shows an area that spans 20.32 mm horizontally and 14.58 mm vertically. Logarithmically compressed wavefronts are shown on a bipolar scale with black representing minimum pressure, white representing maximum pressure, and a dynamic range of 57 dB.
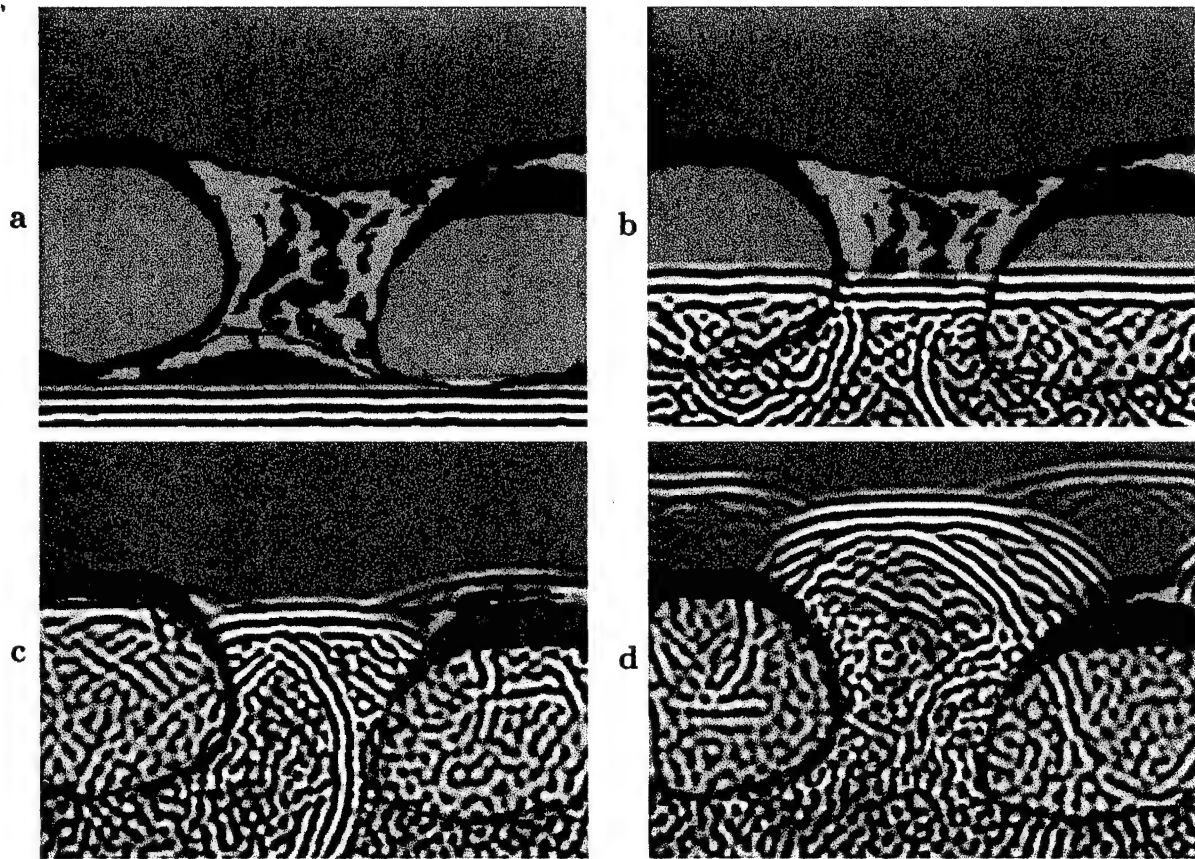
FIG. 5. Propagation through an intercostal space in cross section 8L (path 8L-b). Panels (a)–(d) show instantaneous wavefields at successive intervals of 3.62 μs. Each panel shows an area that spans 28.27 mm horizontally and 21.20 mm vertically. Wavefronts are shown using the same format as in Fig. 4.
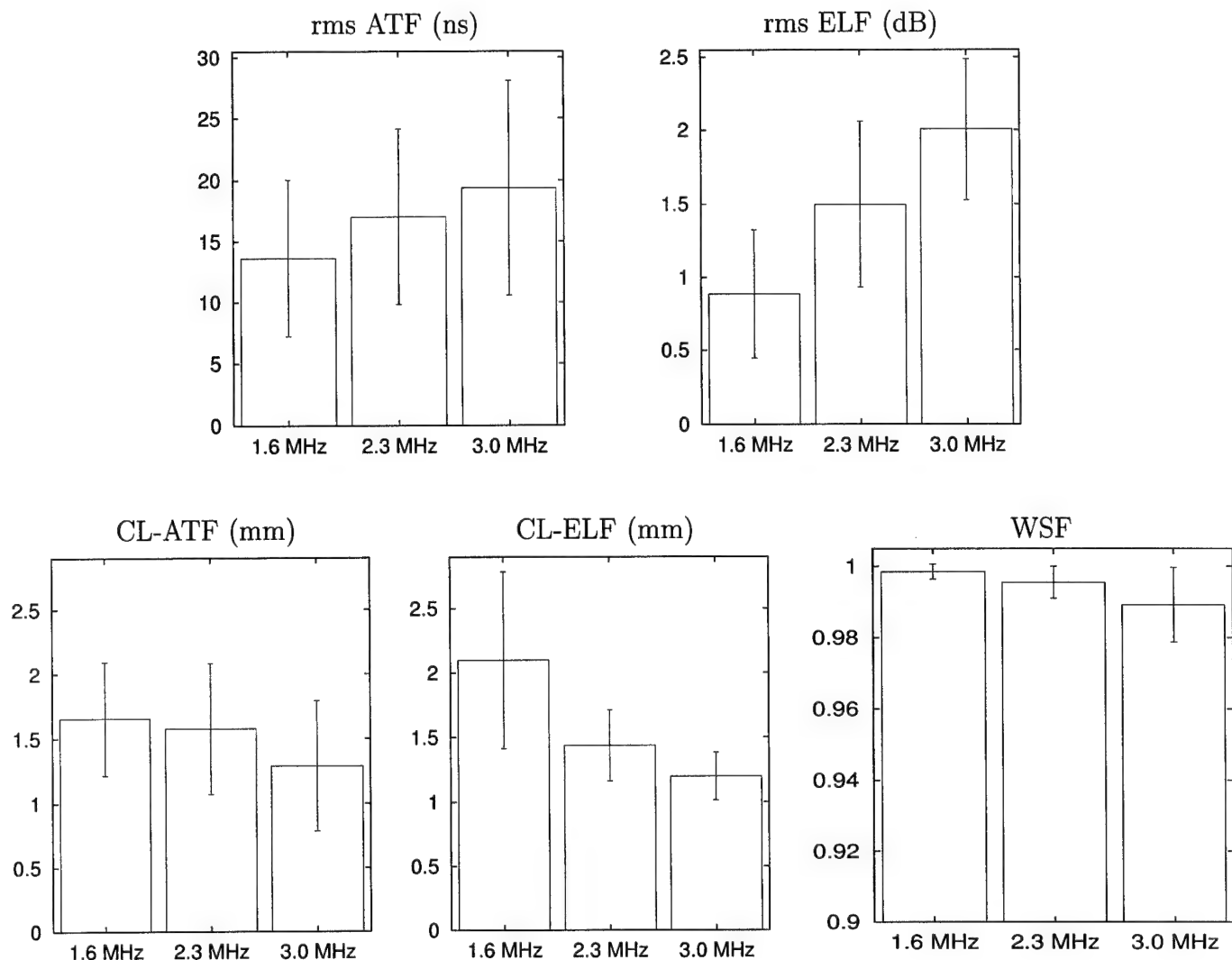
FIG. 6. Summary of frequency-dependent distortion results. Mean rms arrival time fluctuations (ATF), energy level fluctuations (ELF), correlation lengths (CL) of these fluctuations, and waveform similarity factors (WSF) are shown for each of the three pulse frequencies investigated. Error bars indicate a range of plus or minus one standard deviation from the mean.

Appendix C

A K-Space Method for Large-Scale Models
of Wave Propagation in Tissue

Submitted to

IEEE Transactions on Ultrasonics, Ferroelectrics, and Frequency Control

A k-space method for large-scale models of wave propagation in tissue

Laurent P. Souriau
Department of Electrical and Computer Engineering
University of Rochester
Rochester, NY 14627
laurent@club-internet.fr

T. Douglas Mast
Applied Research Laboratory
The Pennsylvania State University
University Park, PA 16801

D.-L. Donald Liu
Ultrasound Group
Siemens Medical Systems
Issaquah, WA 98027

Adrian I. Nachman
Department of Mathematics
University of Rochester
Rochester, NY 14627

Robert C. Waag
Departments of Electrical and Computer Engineering and Radiology
University of Rochester
Rochester, NY 14627

May 12, 1999

Abstract

Large-scale simulation of ultrasonic pulse propagation in inhomogeneous tissue is important for study of ultrasound-tissue interaction as well as for development of new imaging methods. Typical scales of interest span hundreds of wavelengths; most current two-dimensional methods, such as finite-difference and finite-element methods, are unable to compute propagation on this scale with the efficiency needed for imaging studies. Furthermore, for most available methods of simulating ultrasonic propagation, large-scale three-dimensional computations of ultrasonic scattering are infeasible. Some of these difficulties have been overcome by previous pseudospectral and k-space methods, which allow substantial portions of the necessary computations to be executed using fast Fourier transforms. This paper presents a new k-space method that has advantages of both past k-space methods and pseudospectral methods. In this method, the spatial differential equations are solved by a simple Fourier transform method and temporal iteration is performed using a k-t space propagator. The applicability of the k-space method to large-scale soft-tissue modeling is shown by simulating propagation through several tissue-mimicking cylinders as well as a model chest wall cross section. Numerical results indicate that this method is accurate for large-scale soft-tissue computations, with much greater efficiency than that of an analogous leapfrog pseudospectral method or a 2-4 finite difference time-domain method. However, numerical results also indicate that the k-space method is less accurate than the finite-difference method for a high-contrast scatterer with bone-like properties, although qualitatively reasonable results can still be obtained by the k-space method with high efficiency. Possible extensions to the method, including three-dimensional computations and inclusion of absorption effects, are discussed.

1

I. INTRODUCTION

Computation of a scattered acoustic field, given an incident wavefield and complete specification of an inhomogeneous medium, is known as the forward scattering problem. In contrast, computation of medium parameters given the incident and the scattered field is known as the inverse scattering problem. Numerical solution of the forward scattering problem is central to many aspects of ultrasonic imaging, including inverse scattering methods, numerical studies of wavefront distortion, and development of new methods for adaptive focusing.

Most methods for numerical solution of the forward scattering problem fall into one of three categories: finite-difference methods, finite-element methods, and spectral methods. Finite-difference and finite-element methods are known as local because the wave propagation equations of interest are solved at each point based only on the states of nearby points. In contrast, spectral methods such as the k-space method [1]–[6] and the pseudospectral approach [7]–[13] are called global because information from the entire wavefield is employed to solve the wave propagation equations at each point. Because of their global nature, spectral methods can be more accurate than local methods—for instance, pseudospectral methods applied to periodic problems have been shown to be equivalent to finite-difference methods of infinite order [11].

Spectral methods also have considerable advantages for large-scale forward solvers because the required storage and the number of operations per iteration can be dramatically reduced compared to local methods. This advantage occurs for two reasons. First, since spectral methods contain derivatives and/or convolutions that can be evaluated using fast Fourier transforms, the number of operations per iteration is proportional to $N \log_2 N$ for two-dimensional computations, while the number of operations per iteration is proportional to N^2 for implicit finite-element methods [14]. Second, the increased accuracy of spectral methods can allow computations to be performed on coarser grids while maintaining accuracy. For example, finite-element methods and high-order finite-difference methods typically require grid spacings on the order of eight points per minimum wavelength, while second-order finite-difference methods can require twenty points per wavelength [9]. Spectral methods, in theory, require only two points per wavelength (spatial Nyquist sampling), although for computations of propagation in inhomogeneous media, greater accuracy is achieved with grid spacings on the order of four points per wavelength [9, 10, 13].

This report addresses the problem of large-scale ultrasonic wave propagation in biological media such as human tissue. For problems of interest in medical ultrasound, domain sizes can often

exceed the capabilities of conventional forward solvers. For example, one calculation of realistic scale would be the simulated propagation of a pulse with an upper bandwidth limit of 5 MHz in a volume of dimensions 30 mm on each side and a nominal sound speed of 1.5 mm/μs, so that the minimum wavelength is 0.3 mm. For this calculation, a second-order finite-difference method (using twenty points per wavelength) would require a three-dimensional grid containing 8×10^{10} nodes, a finite-element or fourth-order finite-difference method (using ten points per wavelength) would require 1×10^9 nodes, and a spectral method (using four points per wavelength) would require 6.4×10^7 nodes. Since a grid of 6.4×10^7 single-precision complex numbers requires storage of 512 megabytes, only spectral methods are feasible for realistic three-dimensional computations on present-day computers that typically have a maximum random-access memory storage of several gigabytes. The efficiency provided by fast Fourier transform implementations of spectral algorithms is a further reason why spectral methods are a practical approach to large-scale and three-dimensional computations of ultrasonic wave propagation.

Previous spectral approaches have included pseudospectral methods, in which spatial derivatives are evaluated globally using Fourier transformation and wavefields are advanced in time using various numerical integration techniques [7]–[13]. This method has provided high accuracy in may cases; however, temporal iteration techniques that provide good accuracy for large-scale models typically require significant additional computations and/or storage of wave fields from additional time steps [12], so that the efficiency advantages of the pseudospectral approach are less than might first be expected. The k-space family of methods [1]–[6] can overcome this problem by providing explicit temporal propagators related to the Green's function for wave propagation in k-t (spatial frequency and time) space. Previous implementations of the k-space method have posed the spatial part of the wave propagation equations in an integral form that can be solved using discrete convolution [1]–[6]. Although this method has been shown to be efficient and accurate, the discrete convolution step, which employs inherently singular spatial Green's functions, can present complexities in numerical implementations.

The present paper presents an alternative derivation of the k-space method using a differential representation of the wave propagation equations. The spatial part of the wave propagation equations is solved using Fourier transforms in a manner analogous to past pseudospectral methods; this derivation is shown to be theoretically equivalent to previous integral formulations of the k-space method. Temporal iteration is performed using a k-t space propagator [2], which is shown to provide much greater accuracy than "leapfrog" iteration without significant additional computation

3

or storage requirements. Thus, the new k-space method has advantages previously associated with both pseudospectral and integral k-space methods.

Below, a derivation of the new k-space method is presented for propagation in fluid media with spatially-dependent sound speed and density. For several canonical forward problems relevant to ultrasonic imaging, the accuracy and efficiency of the k-space method is compared to a pseudospectral method employing leapfrog iteration and to a 2-4 finite difference time-domain method. The k-space and finite-difference methods are also used in an example computation for a large-scale two-dimensional tissue model. Possible extensions of the new k-space method, including multiple relaxation effects for absorption, full elastic wave propagation, perfectly matched layers for absorbing boundary conditions, three-dimensional computations, and parallelization, are discussed.

II. THEORY

A. Derivation of the k-space method

A new k-space method for solving the acoustic forward scattering problem is derived here. The method is applicable to large-scale modeling of linear ultrasonic propagation in soft tissues, which are modeled here as fluid media with spatially-dependent sound speed and density. Although the k-space method described below can be extended to include absorption effects, acoustic nonlinearity, and shear-wave propagation, these effects are neglected in this derivation for simplicity.

For a fluid medium with spatially-dependent sound speed and density, the wave equation is

$$\nabla\left(\frac{1}{\rho(\mathbf{x})}\nabla p(\mathbf{x}, t)\right) - \frac{1}{\rho(\mathbf{x})\, c(\mathbf{x})^2}\frac{\partial^2 p(\mathbf{x}, t)}{\partial t^2} = 0, \tag{1}$$

where $p(\mathbf{x}, t)$ is the acoustic perturbation in pressure, $\rho(\mathbf{x})$ is the ambient density, and $c(\mathbf{x})$ is the ambient sound speed.

By defining the normalized wavefield

$$f(\mathbf{x}, t) \equiv p(\mathbf{x}, t)/\sqrt{\rho(\mathbf{x}, t)}, \tag{2}$$

Eq. (1) can be rewritten in the form

$$\nabla^2 f(\mathbf{x}, t) - \frac{1}{c^2(\mathbf{x})}\frac{\partial^2 f(\mathbf{x}, t)}{\partial t^2} - b(\mathbf{x})\, f(\mathbf{x}, t) = 0, \tag{3}$$

where

$$b(\mathbf{x}) = \sqrt{\rho(\mathbf{x})}\,\nabla^2\left(1/\sqrt{\rho(\mathbf{x})}\right). \tag{4}$$

The normalized field f may now be split into an incident and a scattered part, $f(\mathbf{x}, t) = f_i(\mathbf{x}, t) + f_s(\mathbf{x}, t)$. The normalized incident field f_i satisfies the homogeneous wave equation

$$\nabla^2 f_i(\mathbf{x}, t) - \frac{1}{c_0^2}\frac{\partial^2 f_i(\mathbf{x}, t)}{\partial t^2} = 0, \tag{5}$$

where c_0 is a nominal "background" sound speed for the inhomogeneous medium, while the normalized scattered field f_s satisfies the inhomogeneous equation

$$\nabla^2 f_s(\mathbf{x}, t) - \frac{1}{c_0^2}\frac{\partial^2 f_s(\mathbf{x}, t)}{\partial t^2} = \left(\frac{1}{c(\mathbf{x})^2} - \frac{1}{c_0^2}\right)\frac{\partial^2 f(\mathbf{x}, t)}{\partial t^2} + b(\mathbf{x})f(\mathbf{x}, t). \tag{6}$$

The terms on the right hand side of Eq. (6) are effective sources of scattered waves, and can be written in terms of a source associated with sound speed variations,

$$v(\mathbf{x}, t) = \left(\frac{c_0^2}{c(\mathbf{x})^2} - 1\right) f(\mathbf{x}, t), \tag{7}$$

5

and a source associated with density variations,

$$q(\mathbf{x}, t) = c_0^2 \, b(\mathbf{x}) \, f(\mathbf{x}, t). \tag{8}$$

With the additional definition of an auxiliary field $w(\mathbf{x}, t) = f_s(\mathbf{x}, t) + v(\mathbf{x}, t)$, Eq. (6) can be written as

$$\nabla^2 f_s(\mathbf{x}, t) = \frac{1}{c_0^2} \frac{\partial^2 w(\mathbf{x}, t)}{\partial t^2} + b(\mathbf{x}) \, f(\mathbf{x}, t). \tag{9}$$

After spatial Fourier transformation of Eq. (9), the inhomogeneous-medium wave equation can be written as the coupled set of equations

$$\frac{\partial^2 W(\mathbf{k}, t)}{\partial t^2} = (c_0 k)^2 \, [V(\mathbf{k}, t) - W(\mathbf{k}, t)] - Q(\mathbf{k}, t) \tag{10}$$

$$v(\mathbf{x}, t) = d(\mathbf{x}) \, [f_i(\mathbf{x}, t) + w(\mathbf{x}, t)] \tag{11}$$

$$q(\mathbf{x}, t) = c_0^2 \, b(\mathbf{x}) \, [f_i(\mathbf{x}, t) + w(\mathbf{x}, t) - v(\mathbf{x}, t)], \tag{12}$$

where capital letters denote spatially Fourier transformed variables and the sound speed contrast function $d(\mathbf{x})$ is defined as

$$d(\mathbf{x}) = 1 - \frac{c(\mathbf{x})^2}{c_0^2}. \tag{13}$$

In numerical implementation of the k-space algorithm, Eq. (10) is used to advance the auxiliary field $W(\mathbf{k}, t)$ in time, Eq. (11) updates the effective source v associated with sound speed variations, and Eq. (12) updates the effective source q associated with density inhomogeneities. Notable is that the effective source v is directly proportional to the square of the sound speed variation of the medium, while the effective source q is directly proportional to the Laplacian of $1/\sqrt{\rho(\mathbf{x})}$. Thus, for a piecewise-constant inhomogeneous medium, v may be non-zero everywhere while q is nonzero (and singular) only on borders between regions.

The algorithm derived above can be considered an extension of Bojarski's formulation [1, 2], which was obtained using an integral representation of the acoustic wave equation. This can be shown by rewriting Eq. (10) using the k-t space Green's function [2]

$$G(\mathbf{k}, t - \tau) = c_0 k \, \sin[c_0 k (t - \tau)] \, H(t - \tau), \tag{14}$$

where H is the Heaviside step function. The Green's function defined by Eq. (14) satisfies the differential equation

$$\frac{\partial^2 G(\mathbf{k}, t)}{\partial t^2} + c_0^2 k^2 \, G(\mathbf{k}, t) = c_0^2 k^2 \, \delta(t). \tag{15}$$

6

For zero initial conditions, Eq. (10) can then be rewritten as

$$W(\mathbf{k}, t) = c_0 k \int_0^t \sin[c_0 k(t - \tau)] \left(V(\mathbf{k}, \tau) - \frac{1}{(c_0 k)^2} Q(\mathbf{k}, \tau) \right) d\tau. \tag{16}$$

For a medium of constant density, $Q = 0$ and Eq. (16) reduces to Eq. (56) of Ref. [2]. Thus, the present method can be considered a generalized form of Bojarski's k-space method.

Equations (10)–(12) can be written in several different discrete forms. For instance, using a second-order accurate finite-difference representation of the second-order time derivative, Eq. (10) can be written in the discrete form

$$W(\mathbf{k}, t + \Delta t) - 2 W(\mathbf{k}, t) + W(\mathbf{k}, t - \Delta t) = (c_0 k \Delta t)^2 \left[V(\mathbf{k}, t) - W(\mathbf{k}, t) - \frac{Q(\mathbf{k}, t)}{(c_0 k)^2} \right], \tag{17}$$

where Δt is the time step. This is known as "leapfrog" iteration; use of Eq. (17) in the current method is analogous to commonly used pseudospectral approaches [12, 13]. (Although increased accuracy can be achieved by higher-order methods such as fourth-order Adams-Bashforth or Adams-Moulton iteration, these methods have the disadvantage of requiring storage of the entire computational grid for additional time steps [11, 12].) A more accurate form, however, results from expanding Eq. (16) about the instants $t \pm \Delta t$ and making the approximation $V(\mathbf{k}, t) \approx (1/2)[V(\mathbf{k}, t + \Delta t/2) + V(\mathbf{k}, t - \Delta t/2)]$ [2]. This yields the k-t space propagation equation

$$W(\mathbf{k}, t + \Delta t) - 2 W(\mathbf{k}, t) + W(\mathbf{k}, t - \Delta t) = 4 \sin^2 \left(\frac{c_0 k \Delta t}{2} \right) \left[V(\mathbf{k}, t) - W(\mathbf{k}, t) - \frac{Q(\mathbf{k}, t)}{(c_0 k)^2} \right]. \tag{18}$$

Alternatively, Eq. (18) can be derived from Eq. (10) using the method of mode-dependent discretization [15], in which a difference operator is chosen to produce the same result as the differential operator on a set of chosen "coincident" functions. A natural choice for these coincident functions is the set of null functions for the differential operator of interest. Here, these are $e^{\pm i c_0 k t}$ for the operator $\partial^2/\partial t^2 + (c_0 k)^2$ that is applied to W in Eqs. (10)–(12). By applying the differential operator $\partial^2/\partial t^2 + (c_0 k)^2$ as well as its discrete form to these coincident functions and equalizing the results, Eq. (18) follows. It may also be noted that Eqs. (17) and (18) are equivalent in the limit of small Δt. However, results shown below indicate that use of the k-t propagator (18) provides much greater accuracy for larger time steps.

The present k-space algorithm can now be summarized as follows:

1. Define the contrast functions $d(\mathbf{x})$ and $b(\mathbf{x})$.

7

2. Initialize the field $w(\mathbf{x}, t)$ to zero.

3. Define the incident wave $f_i(\mathbf{x}, t)$ on the entire grid.

4. Compute $v(\mathbf{x}, t)$ using Eq. (11).

5. Compute $q(\mathbf{x}, t)$ using Eq. (12).

6. Obtain $V(\mathbf{k}, t)$, $Q(\mathbf{k}, t)$, and $W(\mathbf{k}, t)$ by FFT.

7. Evaluate $W(\mathbf{k}, t + \Delta t)$ from Eq. (17) or Eq. (18).

8. Obtain $w(\mathbf{x}, t + \Delta t)$ by inverse FFT.

9. Set $t \to t + \Delta t$ and go to (3).

To distinguish between the standard leapfrog iteration method and the improved method used here, the following nomenclature is used in the present paper. The above algorithm employing Eq. (17) for temporal iteration is referred to as a leapfrog pseudospectral method below, while the algorithm employing Eq. (18) is referred to as a k-space method. This nomenclature is used because, as shown above, the algorithm employing Eq. (18) is equivalent to an extended form of Bojarski's k-space method [2] cast in terms of differential equations rather than integral equations.

B. Numerical stability and accuracy

The stability of the method derived above can be evaluated using standard, linear von Neumann stability analysis [16]. In this technique, the difference equations that comprise Eqs. (17) and (18) are applied to a test function

$$W_{\text{test}}(\mathbf{k}, n\Delta t) = \phi(\mathbf{k})^n \, \psi(\mathbf{k}), \tag{19}$$

where $\psi(\mathbf{k})$ is a spatial-frequency domain eigenmode and $\phi(\mathbf{k})$ is a temporal amplification factor. If a difference equation admits solutions with $|\phi(\mathbf{k})| > 1$ for any vector wavenumber $\mathbf{k}$, errors may grow exponentially with time and the solution is thus unstable. If $|\phi(\mathbf{k})| \leq 1$ for all wavenumbers, then the solution is numerically stable. For simplicity, since results can depend on the inhomogeneity employed, this stability computation is performed here under the assumption of a homogeneous medium.

8

Application of this technique to Eq. (17), which represents a leapfrog pseudospectral approach, yields a quadratic equation for $\phi(\mathbf{k})$. The resulting stability condition is

$$c_{\max} k_{\max} \Delta t \leq 2, \tag{20}$$

where $c_{\max}$ is the maximum sound speed in the region of computation, $k_{\max} = \pi/\Delta x$ is the maximum wavenumber in the discrete Fourier transforms used to compute $W(\mathbf{k}, t)$, and Δt and Δx, respectively, are the temporal and spatial steps employed. Using the standard definition for a Courant-Friedrichs-Lewy (CFL) number [17], the stability condition

$$\mathrm{CFL} \equiv \frac{c_0 \Delta t}{\Delta x} \leq \frac{2}{\pi} \frac{c_0}{c_{\max}} \tag{21}$$

is obtained for the leapfrog pseudospectral method represented by Eq. (17).

Application of the same analysis to the k-space method represented by Eq. (18) yields a very different result: in the absence of inhomogeneities, the linear numerical stability of the k-space method is unconditional. An upper limit on the minimum required time step, however, arises from the requirement of sampling at the Nyquist rate: that is, the time step should be sufficiently small to allow two samples per period for the highest-frequency component of the computed field. Thus, the requirement can be written

$$\Delta t \leq \frac{1}{2 f_{\max}} = \frac{\pi}{c_{\max} k_{\max}} = \frac{\Delta x}{c_{\max}}, \tag{22}$$

or simply $\mathrm{CFL} \leq c_0/c_{\max}$.

The Fourier transform steps in the above algorithm can lead to numerical artifacts (related to the Gibbs phenomenon) when the scattering object contains discontinuities in sound speed or density. To avoid such artifacts, the scattering object can be spatially filtered to smooth discontinuities. That is, the sound-speed contrast function $c_0^2(\mathbf{x})/c^2 - 1$ and the density contrast function of Eq. (4) are replaced by filtered functions of the form

$$u_{\mathrm{filtered}}(\mathbf{x}) = \mathbf{F}^{-1}[U(\mathbf{k})\, \phi(\mathbf{k})], \tag{23}$$

in which the Fourier transform $U(\mathbf{k})$ of the function $u(\mathbf{x})$ is multiplied by a low-pass spatial-frequency filter $\phi(\mathbf{k})$. In the present study, the filter employed is the spatial-frequency Blackman window [18]

$$\phi(\mathbf{k}) = 0.42 + 0.5\cos\left(\frac{\pi k}{k_{\max}}\right) + 0.08\cos\left(\frac{2\pi k}{k_{\max}}\right). \tag{24}$$

9

Spatial-frequency windowing, like that represented by Eq. (24), naturally reduces high spatial-frequency components of the wavefield, so such windowing may also allow use of larger time steps while still meeting the Nyquist criterion of Eq. (22).

III. Numerical Methods

Numerical implementation of the new k-space algorithm was accomplished using the algorithm described above. The normalized incident wave $f_i(\mathbf{x}, t)$ was defined as a plane wave with Gaussian temporal shape,

$$f_i(\mathbf{x}, t) = \rho(\mathbf{x})^{-\frac{1}{2}} \sin(\omega_0 \tau) \, e^{-\tau^2/(2\sigma^2)}, \tag{25}$$

where τ is the retarded time $\tau = t - (x - x_0)/c_0$ and x_0 is the initial central position of the wave. Boundary conditions were implicitly periodic.

Wavefields were computed on two-dimensional grids chosen to be large enough to avoid influence of "wraparound" error within the temporal window of interest. All k-space computations were performed on square grids of size N by N. Prior to execution of the main computation loop, the Laplacian occurring in Eq. (4) was evaluated using second-order accurate, centered finite-difference representations of the second derivative in each direction. Within the main computational loop, all spatial derivatives were evaluated by Fourier transformation, implemented using a fast Fourier transform (FFT) algorithm [20]. For maximum FFT efficiency, grid sizes N were chosen to be integers with prime factors no higher than 3. In some cases, wavefields were computed on a grid of size smaller than N and the fields were zero-padded to size N by N.

The spatial-frequency time-domain wavefield $W(\mathbf{k}, t + \Delta t)$ was windowed using the rectangular window

$$\phi(\mathbf{k}) = H(k_{\max} - k), \tag{26}$$

before inversion to yield $w(\mathbf{x}, t + \Delta t)$. (That is, between steps 7 and 8 in the algorithm enumerated above.) In Eq. (26), H is, as before, the Heaviside step function, $k_{\max}$ is the maximum wavenumber magnitude (equal to $\pi/\Delta x$), and k is the magnitude of the vector wavenumber $\mathbf{k}$. In some cases, the contrast functions $b(\mathbf{x})$ and $d(\mathbf{x})$ were also smoothed by windowing in the spatial-frequency domain using Eq. (24) with a wavenumber cutoff equal to $\pi/\Delta x$.

For comparison, wavefields were also computed using a second-order in time, fourth-order in space finite-difference method, described in Refs. [17] and [19]–[23]. For the finite-difference computations, the incident wave was specified by a single initial condition rather than updated at each time step. Periodic boundary conditions were applied on the sides perpendicular to the wavefront, while first-order radiation boundary conditions [23] were applied on the sides parallel to the wavefront. Time steps were determined using a CFL number of 0.25, which is a natural choice for this finite-difference method [21]. To reduce the computational burden, domain sizes were

11

minimized in the dimension for which the radiation boundary conditions eliminated wraparound errors. As in Refs. [23]–[25], computations were performed at each time step only on portions of the grid where the wavefields were nonzero; this reduces the required computation time for the finite-difference method by about one half.

To quantitatively test the accuracy of the k-space and finite-difference methods, benchmark computations were performed using an exact series solution for the scattering of a plane wave by a fluid cylinder [26]. The sampling rate and waveform shape were chosen to match the time-domain simulation data for the case of interest. The pressure field was then computed for each frequency component with relative magnitude within 60 dB of the peak magnitude. Each single-frequency computation truncated the series at the term having a relative contribution less than 10^{-12} times the sum of all terms. The frequency-domain scattered fields were then inverted by FFT to obtain exact numerical solutions for the time-domain pressure fields at the simulated measurement points.

Benchmark studies of accuracy were performed using a cylinder with radius 2.0 mm and acoustic properties of human fat, and a background medium with acoustic properties of water at body temperature. Rationale for use of these values is discussed in Ref. [23]. The cylinder had a sound speed of 1.478 mm/μs and a density of 0.950 g/mm^3, while the background medium had a sound speed of 1.524 mm/μs and a density of 0.993 g/mm^3. The incident pulse was a plane wave with Gaussian temporal characteristics, a temporal Gaussian parameter $\sigma = 0.25$ μs, and a central starting position of $x = -4.5$ mm at time zero. For this pulse, a nominal maximum frequency is 4.43 MHz, corresponding to the spectral point 40 dB down from the center frequency (for the benchmark problem, this frequency corresponds to a minimum wavelength of 0.334 mm). The k-space, leapfrog pseudospectral, finite-difference, and exact methods described above were used to compute time histories of the total pressure field at 128 equally-spaced "measurement" points spanning a circle of radius 2.5 mm concentric to the cylinder. The domain size for each computation employing this cylinder was 9.5×9.5 mm^2.

Further studies of accuracy were performed using a cylinder of radius 10 mm. Other parameters were as described above for the small problem, except that the radius of the measurement circle was 12.5 mm and the starting position of the wavefront was $x = -14.5$ mm. The k-space method was employed to compute two cases corresponding to unsmoothed and smoothed contrast functions, using a spatial step of four points per minimum wavelength and a CFL number of 0.5. In each k-space computation for this cylinder, the domain size employed was 72×72 mm^2. The finite-difference method was employed to compute a single case, using a spatial step of fourteen points

12

per minimum wavelength and a CFL number of 0.25. Because storage requirements proved to be large for this finite-difference computation, the computational configuration was modified to employ a finite-width plane wave with a 13% cosine taper, as well as radiation conditions on all computational boundaries. These modifications, which were performed only for the large cylinder case, allowed reduction of the domain size to 32×32 mm^2, so that the computation could be performed within the storage limits of the computer employed.

To evaluate the relative accuracy and efficiency of the k-space and finite-difference methods for a high-contrast scatterer, computations were also performed using a cylinder of radius 2.0 mm with the sound speed and density of human bone. The values employed were a sound speed of 3.54 mm/μs and a density of 1.99 g/mm^3, as in Ref. [25]. The incident pulse, receiver, and computational domain characteristics were identical to those for the 2.0 mm "fat" cylinder case described above.

In all of the above accuracy tests, a quantitative measure of the accuracy was obtained using the time-domain L^2 error of each approximate pressure field $p_{\text{approx}}(\mathbf{x}, t)$ versus the corresponding exact series solution $p_{\text{exact}}(\mathbf{x}, t)$. This quantity has the definition

$$\epsilon = \frac{\iint |p_{\text{approx}}(\mathbf{x}_r, t) - p_{\text{exact}}(\mathbf{x}_r, t)|^2 \, dx_r \, dt}{\iint |p_{\text{exact}}(\mathbf{x}_r, t)|^2 \, dx_r \, dt}, \tag{27}$$

where the integrals are evaluated using discrete summation over all receiver points x_r and the entire time span of the computations. Eq. (27) represents an accuracy criterion that is much stricter than more general criteria, such as comparison of the rms waveform amplitude or the amplitude and phase at the center frequency. To achieve a low L^2 error by the definition of Eq. (27), both the waveform amplitude and phase must be accurately computed for all significant frequency components of the field.

Lastly, the use of the present k-space method in a more realistic simulation of ultrasonic propagation was also tested. For this purpose, a cross-sectional tissue map of the human chest wall [25] was used as the simulated medium. A pulse center frequency of 3.0 MHz was employed together with a temporal Gaussian parameter of 0.4766 μs; these parameters correspond to the highest center frequency employed in the simulation study reported in Ref. [25]. The corresponding nominal minimum wavelength is 0.3252 mm. The k-space computation employed 4 points per minimum wavelength, a CFL number of 0.5, and a grid size of 54.9×54.9 mm^2. The finite-difference computation employed 14 points per minimum wavelength, a CFL number of 0.25, and a grid size of 38.5×29.7 mm^2.

13

IV. Numerical Results

An example k-space computation, performed using the 2.0 mm cylinder with acoustic properties of human fat, is illustrated in Fig. 1. The cylinder boundary is also sketched in each panel. For the computation shown, the contrast functions $d(\mathbf{x})$ and $b(\mathbf{x})$, which are related to the spatially-dependent sound speed and density by Eqs. (13) and (4), respectively, were smoothed using Eq. 24. The time history of the total wavefield is shown as computed by the k-space method for a spatial step size of four points per minimum wavelength and a CFL number of 0.5. Details visible include a scattered wave from the edge nearest the initial wavefront (panel 3), some spurious oscillations near the -60 dB level (panels 4–6), weak focusing near the trailing edge of the cylinder (panel 5), and scattering from the trailing edge (panels 6–9).

Results of accuracy benchmarks for the k-space and leapfrog pseudospectral methods described above are shown in Fig. 2. Each of these computations was made using the 2.0 mm radius cylinder described above and a spatial step size of four points per maximum wavelength. The results show that the k-space method employing the k-t space propagator of Eq. (18) provides much higher accuracy than the pseudospectral method employing the leapfrog propagator of Eq. (17). The two methods provide equivalent results for very small time steps (CFL numbers less than about 0.1), but the k-space method maintains its highest accuracy up to a CFL number of about 0.7. In contrast, the pseudospectral method rapidly increases in error for CFL numbers above 0.1.

Error results for the pseudospectral computations shown in Fig. 2 are not given for CFL numbers above 0.6 because, for higher CFL numbers, the computation was unstable. (Computed fields incurred spurious exponential growth, resulting in numerical overflow.) This observation of instability is consistent with the theoretical stability limit of 0.6366 given by Eq. (21) for this case. Although the k-space method did not incur any numerical instability for the range of CFL numbers investigated, the error of this method grows as the CFL number approaches and exceeds unity, consistent with the Nyquist sampling criterion given by Eq. (22).

The relative accuracy of the k-space and finite-difference methods are compared in Fig. 3 as a function of the spatial step size. For these computations, the CFL number of the k-space computations was held constant at 0.5, consistent with the range of accuracy shown in Fig. 2, while the CFL number of the finite-difference computations was held at 0.25 [21]. Both methods achieve high accuracy as the grid spacing becomes finer; however, the k-space method achieves higher accuracy for much larger spatial step sizes. The L^2 error drops below 0.05 for k-space computations

employing only four points per minimum wavelength, while achievement of the same accuracy criterion requires 16 points per minimum wavelength for the finite-difference computations. This difference suggests that storage requirements for k-space computations can be much smaller than those for finite-difference computations of comparable accuracy: on the order of 16 times smaller for two-dimensional computations and 64 times smaller for three-dimensional computations.

Visual comparison of simulated waveforms for the 2.0 mm diameter cylinder is shown in Fig. 4. Waveforms in this figure are those computed using the k-space (four points per minimum wavelength, CFL number 0.5, with both unsmoothed and smoothed contrast functions), finite-difference time-domain (14 points per minimum wavelength, CFL number 0.25), and exact methods. The k-space solution for the unsmoothed cylinder shows the smallest time-domain L^2 error (0.0347), but also exhibits spurious waves (nearly 60 dB down from the peak pressure amplitude) between the two main arrivals. These spurious waves are removed by use of the k-space method with smoothed contrast functions (*i.e.*, $b(\mathbf{x})$ from Eq. (4) and $d(\mathbf{x})$ from Eq. (13) smoothed using Eq. (24) with $k_{\max} = \pi/\Delta x$), but the L^2 error is increased to 0.0414 by this smoothing. Visual inspection of Fig. 4(b) indicates that the amplitude of the backscattered wave is underpredicted by the k-space method when smoothed contrast functions are employed. The finite-difference result bears a strong qualitative resemblance to the exact solution, but the larger L^2 error (0.0529) indicates that phase errors have been introduced by the dispersion inherent to the finite-difference method. Computation times (CPU times for a Linux workstation with an AMD K6 processor running at 200 MHz) were 4.15 minutes for the k-space method and 46.8 minutes for the finite-difference method, so that the k-space method yields comparable accuracy at much less computational cost.

Waveforms for the 10 mm diameter cylinder are shown in Fig. 5 in a format analogous to that of Fig. 4. These results indicate that, as for the smaller cylinder, smoothing of the contrast functions produces a reduction in spurious low-amplitude waves. For this problem, unlike the 2.0 mm diameter cylinder discussed above, this smoothing slightly increases the overall accuracy. (The time-domain L^2 error is 0.1080 for the smoothed case versus 0.1103 for the unsmoothed case.) The finite-difference solution, using 14 points per wavelength and a CFL number of 0.25, requires longer computation time (14.50 hours vs. 4.61 hours) and produces waveforms with poorer accuracy (an L^2 error of 0.1763) than the k-space method.

Results for the 2 mm "bone" cylinder are shown in Fig. 6. In this case, the k-space method using a CFL number of 0.5 exhibited numerical instability, possibly associated with the failure of this CFL number to meet the Nyquist condition of Eq. (22). To maintain a consistent temporal sampling

rate, the time step was reduced in proportion to the increase in $c_{\max}$, resulting in a CFL number of 0.2153. Required computation time for the k-space method was 9.9 minutes; the time-domain L^2 error was 0.3072 for the unsmoothed case and 0.8551 for the smoothed case. As can be seen in Fig. 6, the k-space computation with smoothing reduces the level of spurious wave-like artifacts, but shows some wavefield details less accurately than the computation without smoothing. For the k-space method without smoothing, reduction of the time step by an additional factor of two resulted in negligible accuracy improvement (L^2 error 0.3062) and a doubling of the computation time to 19.7 minutes.

For the "bone" cylinder, the finite-difference method, employing 14 points per wavelength and a CFL number of 0.1076 (also changed in proportion to $c_{\max}$), achieved an L^2 error of 0.0541 in a computation time of 189 minutes. This result indicates that finite-difference methods can be much more accurate than k-space methods for scattering problems involving very high-contrast inhomogeneities such as bone within soft tissue. This discrepancy is likely to be associated with inaccurate representation of high-spatial frequency components of the effective sources However, the k-space solution, as seen in Fig. 6, still shows good qualitative agreement with the exact solution.

The relative inaccuracy of the k-space method for high-contrast scatterers may be associated with aliasing effects, as suggested in Ref. [5]. That is, large jumps in spatial contrast functions are associated with significant high-frequency components of the corresponding k-space spectra. If the spatial-frequency range employed in the k-space algorithm is not sufficiently large, aliasing errors result. Smoothing the contrast functions removes this aliasing but introduces additional errors because the contrast functions are replaced by approximations. In general, removal of aliasing errors requires a decrease in the spatial step size so that the range of covered spatial frequencies is increased. To demonstrate the effect of spatial-frequency coverage, a test employing finer spatial and temporal sampling (spatial step of 0.0371 mm, 512×512 grid points, CFL number held at 0.2153) was carried out for the "bone" cylinder. The required computation time increased to 136 minutes, comparable to the finite-difference computation time of 189 minutes. Despite this increased computational cost, the time-domain L^2 error increased from 0.3072 to 0.4081 for the unsmoothed case and decreased only to 0.6841 from 0.8551 for the smoothed case. This indicates that the aliasing errors were not significantly reduced by this increase in k-space coverage; to achieve accuracy comparable to finite-difference computations for this high-contrast object, computational and storage costs much greater than those for the finite-difference method may be required.

Computational results for a large-scale two-dimensional tissue model are shown in Fig. 7.

16

Waveforms computed by the k-space (four points per minimum wavelength, CFL number 0.5, no smoothing) and the finite-difference (ten points per minimum wavelength, CFL number 0.25) were recorded at 130-element apertures composed of simulated point receivers separated by a pitch of 0.21 mm. The results produced by the finite-difference method and the k-space method are visually indistinguishable. However, despite the reduced grid size and limited computations employed for the finite-difference method, the k-space method was more efficient by about a factor of four: the required CPU time for the k-space method was 1.28 hours, while the corresponding time for the finite-difference time-domain method was 5.14 hours. This discrepancy in efficiency is even more impressive when note is made that the k-space method using 4 points per minimum wavelength provides significantly higher accuracy than the finite-difference method using 10 points per minimum wavelength (see Fig. 3). Thus, the present k-space method may be an appropriate replacement for finite-difference methods previously employed to compute propagation through large-scale soft-tissue models [23]–[25].

V. Extensions to the k-Space Method

The present method can be extended in a number of ways to increase its range of applicability in computations of ultrasound-tissue interactions.

Absorption effects could be added to the present algorithm in one of several ways. The most straightforward method for including absorption is to include an *ad hoc* damping term proportional to $\partial f/\partial t$ in Eq. (3) [3]–[5]. This approach yields absorption coefficients proportional to the square of the frequency. Alternatively, the sound speed c can be replaced with a complex sound speed including an imaginary part associated with absorption; this approach results in absorption coefficients directly proportional to the frequency. However, neither of these approaches has a rigorous justification for use in models of ultrasound propagation in biological tissue.

A physically justifiable approach for inclusion of absorption in the present algorithm is to consider absorption associated with multiple relaxation processes. The theoretical basis for this approach is presented in Ref. [27]; one implementation of this method in a finite-difference time-domain algorithm is given in Ref. [28]. Since multiple relaxation processes can lead to a variety of frequency-dependent absorption characteristics, this approach provides a possibility of modeling realistic frequency-dependent attenuation in tissue without introduction of nonphysical dispersion or violation of causality. Following the methods presented in Ref. [28], absorption due to multiple relaxation processes can be implemented in a computationally efficient form. Possible alternatives include the time-causal absorption formulation of Ref. [29].

Another possible extension to the present method is to incorporate the full elastic wave propagation equations. This extension would account for shear wave propagation, which could substantially affect results for propagation models including bone and other calcified tissue. By applying methods similar to those outlined in Refs. [6] and [13] to the algorithm described above, a full elastic k-space method incorporating Fourier-space evaluation of spatial derivatives and a k-t space propagator could be implemented.

Boundary conditions of k-space and pseudospectral methods are inherently periodic, so that simple radiation boundary conditions cannot be straightforwardly implemented. Instead, the technique of perfectly matched layers [30] may be used in a manner that reduces all waves to near zero amplitude at the boundaries [12, 13, 28]. Extension of the present method to include perfectly matched layers is straightforward.

Finally, although all implementations shown in the present paper are two-dimensional, the

18

present method can be applied directly to three-dimensional wave propagation without any formal changes. This is possible because the k-t space Green's function has an identical form for any number of spatial dimensions [2]. To implement the present methods for three-dimensional computations, the algorithm outlined above is simply employed using three-dimensional discrete Fourier transforms.

Computation times for the k-space method can easily be reduced by parallelization. The primary computational burden of the method is incurred in the multidimensional fast Fourier transforms (FFT) taken at each time step. Since FFT's can be efficiently executed on parallel processors [31, 32], the present k-space method should scale efficiently to large problems that require parallel processing.

VI. Conclusions

A new k-space method for computation of ultrasonic wave propagation has been presented. The method efficiently accounts for sound speed and density variations, and can be extended to include realistic absorption effects and absorbing boundary conditions. Three-dimensional computations can also be performed without change to the algorithm as derived here.

Numerical results have shown that the new k-space method provides superior stability and accuracy over both a similar leapfrog pseudospectral method and a fourth-order space, second-order time, finite-difference method. Because of this improved accuracy, the new method allows larger spatial and time steps to be employed, so that large-scale multidimensional computations are more feasible using the new method. Computations using a realistic two-dimensional tissue model support the finding that the k-space method provides high accuracy and low computational cost for large-scale computations.

The results also indicate that care should be taken when choosing and implementing a forward solver for a particular scattering problem. For instance, in the present k-space method, one can suppress spurious waves by smoothing of contrast functions; however, this smoothing can greatly increase the time-domain L^2 error in some cases. Likewise, the finite-difference time-domain method employed here is less accurate than the k-space method in most cases examined here, but achieved higher accuracy for a test case with a bone-like scatterer. In general, the k-space method proposed here should be most applicable to large-scale scattering problems involving low-contrast inhomogeneities such as soft tissue structures.

Acknowledgments

References

[1] N. N. Bojarski, "The k-space formulation of the scattering problem in the time domain," *J. Acoust. Soc. Am.*, vol. 72, pp. 570–584, 1982.

[2] N. N. Bojarski, "The k-space formulation of the scattering problem in the time domain: an improved single propagator formulation," *J. Acoust. Soc. Am.*, vol. 77, pp. 826–831, 1985.

[3] B. Compani-Tabrizi, "K-space formulation of the absorptive full fluid elastic scalar wave equation in the time domain," *J. Acoust. Soc. Am.*, vol. 79, pp. 901–905, 1986.

[4] S. Finette, "A computer model of acoustic wave scattering in soft tissue," *IEEE Trans. Biomed. Eng.*, vol 34, pp. 336–344, 1987.

[5] S. Finette, "Computational methods for simulating ultrasound scattering in soft tissue," *IEEE Trans. Ultrason., Ferroelect., Freq. Contr.*, vol. 34, pp. 283–292, 1987.

[6] Q. H. Liu, "Generalization of the k-space formulation to elastodynamic scattering problems," *J. Acoust. Soc. Am.,*, vol. 97, pp. 1373–1379, 1995.

[7] H.-O. Kreiss and J. Oliger, "Comparison of accurate methods for the integration of hyperbolic equations," *Tellus*, vol. 24, pp. 199–215, 1972.

[8] B. Fornberg, "On a Fourier method for the integration of hyperbolic equations," *SIAM J. Numer. Anal.*, vol. 12, pp. 509–528, 1975.

[9] D. Gottlieb and S. A. Orszag, *Numerical Analysis of Spectral Methods*, Philadelphia: SIAM, 1977.

[10] D. C. Witte and P. G. Richards, "The pseudospectral method for simulating wave propagation," in *Computational Acoustics*, D. Lee, A. Cakmak, and R. Vichnevetsky, Eds., vol. 3, pp 1–18, New York: North-Holland, 1990.

[11] B. Fornberg, *A Practical Guide to Pseudospectral Methods*, Ch. 3, Cambridge: Cambridge University Press, 1996.

[12] G. Wojcik, B. Fornberg, R. Waag, L. Carcione, J. Mould, L. Nikodym, and T. Driscoll, "Pseudospectral methods for large-scale bioacoustic models," *Proc. IEEE Ultrason. Symp.*, 1997, vol. 2, pp. 1501–1506.

[13] Q. H. Liu, "The pseudospectral time-domain (PSTD) algorithm for acoustic waves in absorptive media," *IEEE Trans. Ultrason., Ferroelect., Freq. Contr.*, vol. 45, pp. 1044–1055, 1998.

[14] B. Irons and S. Ahmad, *Techniques of Finite Elements*, Chichester: Ellis Horwood Limited, 1980.

[15] C.-C. J. Kuo and B. C. Levy, "Mode-dependent finite-difference discretization of linear homogeneous differential equations," *SIAM J. Scient. Statist. Comput.*, vol. 9, pp. 992–1015, 1988.

[16] E. H. Twizell, *Computational Methods for Partial Differential Equations*, New York: Ellis Horwood Limited, 1984.

[17] E. Turkel, "On the practical use of high-order methods for hyperbolic systems," *J. Comp. Phys.*, vol. 35, pp. 319–340, 1980.

[18] F. J. Harris, "On the use of windows for harmonic analysis with the discrete Fourier transform," *Proc. IEEE*, vol. 66, pp. 51–84, 1978.

[19] R. W. MacCormack, "Numerical solution of the interaction of a shock wave with a laminar boundary layer," in *Lecture Notes in Physics*, J. Ehlers, K. Hepp, and H. A. Weidenmüller, Eds., vol. 8, pp. 151–163, Berlin: Springer-Verlag, 1971.

[20] P. N. Swarztrauber, "Vectorizing the FFTs," in *Parallel Computations*, G. Rodrigue, Ed., New York: Academic Press, 1982.

[21] D. Gottlieb and A. Turkel, "Dissipative two-four methods for time-dependent problems," *Math. Comp.*, vol. 30, pp. 703–723, 1976.

[22] V. W. Sparrow and R. Raspet, "A numerical method for general finite amplitude wave propagation and its application to spark pulses," *J. Acoust. Soc. Am.*, vol. 90, pp. 2683–2691, 1991.

[23] T. D. Mast, L. M. Hinkelman, M. J. Orr, V. W. Sparrow, and R. C. Waag, "Simulation of ultrasonic pulse propagation through the abdominal wall," *J. Acoust. Soc. Am.*, vol. 102, pp. 1177–1190, 1998. [Erratum: *J. Acoust. Soc. Am.*, vol. 104, pp. 1124–1125, 1998.]

[24] T. D. Mast, L. M. Hinkelman, M. J. Orr, and R. C. Waag, "The effect of abdominal wall morphology on ultrasonic pulse distortion. Part II. Simulations," *J. Acoust. Soc. Am,* vol. 104, pp. 3651–3664, 1998.

[25] T. D. Mast, L. M. Hinkelman, M. J. Orr, and R. C. Waag, "Simulation of ultrasonic pulse propagation, distortion, and attenuation in the human chest wall," submitted to *J. Acoust. Soc. Am.,* 1999.

[26] P. M. Morse and K. U. Ingard, *Theoretical Acoustics,* Ch. 8, New York: McGraw-Hill, 1968.

[27] A. I. Nachman, J. Smith, and R. C. Waag, "An equation for acoustic propagation in inhomogeneous media with relaxation losses," *J. Acoust. Soc. Am.,* vol. 88, pp. 1584–1595, 1990.

[28] X. Yuan, D. Borup, J. Wiskin, M. Berggren, and S. Johnson, "Simulation of acoustic wave propagation in dispersive media with relaxation losses by using FDTD method with PML absorbing boundary condition," *IEEE Trans. Ultrason., Ferroelect., Freq. Contr.,* vol. 46, pp. 14–23, 1999.

[29] T. L. Szabo, "Time domain wave equations for lossy media obeying a frequency power law," *J. Acoust. Soc. Am.,* vol. 96, pp. 491–500, 1994.

[30] J.-P. Berenger, "A perfectly matched layer for the absorption of electromagnetic waves," *J. Comput. Phys.,* vol. 114, pp. 185–200, 1994.

[31] P. N. Swarztrauber, "Multiprocessor FFTs," *Parallel Computing,* vol. 5, pp. 197–210, 1987.

[32] A. Dubey, M. Zubair and C.E. Grosch, "A general purpose subroutine for fast Fourier transform on a distributed memory parallel machine," *Parallel Computing,* vol. 20, pp. 1697–1710, 1994.
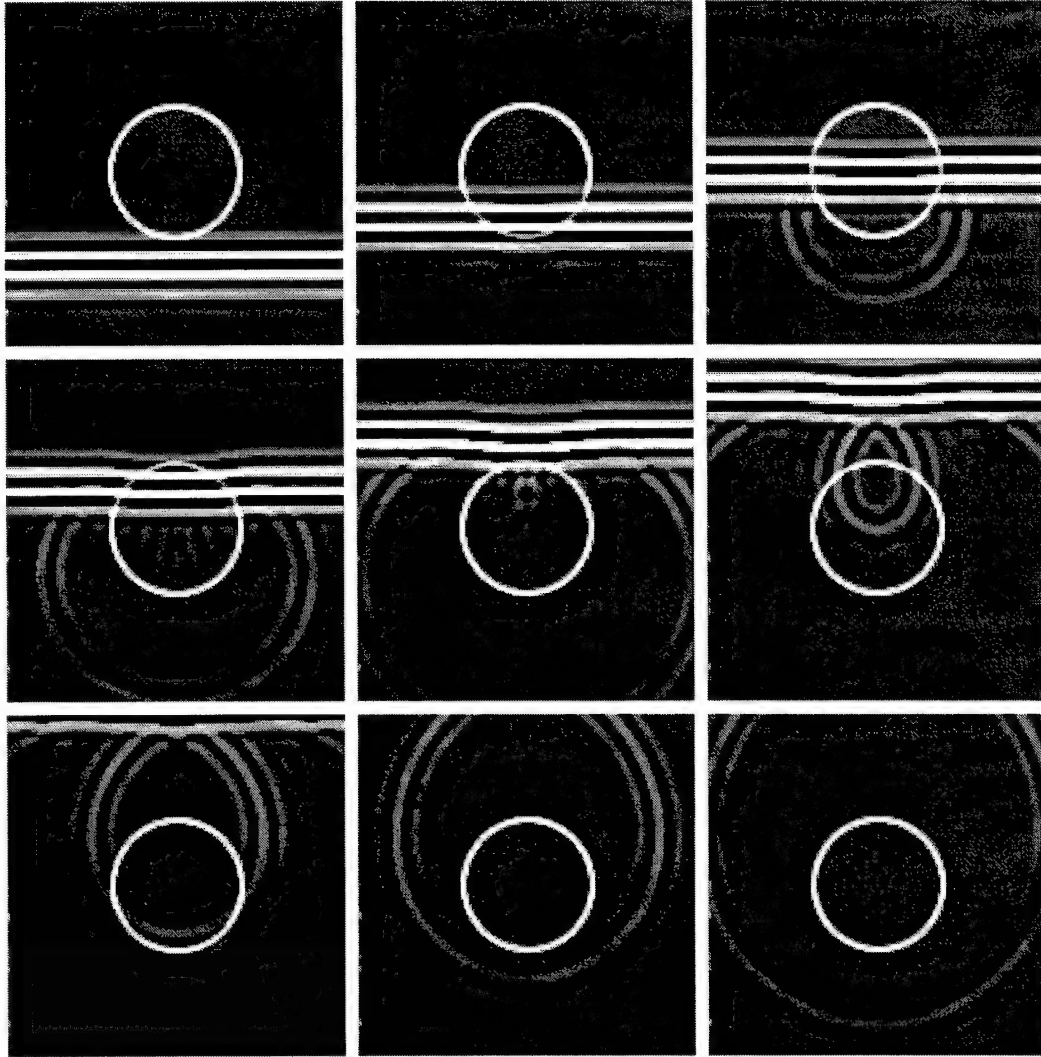
Figure 1: Time history of total acoustic pressure computed by the k-space method for a cylinder of 2.0 mm radius and fat-mimicking acoustic properties. The cylinder boundary is sketched in white. The first panel shows the wavefield impinging on the cylinder at time $t = 0.96$ μs and subsequent panels (progressing from left to right and top to bottom) show the total wavefield at intervals of 0.96 μs. The acoustic pressure is plotted in all panels using a bipolar logarithmic scale with a 60 dB dynamic range.
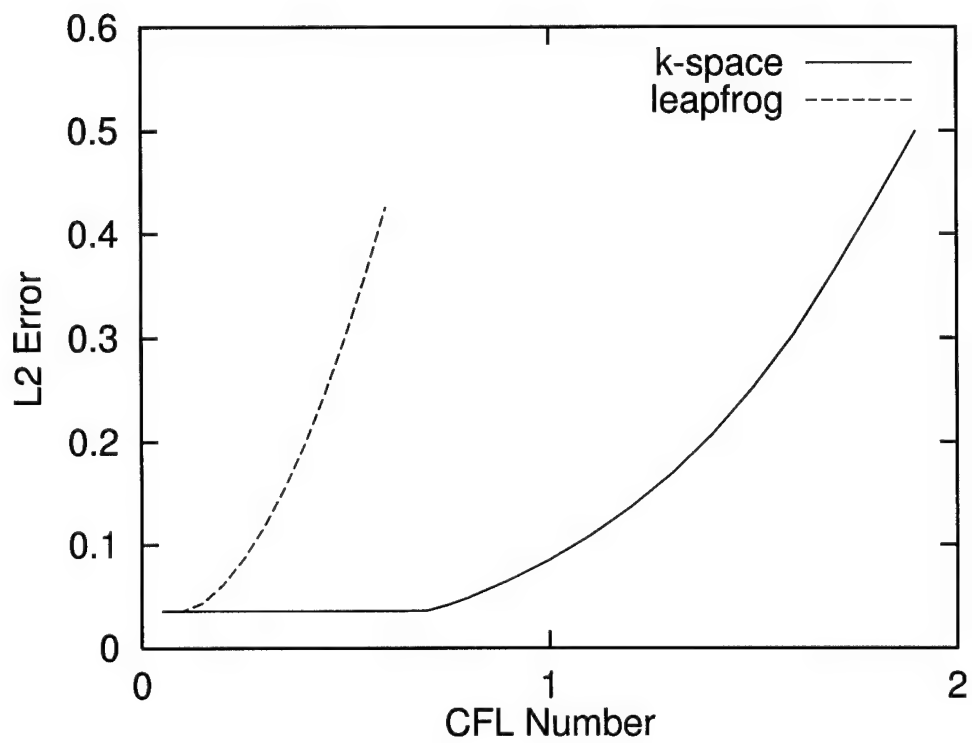
Figure 2: Time-domain comparison of accuracy for the k-space and leapfrog pseudospectral methods as a function of CFL number. Each test used the "fat" cylinder of 2.0 mm radius and a spatial step size of four points per minimum wavelength.
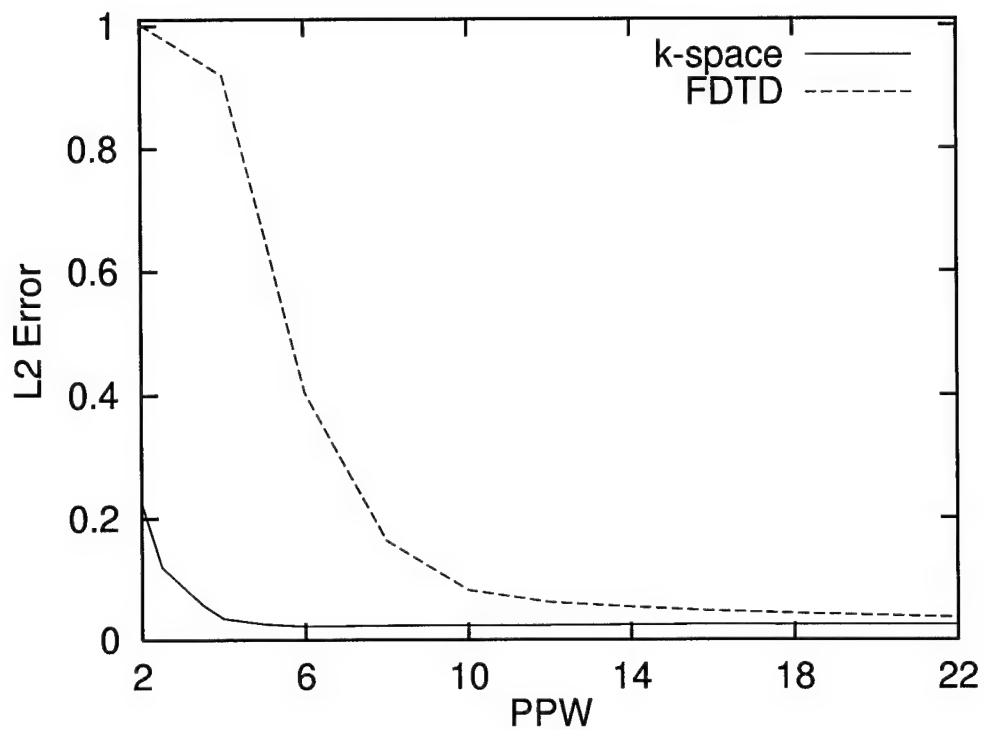
Figure 3: Time-domain comparison of accuracy for the k-space and finite-difference time-domain methods as a function of the spatial step size in points per minimum wavelength (PPW). Each test used the "fat" cylinder of 2.0 mm radius. CFL numbers were 0.5 for the k-space method and 0.25 for the finite-difference time-domain method.
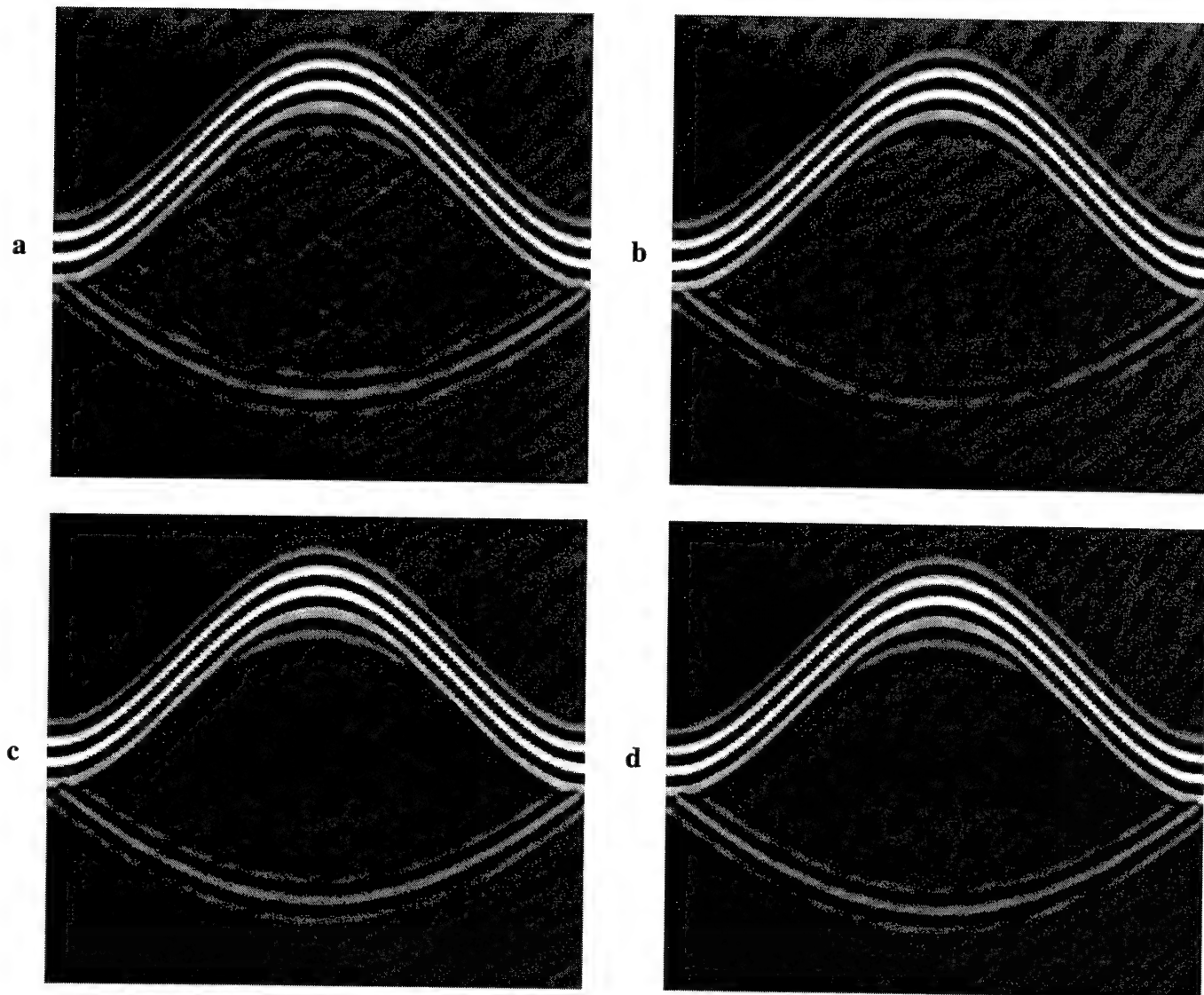
Figure 4: Computed waveforms for the "fat" cylinder at a radius of 2.5 mm for a cylinder of radius 2.0 mm and a pulse center frequency of 2.5 MHz. The acoustic pressure is shown on a bipolar logarithmic scale with 60 dB dynamic range. The horizontal range of each plot is 360 degrees, covering the entire measurement circle starting with angle 0 (forward propagation). The vertical range of each panel corresponds to a temporal duration of 9 μs, with $t = 0$ at the top of each plot. (a) Unsmoothed object; k-space solution with four points per minimum wavelength, L^2 error 0.0347. (b) Smoothed object; k-space solution with four points per minimum wavelength, L^2 error 0.0414. (c) Finite-difference solution with 14 points per minimum wavelength, L^2 error 0.0529. (d) Exact solution.
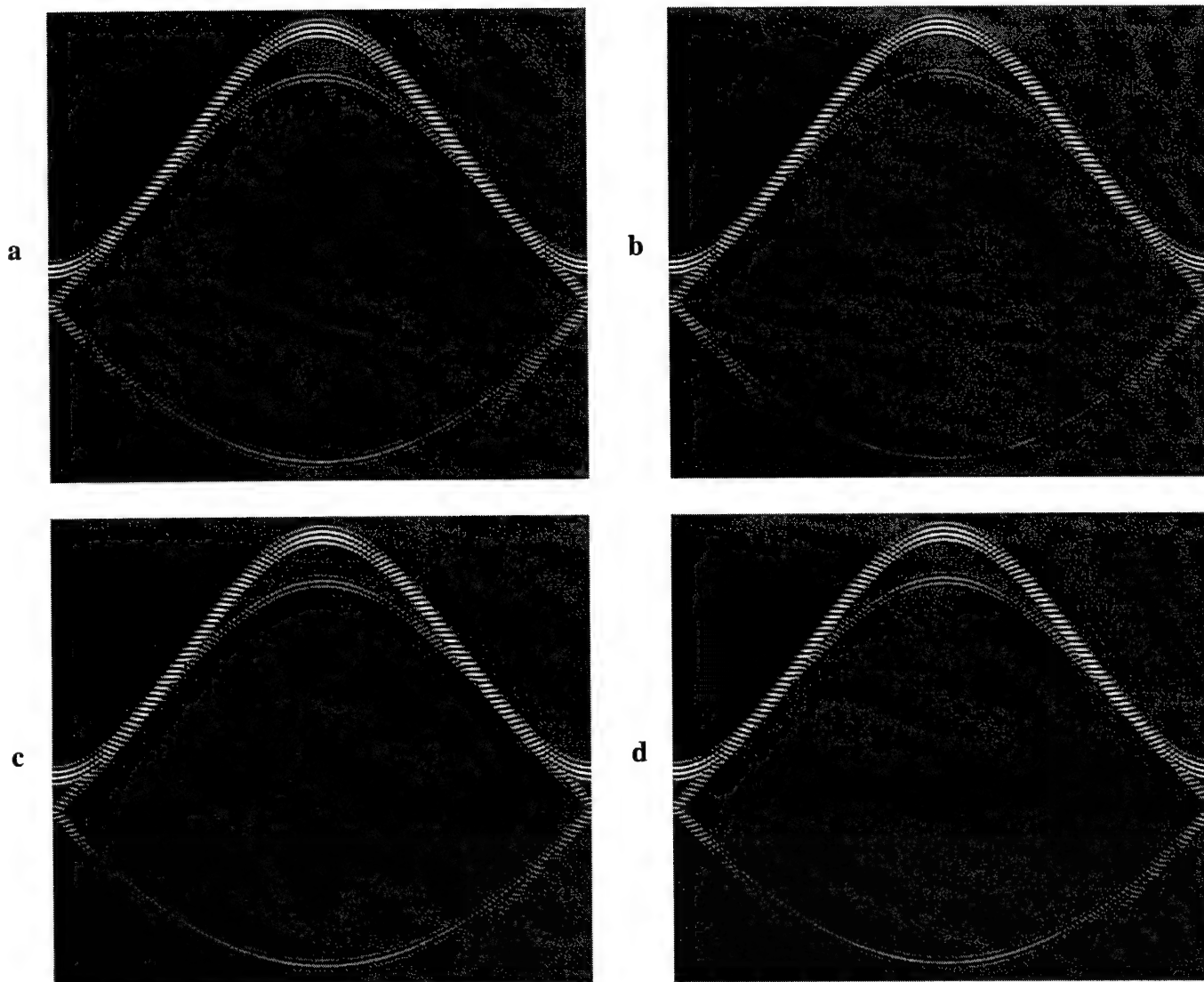
27

Figure 5: Computed waveforms at a radius of 12.5 mm for a "fat" cylinder of radius 10.0 mm and a pulse center frequency of 2.5 MHz. The acoustic pressure is shown in each panel using a bipolar logarithmic scale with a 60 dB dynamic range. The horizontal range of each panel is 360 degrees and the vertical range is 33 μs. (a) Unsmoothed object; k-space solution, L^2 error 0.1103. (b) Smoothed object; k-space solution, L^2 error 0.1080. (c) Finite-difference solution, L^2 error 0.1763. (d) Exact solution.
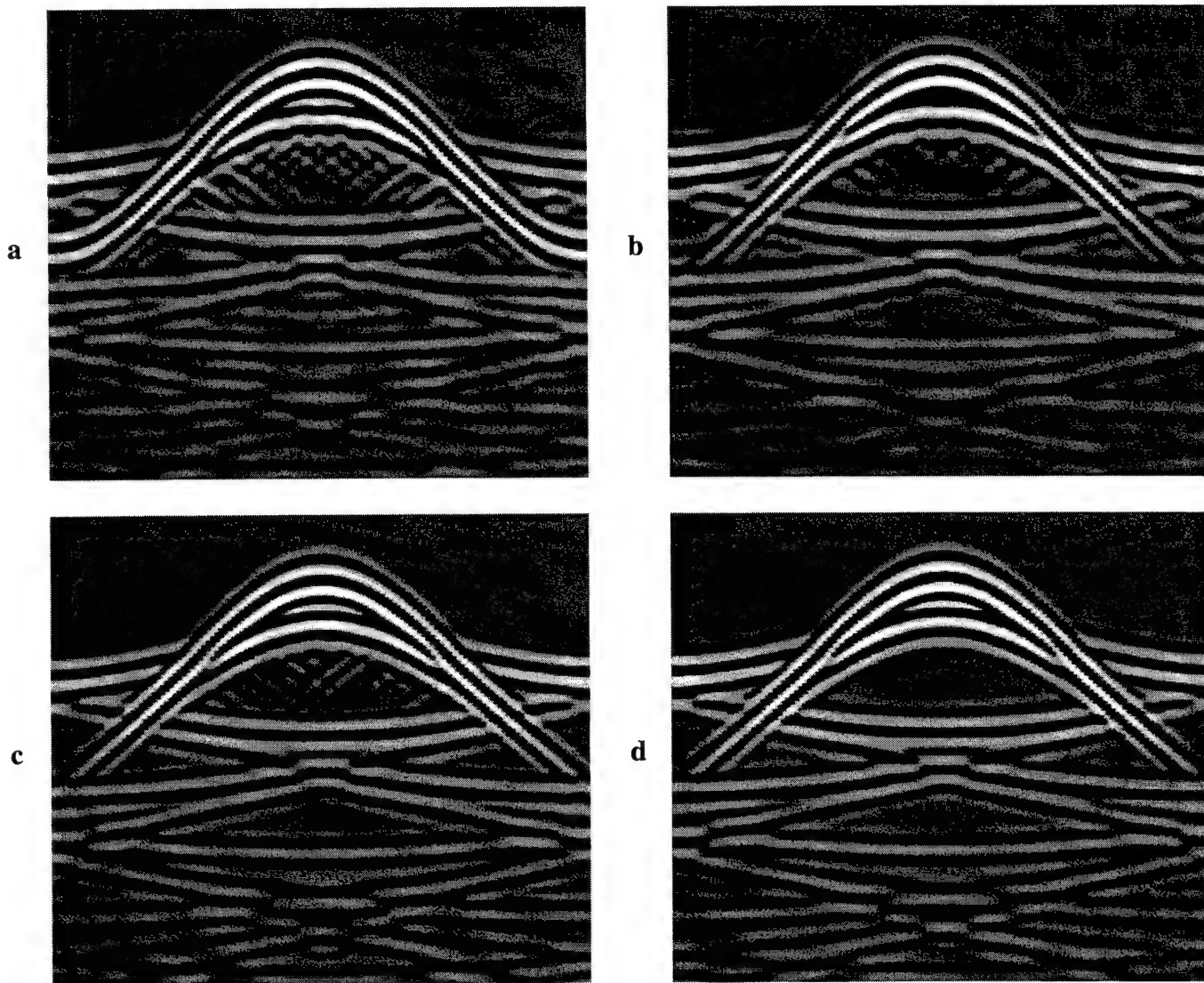
Figure 6: Computed pressure waveforms at a receiver radius of 2.5 mm for a "bone" cylinder of radius 2.0 mm and a pulse center frequency of 2.5 MHz. The format is the same as in Fig. 4. (a) Unsmoothed object; k-space solution, L^2 error 0.3072. (b) Smoothed object; k-space solution, L^2 error 0.8551. (c) Finite-difference solution, L^2 error 0.0541. (d) Exact solution.
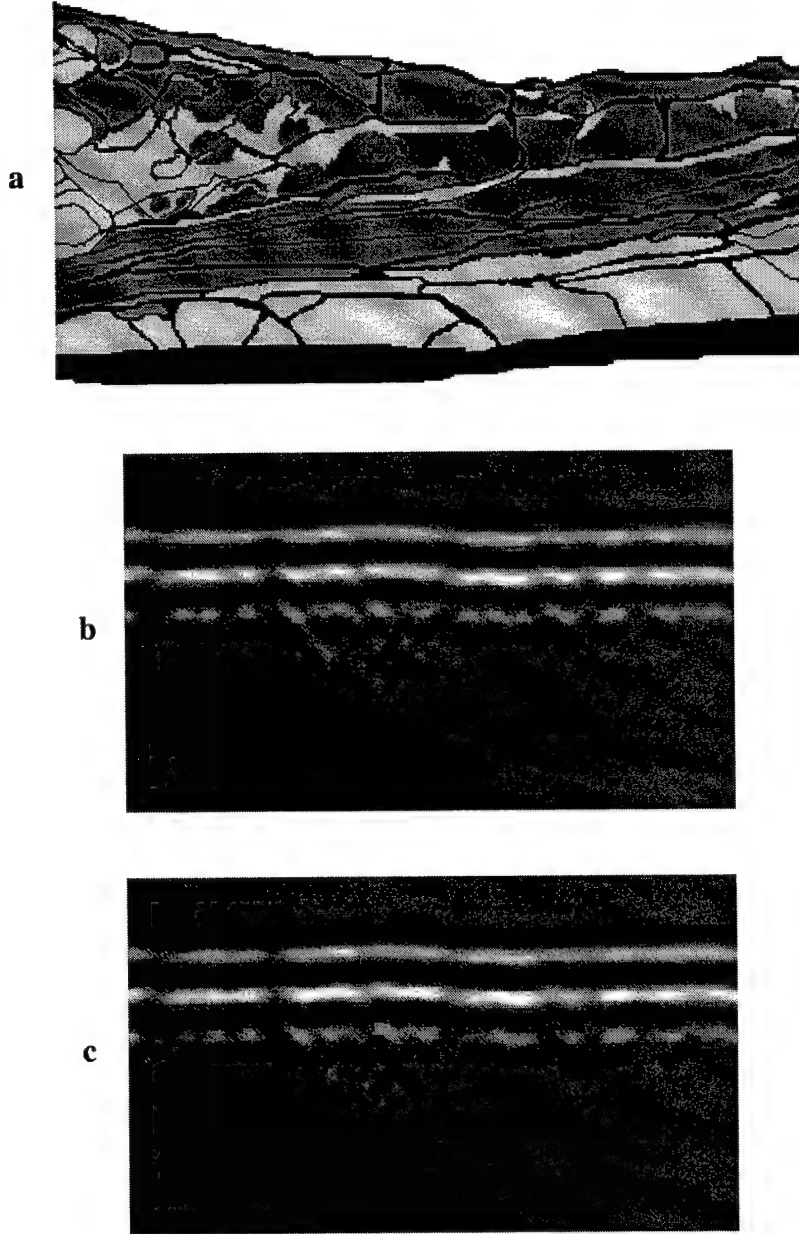
Figure 7: Comparison of k-space and finite-difference methods for a tissue cross-sectional model. (a) Chest wall cross section (taken from Ref. [24]), with black indicating connective tissue, dark gray indicating muscle, and light gray indicating fat. The region is 33.5 mm wide and 17.2 mm high. (b) Transmitted waveforms computed by the k-space method using four points per minimum wavelength and a CFL number of 0.5, shown on a bipolar linear gray scale with white indicating maximum positive pressure and black indicating maximum negative pressure. The horizontal range shown is 27.3 mm and is shown to the same scale as in (a). The vertical range is 3.29 μs. (c) Transmitted waveforms computed by the finite-difference time-domain method using 10 points per minimum wavelength and a CFL number of 0.25, shown using the same format as in (b).

Appendix D

Abstracts

"Simulation of Ultrasonic Pulse Propagation, Distortion,
and Attenuation in the Human Chest Wall"

Presented at the 136th Meeting of the Acoustical
Acoustical Society of America

"Time-Domain Ultrasound Diffraction Tomography"

Presented at Forum Acusticum 99
[Joint Meeting: 137th Meeting of the Acoustical Society of America,
2nd Convention of the European Acoustics Association,
and 25th German Acoustics DAGA Conference]

4pBB4. Simulation of ultrasonic propagation, scattering, and attenuation in the human chest wall. T. Douglas Mast (Appl. Res. Lab., Penn State Univ., University Park, PA 16802, mast@sabine.acs.psu.edu), Laura M. Hinkelman (Penn State Univ., University Park, PA 16802), and Robert C. Waag (Univ. of Rochester, Rochester, NY 14627)

A finite-difference time-domain model for ultrasonic pulse propagation through soft tissue [Mast *et al.*, J. Acoust. Soc. Am. **102**, 1177–1190 (1997)] has been extended to incorporate absorption effects as well as longitudinal-wave propagation in cartilage and bone. This extended method has been used to simulate ultrasonic propagation through anatomically detailed chest wall models. The inhomogeneous chest wall structure is represented by two-dimensional tissue maps determined by staining chest wall cross sections to identify connective tissue, muscle, fat, cartilage, and bone, scanning the stained cross sections at 300 dpi, and processing the scanned images to assign a tissue type to each pixel. Each pixel of the tissue map is then assigned a sound speed, density, and absorption value determined from published measurements to be representative of the local tissue type. Computational results for wavefront distortion including amplitude fluctuations, arrival time fluctuations, and waveform distortion show qualitative agreement with measurements performed on the same specimens [Hinkelman *et al.*, J. Acoust. Soc. Am. **101**, 2365–2373 (1997)]. Visualization of simulated tissue-ultrasound interactions in the chest wall shows possible mechanisms for image aberration in echocardiography, including effects due to reflection and diffraction from rib structures.

2aPAb6. Time-domain ultrasound diffraction tomography. T. Douglas Mast (Appl. Res. Lab., Penn State Univ., University Park, PA 16802, mast@sabine.acs.psu.edu)

A quantitative ultrasonic imaging method employing time-domain scattering data is presented. This method provides tomographic images of inhomogeneous media using scattering measurements made on a surface surrounding the medium of interest, e.g., on a circle for two-dimensional problems or on a sphere for three-dimensional problems. These scattering data are used to construct a time-domain analog of the far-field scattering operator. Images of compressibility variations are then reconstructed using a coherent combination of the far-field scattered waveforms, delayed and summed in a manner that numerically focuses on the unknown medium. This approach is closely related to synthetic aperture imaging; however, unlike conventional synthetic-aperture methods, the present method provides quantitative reconstructions of compressibility variations, analogous to frequency-compunded filtered backpropagation images weighted by the spectrum of the incident wave. Example reconstructions, obtained using synthetic data for two-dimensional scattering of wideband pulses, show that the time-domain reconstruction method can provide image quality superior to single-frequency reconstructions for objects of size and contrast relevant to medical imaging problems such as ultrasonic mammography. Reconstructions also illustrate the dependence of image quality on the number of incident-wave insonifications and on the range of scattering angles available for measurements.

Appendix E

Curriculum Vitae

T. Douglas Mast

Principal Investigator

Annual Report for DAMD17-98-1-8141, July 1999

T. Douglas Mast

Research Associate, Applied Research Laboratory,
The Pennsylvania State University, P.O.B. 30, State College, PA 16804
(814) 863-9998 (tel.), (814) 863-9918 (fax), mast@sabine.acs.psu.edu

Research and Teaching Interests

Physical acoustics, ultrasonic imaging, wave propagation and scattering in inhomogeneous media, inverse scattering, flow/sound interaction, bioacoustics, nondestructive evaluation.

Education

Ph.D. in Acoustics, The Pennsylvania State University, 1993. Thesis: *Physical Theory of Narrow-Band Sounds Associated with Aneurysms*. Advisor: Allan D. Pierce. GPA: 3.93/4.0.

Certificate (comparable to B.A.) in Music, The Naropa Institute, 1988.

B.A. in Physics and Mathematics, Goshen College, 1987. GPA: 3.89/4.0.

Present and Recent Employment

Research Associate, Applied Research Laboratory, The Pennsylvania State University, 1997–present.

Postdoctoral Scholar, Applied Research Laboratory, The Pennsylvania State University, 1996–1997.

Postdoctoral Fellow, Ultrasound Research Laboratory, University of Rochester, 1993–1996.

Research Asst., Graduate Program in Acoustics, Pennsylvania State University, 1988–1993.

Research Asst., Turner Laboratory of Precision X-Ray Measurements, Goshen College, 1986–1987.

Teaching Asst., Department of Physics, Goshen College, 1985–1987.

Honors, Awards and Society Affiliations

Listed in *Who's Who in Science and Engineering*.

Kenneth E. Simowitz Memorial Award, The Pennsylvania State University, 1996.

F. V. Hunt Fellowship, Acoustical Society of America, 1994–1995.

Kenneth E. Simowitz Memorial Citation, The Pennsylvania State University, 1992.

General Electric Teaching Incentive Loan, 1990.

Turner Laboratory Fellowship, Goshen College, 1986.

Member of Acoustical Society of America.

Member of American Institute of Ultrasound in Medicine.

Member of Institute of Electrical and Electronics Engineers (Ultrasonics, Ferroelectrics, and Frequency Control Society).

Scientific Publications

Mast, T. D. and Gordon, G. A., "Quantitative flaw reconstruction from ultrasonic surface wavefields measured by electronic speckle pattern interferometry," submitted to *IEEE Trans. Ultrason. Ferroelect. Freq. Control* (1999).

Mast, T. D., "Wideband quantitative ultrasonic imaging by time-domain diffraction tomography," submitted to *J. Acoust. Soc. Am.* (1999).

Mast, T. D., Hinkelman, L. M., Metlay, L. A., Orr, M. J., and Waag, R. C., "Simulation of ultrasonic pulse propagation, distortion, and attenuation in the human chest wall," submitted to *J. Acoust. Soc. Am.* (1999).

Souriau, L. P., Mast, T. D., Liu, D.-L. D., Nachman, A. I., and Waag, R. C., "A new *k*-space method for large-scale models of wave propagation in tissue," submitted to *IEEE Trans. Ultrason. Ferroelect. Freq. Control* (1999).

Mast, T. D., Swanson, D. C., Mahon, M. P. and Norris, D. E., "Resolution of multipath outdoor sound propagation using spread spectrum signals," submitted to *J. Acoust. Soc. Am.* (1998).

Gordon, G. A. and Mast, T. D., "Wide-area imaging of ultrasonic Lamb wave fields by electronic speckle pattern interferometry," *Proc. SPIE* **3586**, 297–309 (1999).

Myers, L. F, Lovette, M., Kilgus, C. C., Giannini, J. A., Swanson, D. C., Reichard, K. M., Mahon, M. P., and Mast, T. D., "Java-based information system for wayside sensing and control," *Proceedings of the IEEE/ASME Joint Railroad Conference*, 135–147 (1998).

Hinkelman, L. M., Mast, T. D., Metlay, L. A., and Waag, R. C., "The effect of abdominal wall morphology on ultrasonic pulse distortion. Part I: Measurements," *J. Acoust. Soc. Am.* **104**, 3635–3649 (1998).

Mast, T. D., Hinkelman, L. M., Orr, M. J., and Waag, R. C., "The effect of abdominal wall morphology on ultrasonic pulse distortion. Part II: Simulations," *J. Acoust. Soc. Am.* **104**, 3650–3664 (1998).

Mast, T. D., Hinkelman, L. M., Orr, M. J., Sparrow, V. W., and Waag, R. C., Erratum: "Simulation of ultrasonic pulse propagation through abdominal wall," [*J. Acoust. Soc. Am.* **102**, 1177–1190 (1997)], *J. Acoust. Soc. Am.* **104**, 1124–1125 (1998).

Jansson, T. T., Mast T. D., and Waag, R. C., "Measurements of differential scattering cross-section using a ring transducer," *J. Acoust. Soc. Am.* **103**, 3169–3179 (1998).

Mast, T. D., Nachman, A. I., Liu, D.-L., and Waag, R. C., "Quantitative imaging with eigenfunctions of the scattering operator," *1997 IEEE Ultrasonics Symposium Proceedings*, Vol. 2, pp. 1507–1510.

Hinkelman, L. M., Mast, T. D., Orr, M. J., and Waag, R. C., "Effects of abdominal wall morphology on ultrasonic pulses," *1997 IEEE Ultrasonics Symposium Proceedings*, Vol. 2, pp. 1493–1496.

Mast, T. D., Nachman, A. I., and Waag, R. C., "Focusing and imaging using eigenfunctions of the scattering operator," *J. Acoust. Soc. Am.* **102**, 715–725 (1997).

Mast, T. D., Hinkelman, L. M., Orr, M. J., Sparrow, V. W., and Waag, R. C., "Simulation of ultrasonic pulse propagation through abdominal wall," *J. Acoust. Soc. Am.* **102**, 1177–1190 (1997).

Mast, T. D. and Waag, R. C., "Wave space resolution in ultrasonic scattering measurements," *J. Acoust. Soc. Am.* **98**, 3050–3058 (1995).

Mast, T. D. and Pierce, A. D., "A theory of aneurysm sounds," *J. Biomech.* **28**, 1045–1053 (1995).

Mast, T. D. and Pierce, A. D., "Describing-function theory for flow excitation of resonators," *J. Acoust. Soc. Am.* **97**, 163–172 (1995).

Mast, T. D., "Limit cycles of flow-excited resonators: a describing-function analysis," in *Structural Acoustics, Scattering, and Propagation: Theoretical and Computational Acoustics—Volume I*, Edited by J. E. Ffowcs Williams, D. Lee, and A. D. Pierce, (River Edge, New Jersey: World Scientific, 1994), pp. 389-403.

Mast, T. D. and Pierce, A. D., "Flow-induced sounds associated with aneurysms," in *Flow Noise Modeling, Measurement, and Control*, edited by T. M. Farabee, W. L. Keith, and R. M. Lueptow (New York: American Society of Mechanical Engineers, 1991), pp. 129-134.